PARTICLE DYNAMICS SIMULATION OF GRAVITY DRIVEN GRANULAR POISEUILLE FLOW

A Thesis

Submitted for the Degree of

Master of Science (Engineering)

by

Vijayakumar Kudleppa Chikkadi

Engineering Mechanics Unit
Jawaharlal Nehru Centre for Advanced Scientific Research
(A Deemed University)
Bangalore – 560 064

FEBRUARY 2008

DECLARATION

I declare that the matter embodied in the thesis entitled "**Particle Dynamics Simulation of Gravity Driven Granular Poiseuille Flow**" is the result of investigations carried out by me at the Engineering Mechanics Unit, Jawaharlal Nehru Centre for Advanced Scientific Research, Bangalore, India under the supervision of Dr. Meheboob Alam and that it has not been submitted elsewhere for the award of any degree or diploma.

In keeping with the general practice in reporting scientific observations, due acknowledgment has been made whenever the work described is based on the findings of other investigators.

Vijayakumar Kudleppa Chikkadi

CERTIFICATE

I hereby certify that the matter embodied in this thesis entitled "**Particle Dynamics Simulation of Gravity Driven Granular Poiseuille Flow**" has been carried out by Mr. Vijayakumar Kudleppa Chikkadi at the Engineering Mechanics Unit, Jawaharlal Nehru Centre for Advanced Scientific Research, Bangalore, India under my supervision and that it has not been submitted elsewhere for the award of any degree or diploma.

Dr. Meheboob Alam
(Research Supervisor)

Abstract

The gravity-driven flow of granular materials in a vertical channel is simulated using molecular dynamics technique. The granular particles are modelled as smooth hard disks, so the simulations are performed in two dimensions. An event-driven algorithm proposed by Lubachevsky [51] has used to perform simulations. The control paramters are : volume fraction of particles (ν), normal restitution coefficient (e_n) that characterises the loss due to particle-particle collisions and tangential restitution coefficient (β_w) that characterises the energy loss due to particle-wall collisions. We have studied various aspects of granular Poiseuille flow (GPF) over a range of the control paramters.

The local velocity distribution of the fluctuating velocities in x-direction and y-direction, denoted as $P(u_x)$ and $P(u_y)$, are close to a Gaussian distribution over a wide range of densities ($\nu \leq 0.85$) for nearly elastic collisions ($e_n \rightarrow 1$). Increasing the wall roughness leads to interesting *asymmetric* distribution function for u_x, with a peak at negative velocities in the near wall region. On the other hand, an increase in the degree of dissipation due to particle-particle collisions is accompanied with the formation of a plug at the centre of the channel and the structure of the flow undergoes a transition from liquid to a crystal like state. Within the plug, the density correlations and the spatial correlations of streamwise velocity are enhanced, leading to deviation of tails of the velocity distribution (both $P(u_x)$ & $P(u_y)$) from a Gaussian to a power-law. The flow outside the plug region is in a gaseous state with negligible density and velocity correlations.

Various rheological quantities such as the pressure, shear stress, viscosity and first normal stress difference are computed over a range of densities and dissipation. In the quasi-elastic limit, the simulation results agree well with expressions derived from kinetic theory by Jenkins & Richman [41] for circular disks. In the

quasi-elastic limit, the first normal stress difference ($\mathcal{N}_1$) is negligible. At higher dissipation, the first normal stress difference near the center-line of the channel increases from zero in the dilute limit, reaches a maximum value at some intermediate density and then decreases, attaining a negative value beyond a critical density. A closer look at kinetic ($\mathcal{N}_1^k$) and collisional ($\mathcal{N}_1^c$) components of $\mathcal{N}_1$ reveals that $\mathcal{N}_1$ at large densities is dictated by the behaviour of its collisional component ($\mathcal{N}_1^c$), which reverses sign beyond a certain volume fraction due to the structural re-organisaton of particles. The microstructural origin of the sign-reversal of $\mathcal{N}_1$ in GPF appears to be the same as in the sheared granular flow of Alam & Luding [1].

The simulations predict a power-law relation between the slip velocity and Knudsen number over the range $Kn \sim (1.1 - 0.02)$ for $e_n > 0.8$ with the exponent varying from $\alpha \sim (0.55 - 0.78)$. A similar power law dependence of Knudsen number and slip velocity on volume fraction was also observed over the range $\nu \sim (0.015{-}0.4)$ for $e_n > 0.7$. In addition, the velocity gradient near the walls varies as a negative power of the Knudsen number over the range ($Kn \sim 0.001 - 3$) and $e_n \sim (1{-}0.8)$, with an exponent $\alpha = -0.212$. Furthermore, the simulations predict the average velocity to be constant at very low Knudsen number ($Kn < 0.005$) and decrease rapidly with further increase in the Knudsen number.

The temporal evolution and steady structure of density waves are investigated in different density regimes. At moderate densities, the density waves have three different steady state structures : a plug, wave and slug. The range of L/W values over which different structures exist depends on the aspect ratio W/d. In dense flows, at moderate and high value of coefficient of restitution ($e_n > 0.8$) a new symmetric wave mode (varicose mode) emerges. Otherwise, at lower values of e_n ($= 0.5$) the density waves display a transition from plug-wave-slug with increasing L/W ratio. In the dilute limit, the particles form small clumps with no distinct features over a large range of L/W and W/d ratios. Besides, the effect of wall roughness was studied by varying the roughness of the walls symmetrically and asymmetrically. In the case of symmetric roughness, the effect on density waves was negligible, whereas in the case of asymmetric roughness the density waves were pushed towards the smooth (cold) wall but the effect on the structure of density waves was found to be small.

Contents

List of Figures

CHAPTER 1

INTRODUCTION

1.1 Granular matter

Granular materials are ubiquitous in nature and occur in a variety of forms. Planetary object like Saturn rings and the interstellar dust, sand dunes, food items and pills, all comprise of granular particles. Many of the industrial applications involve handling of granular material, for example, the pharmaceutical industries that manufacture the powder and pills need to transport and process granular particles; similarly, the food industries process grains and seeds on a large scale. Due to numerous industrial applications it is imperative to understand the behaviour of granular materials. Some of the pressing industrial concerns are :
(a) Segregation occurs spontaneously when particles of different sizes are mixed [58, 59, 71], while ideally one would like to suppress segregation to achieve uniform mixing in pharmaceutical industries.
(b) Jamming in granular materials is a very common phenomenon that leads to clogging of feeders and hoppers in food industries [49, 90, 100]. Improved design of equipments or other strategies to prevent jamming is desirable.
(c) Clustering is frequently encountered when transporting granular material via conveyor belts, sorting machines, etc., so normally one would like to devise methods to break these clusters.
Even a small improvement in our understanding of granular materials could lead to a profound impact on these industries.

Granular materials are primarily collections of solid particles of different sizes and shapes. They can exist in any of the three states of matter : solid, liquid or gas. For instance, consider a sand pile at rest with a slope lower than the angle of repose, Fig. 1.1 (a), it behaves as a solid. When the slope of the pile exceeds the angle of repose, Fig. 1.1 (b), particles begin to flow like a liquid [39, 67]. It is observed that only the particles on the surface begin to flow like a liquid, while the particles underneath are in a state of rest or solid like state. Hence, the liquid-solid states can coexist in a granular system.

Besides, the very fact that granular particles behave differently from molecules make them interesting to study. The difference arises fundamentally for two reason : granular particles are macroscopic in nature and the collisions are inelastic. Due to their macroscopic nature, the energy needed to lift a particle is large compared to the energy it receives from the thermal environment *i.e,* k_BT, where k_B is the Boltzmann constant and T is the thermodynamics temperature. As a consequence, they cannot spontaneously rearrange in phase space due to thermal motion.

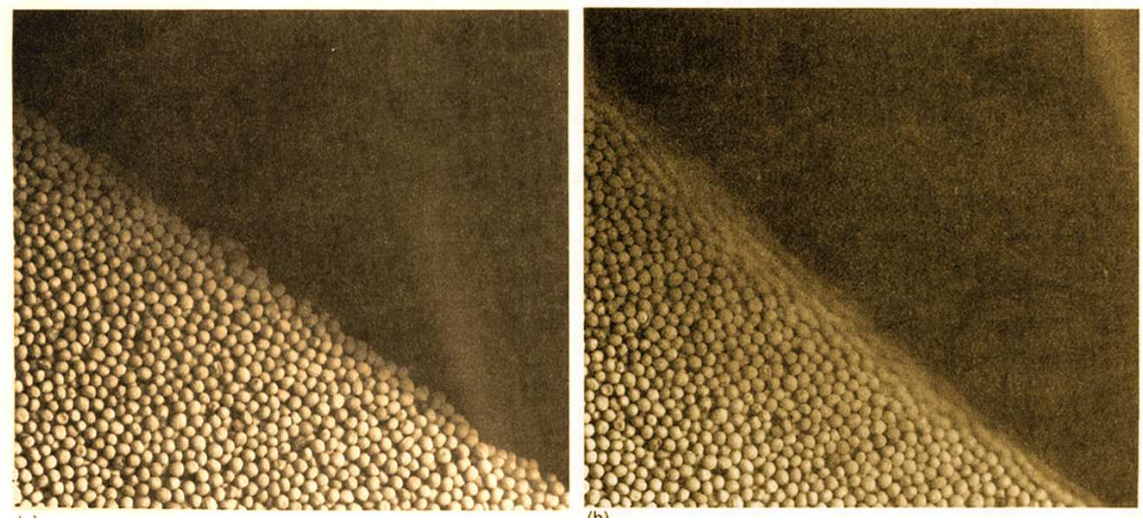

(a) (b)

Figure 1.1: (a) A pile of mustard seeds with angle of tilt lower than the angle of repose. (b) The pile is tilted at an angle greater than the angle of repose to create an avalanche. The pictures are taken from Ref. [39].

In other words, these are non-Brownian or athermal systems. In order to set them into motion, they have to be perturbed by external forcing. Some of the commonly used forcing techniques in experiments are shearing the particles between a pair of plates or vibrating them on a bed, *etc.* Another related issue is the lack of scale separation between microscopic and macroscopic scales. Due to this reason additional difficulties arise in describing granular media using standard hydrodynamics equations [30, 45] which assume scale-separation. The scale-separation assumption implies the existence of well defined length and time scales, much larger than microscopic scales and smaller than macroscopic scales, over which averaging is performed. It is not obvious that such a separation of scales exists in granular matter. Moreover, due to the lack of spontaneous rearrangement by thermal motion, the fluctuations and average values are often of the same order. The inelastic collisions is the other distinguishing feature of granular particles that sets them apart from molecules. Since the collisions lead to dissipation of energy, to sustain a steady motion of the particles it is necessary to continuously inject energy into the system. Hence they are inherently out-of-equilibrium. It could be stated without hesitation that the dynamics of granular particles is rich since dissipation gives rise to a host of interesting phenomena, such as clustering, non-Gaussian velocity distribution [9, 11, 16, 28, 63, 64, 68, 75, 85, 93, 94], non-equipartition of energy in a binary mixture [1, 2, 3, 7, 29] and others. The dissipative and athermal character of the individual components breaks two fundamental assumptions of classical statistical physics: the conservation of energy and the ergodic exploration of the

phase space. Consequently, concepts from equilibrium statistical mechanics need to be modified [30].

Depending on the nature of particle-particle interaction, granular flows are classified into two regimes : *slowly deforming flows* and *rapidly deforming flows*. Slow flows are characterised by enduring contact between the particles with sliding and rolling motion dominating the interactions. Generally, in such flow the densities are high and the deformation rates are low. The momentum and energy are transferred between particles mainly through frictional forces, so they are also known as frictional flows. On the other hand, rapid flows are characterised by high deformation rates and are reminiscent of molecular gases. The transport of momentum and energy occur through instantaneous binary collisions between the particles. These similarities with the thermal motion of molecules have motivated in defining the temperature of granular gases, analogous to molecules, as the mean kinetic energy associated with the fluctuation motion [69]. However, it should be noted this temperature is not the thermodynamic temperature.

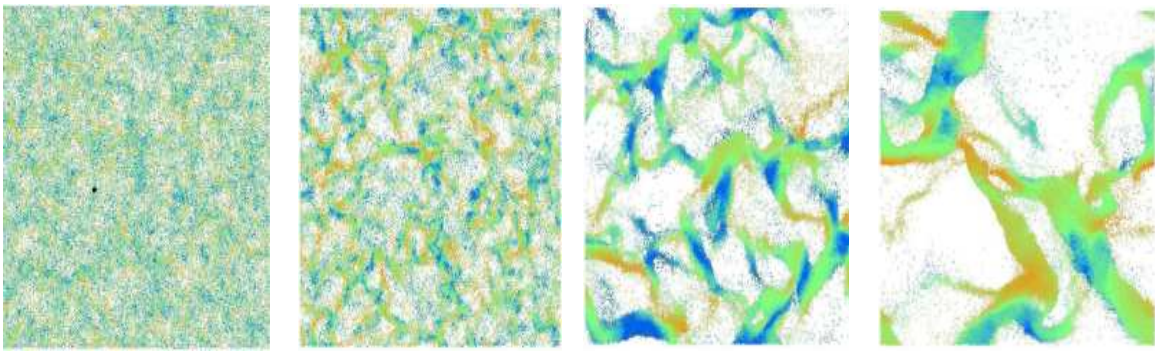

Figure 1.2: Snapshots of the cooling of an inelastic gas starting from thermal equilibrium, in an event-driven simulation [53]. The energy of single particle is color coded and the arrow at the bottom of the figure indicates direction of time.

A small modification in the interaction of the particles can give rise to a dramatic change in the behaviour of the system. To illustrate the effect of inelastic collision we present computer simulation results of Luding and Herrmann [53]. Consider an elastic gas that is initially in a state of equilibrium with homogeneous distribution of particles. Imagine its coefficient of restitution is switched to a value less than 1 at a time t_0. Until t_0, the system is in equilibrium at a well defined temperature, but at later times ($t > t_0$), the collisions start dissipating energy, and the temperature drops. Very soon correlations develop and structures appear in density fields, see Fig. 1.2. Such inhomogeneities generate dense clusters of particles inside which the collision rates are very high and the cooling is much faster than in more dilute parts of the system. As more and more grains aggregate, the late time dynamics is dominated by complex interactions among the clusters which

collide, merge and break [89].

We consider another example to demonstrate the clustering phenomena or the Maxwell's demon in a granular gas. Maxwell's demon was a "gedanken" experiment conceived by James Clerk Maxwell. He described the demon as capable of spontaneously separating the fast moving molecules from the slow moving ones, or in other words, the creation of hot and cold zones in a molecular gas. While many Physicists have ruled out such a possibility in equilibrium systems, however, a granular gas which is not in equilibrium is capable of exhibiting features that are reminiscent of Maxwell's demon [26, 84, 86].

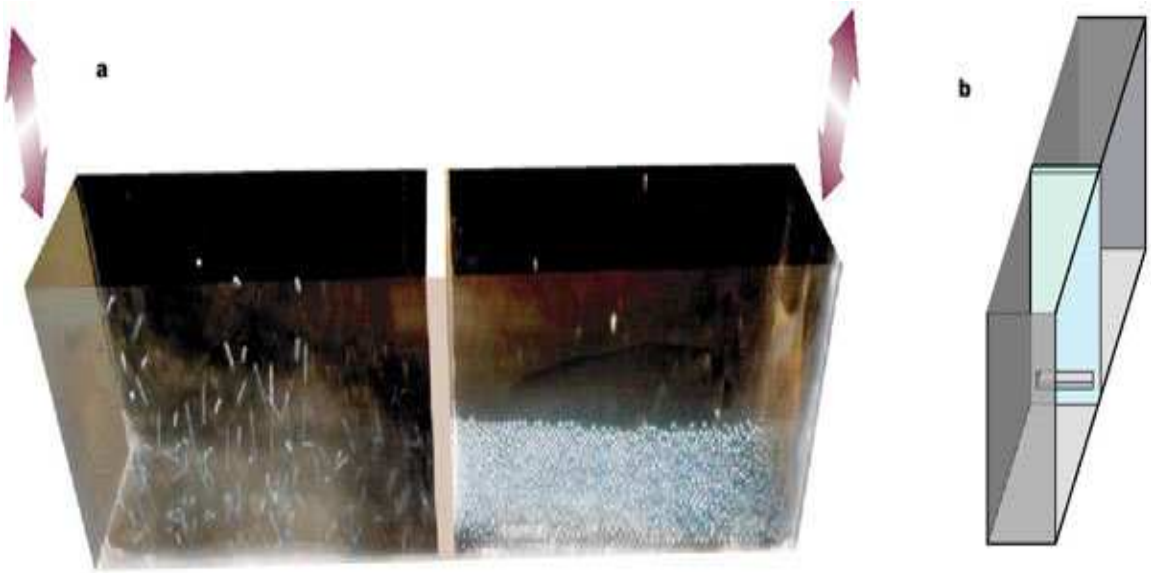

Figure 1.3: (a) Snapshot of spontaneous separation between gas-like and solid-like states of steel beads (diameter 2 mm) from an experiment in which an acrylic container is vibrated sinusoidally at 10 Hz and a maximum acceleration of 1.3g. Initially the beads are distributed uniformly across the container, but owing to collisional inelasticity they migrate to whichever side randomly acquires a slight excess of beads. (b) Schematic of container which is divided into two chambers by a barrier containing a window 6 mm high, beginning 6 mm from the bottom of the container. These figures are taken from Ref. [86].

In an experiment by Schlichtting & Nordmeier [84], a box is divided into two compartments by introducing a wall. A hole is made in the wall such that there is exchange of energy and mass between the compartments as shown in Fig. 1.3. At the start of the experiment the box is filled with equal number of beads and they are brought into a state of gas by vertical agitation. When the agitation is strong, the compartments are filled with equal number of beads. On decreasing the agitation, a critical threshold is met below which the symmetry is broken. One of the compartment is more populated that the other and the grains in the

denser compartment suffer more collisions. Since the collisions are inelastic, it leads to decrease in the mean kinetic energy. On the other hand, the particles in the dilute compartment have, relatively, higher mean kinetic energy due to similar arguments and hence the escape rate of particles from this compartment is more compared to the other. If the vertical agitation is not strong enough to overcome these fluctuations, it results in the formation of dense and dilute compartments that have different mean kinetic energies or granular temperatures. Hence a *cold* and *hot* can coexist in a granular gas, however, one should realise that granular particles are macroscopic and collisions are inelastic, unlike molecules.

Granular gases are known to deviate significantly from the behaviour of Newtonian fluids due to inelasticity [1, 17, 18, 31, 79, 97]. The stress tensor for granular flows is anisotropic and the normal stress differences, which are indicators of the non-Newtonian behaviour, have been studied by various authors. Jenkins & Richman [42] were first to point out that inelastic collisions lead to anisotropy in the second moment of fluctuating velocities that, in turn, manifests as first and second normal stress difference ($\mathcal{N}_1$ and $\mathcal{N}_2$). They predicted that $\mathcal{N}_1$ is maximum in the dilute limit and decays to zero at high densities. Later, Goldhirsch and Sela [31] established that the normal stress differences are Burnett-order effects and cannot be predicted at the level of Navier-Stokes (NS) that includes only first-order terms in Chapman-Enskog expansion. The origin of $\mathcal{N}_1$ (in the dilute limit) is universal in both atomic and granular fluids, with the inelasticity acting as an amplifier of these effects in granular fluids, [31]. Further, contrary to the observations of Jenkins & Richman [42], Alam & Luding [1] showed that the first normal stress difference undergoes a reversal in the sign, instead of decaying to zero, at high densities. They explained that this sign reversal occurs due to microstructural reorganisation of particles. When the normal stress differences are of order one, the NS-level hydrodynamics equations need to be augmented by incorporating higher-order effects.

The standard Fourier's law relates the local heat flux to the temperature gradient : $\vec{q} = -\kappa\vec{\nabla}T$, where κ is the thermal conductivity, T is the temperature and $\vec{q}$ is the heat flux. This expression does not hold for a granular gas and has to be modified suitably [55, 87]. A modified form of the Fourier's law, derived starting from the Boltzmann equation [13, 14, 85], has an additional term appearing due to density gradient :

$$\vec{q} = -\kappa\vec{\nabla}T - \mu\vec{\nabla}n, \tag{1.1}$$

where κ, $\vec{q}$ and T are analogues of thermal conductivity, heat flux and temperature for a granular gas and n is the number density. The coefficient μ has no analogue in a molecular system and is related to the inelastic effects : μ is positive when the collisions are inelastic and vanishes for elastic collisions. In Ref. [37], the local heat flux was measured in a two-dimensional vibrated granular gas via molecular dynamics simulation. It was found that the predictions of standard Fourier's law were reasonable only when the inelasticities were low, hinting that the standard hydrodynamics of Navier-Stokes has limited validity for moderately inelastic

systems.

1.2 Present work

In the present thesis, various aspects of the gravity-driven granular Poiseuille flow have been studied using molecular dynamics simulation [96] and the focus is mainly on the rapid flow regime. The particles are modeled as frictionless hard disks, so the simulations are performed in two dimensions by neglecting the rotational degrees of freedom. A billiard ball algorithm proposed by Lubachevsky [51] has been used for simulation. We have studied the local velocity distributions, rheological quantities such as pressure, shear stress, viscosity and first normal stress difference, slip velocity and density waves in the context of Poiseuille flow over a range of the control paramaters : particle volume fraction, normal resitution coefficient, wall roughness and channel width.

1.2.1 Organisation of thesis

Chapter 2

In this chapter, we begin with the modelling of granular particles, then describe the billiard ball algorithm [51] in detail and illustrate its advantages over other simple algorithms. Further, we suggest simple modifications to the billiard ball algorithm for simulating a gravity-driven Poiseuille flow, followed by a discussion on the method of averaging.

Chapter 3

Here the local velocity distribution [1] of streamwise and spanwise fluctuating velocities are studied over a wide range of densities and normal restitution coefficient. In the first section we compute the distributions in the quasi-elastic limit for smooth and rough walls and then move on to the distributions at higher dissipation in the next section. The deviation of the distributions from a Gaussian is quantified using kurtosis, while the skewness is used to get a measure of asymmetry associated with the distribution. Further, the spatial density and velocity correlations, along with velocity autocorrelation function (VAF), are examined to understand the behaviour of velocity distribution at high densities.

Chapter 4

Various rheological quantities like pressure, shear stress, viscosity and first normal stress ($\mathcal{N}_1$) are computed and compared with the theoretical predictions of Jenkins

[1] Part of this chapter has appeared in *Phys. Rev. E*, 75:051306, 2007

& Richmann [41], in the quasi-elastic limit. We study the effect of effect of normal restitution coefficient (e_n) on these quantities. The behaviour of $\mathcal{N}_1$ is of particular interest [2]. By decomposing $\mathcal{N}_1$ into kinetic and collisional components, we understand the origin of negative first normal stress difference. Some results on the effect of different control parameters on slip velocity and wall temperature (T_w) are presented, and the relationship between $slip$ and Kn is investigated.

Chapter 5

A Fourier analysis of the density field is carried out using the FFT subroutine in MATLAB to examine the time evolution of density waves. Different forms of the density waves are identified and a phase diagram of their steady state structures is presented in the $(L/W - W/d)$ plane. The phase diagrams are presented for different density regimes: dilute, moderately dense and dense. The role of wall-roughness is investigated by varying the tangential resitution coefficient of particle-wall collisions (β_w) in two ways : by assigning the same value of β_w to both walls and assigning different value of β_w to each wall. The phase diagram of structures for each case is presented on a $(L/W - \beta_w)$ plane.

CHAPTER 2

EVENT-DRIVEN SIMULATION

2.1 Hard disks

The granular particles are modelled as hard disks (*i.e.,* in two-dimension) for which the interaction potential $U(r)$ is purely repulsive :

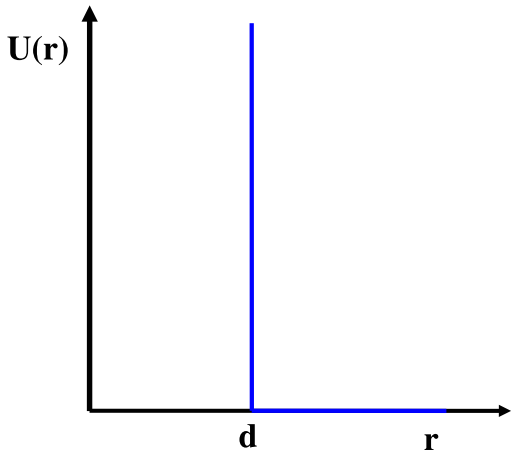

Figure 2.1: The repulsive potential of hard-disk, r is the distance between the centres of the disks.

$$U(r) = \begin{cases} 0 & (r > d) \\ \infty & (r \leq d) \end{cases} , \tag{2.1}$$

where d is the distance between the centers of disks at contact or the diameter of the disk. The form of this potential shown in Fig. 2.1 indicates that the repulsive forces come into play only when the disks are in contact. Since the interaction potential $U(r)$ between hard disks is a discontinuous function of r, the dynamics of hard-disks is qualitatively different than for a continuous potential such as the Lennard-Jones (L-J) potential for soft-spheres. The L-J potential consists of an attractive part and a repulsive part and is suitable for modelling molecular fluids. Due to continuous interaction it is possible to solve the dynamical equations numerically with any time integration method. However, for hard disks the interaction potential is singular and the task of integrating the equations of motion becomes a simple problem of processing a sequence of binary collisions between the particles.

The algorithm for hard particles therefore is event-driven (ED), as opposed to the time-driven algorithm for soft-particle molecular dynamics (MD) in which the equations of motion are integrated over small time steps. In an event-driven algorithm one needs to predict and process a sequence of discrete events. The simulation is advanced to the time of the event with the smallest scheduled time (the impending event) and that event is processed. The schedule of events is updated if necessary and the same process is repeated. This kind of collision-driven simulation has been extended and improved in a variety of ways, most importantly, to increase the efficiency of the algorithm.

2.2 Collision dynamics

The collisions between granular particles are inherently inelastic, due to which a fraction of kinetic energy is transferred to the internal degrees of freedom that appears in the form of heat. This process conserves only the momentum, so that the velocity of the centre of mass of the grains is not modified. Further, the particles are assumed to be smooth, thereby neglecting the rotational degree of freedom. Various models have been proposed to describe the binary inelastic collisions for hardsphere models [19, 33, 38, 57]. We consider a monodisperse system of smooth, inelastic disks of diameter $\tilde{d}$ and mass $\tilde{m}$ interacting through a hard-core potential. (The tilde denotes dimensional quantities). The degree of inelasticity is characterised by the *coefficient of normal restitution*, e_n, which is fixed for all collisions. This is the simplest collision model that nevertheless leads to interesting and meaningful results.

Now consider a collision between particles *1* and *2*. Let $\tilde{\mathbf{u}}_1$ and $\tilde{\mathbf{u}}_2$ be the velocities before collision and $\tilde{\mathbf{u}}_1'$ and $\tilde{\mathbf{u}}_2'$ be the post-collisional velocities. From the conservation momentum we get :

$$\tilde{\mathbf{u}}_1 + \tilde{\mathbf{u}}_2 = \tilde{\mathbf{u}}_1' + \tilde{\mathbf{u}}_2'. \tag{2.2}$$

Since the kinetic energy is not conserved during collision, a second equation is required to close the above equation and it comes from the definition of the *coefficient of normal restitution* e_n. It is the ratio of the *post-collisional* relative velocity to the *pre-collisional* relative velocity along the direction of line connecting the centres of particles, expressed as :

$$\tilde{\mathbf{u}}_{21}'\cdot\hat{\mathbf{n}} = -e_n\left(\tilde{\mathbf{u}}_{21}\cdot\hat{\mathbf{n}}\right), \tag{2.3}$$

where $0 \leq e_n \leq 1$. The collisions are perfectly elastic when $e_n = 1$, and when $e_n = 0$ collisions are perfectly inelastic which implies that the particles stick to each other after collision.

By solving Eq. 2.2 and Eq. 2.3, the *post-collisional* velocities could be related

to *pre-collisional* velocities as given below :

$$\tilde{\mathbf{u}}_1' = \mathbf{u}_1 - \frac{1+e_n}{2}\left(\tilde{\mathbf{u}}_{12}\cdot\hat{\mathbf{n}}\right)\hat{\mathbf{n}}, \tag{2.4a}$$

$$\tilde{\mathbf{u}}_2' = \mathbf{u}_2 + \frac{1+e_n}{2}\left(\tilde{\mathbf{u}}_{12}\cdot\hat{\mathbf{n}}\right)\hat{\mathbf{n}}. \tag{2.4b}$$

The momentum change during a collision *i.e.*, the impulse $\tilde{\mathbf{I}}$ is given by :

$$\tilde{\mathbf{I}} = \tilde{m}\frac{1+e_n}{2}\left(\tilde{\mathbf{u}}_{12}\cdot\hat{\mathbf{n}}\right)\hat{\mathbf{n}}. \tag{2.5}$$

We now consider the criteria for a collision to occur. Consider disks 1 and 2 at positions $\tilde{\mathbf{r}}_1$ and $\tilde{\mathbf{r}}_2$ at $t = 0$. If they collide at a time $\tilde{t_{12}}$ later, their centers will be separated by a distance d. The time of collision is found using the following set of equations :

$$\left|\tilde{\mathbf{r}}_1(t_{12}) - \tilde{\mathbf{r}}_2(t_{12})\right| = \tilde{d}, \tag{2.6a}$$

$$\tilde{\mathbf{r}}_1(t_{12}) = \tilde{\mathbf{r}}_1(0) + \tilde{\mathbf{u}}(0)_1\,\tilde{t}_{12}, \tag{2.6b}$$

$$\tilde{\mathbf{r}}_2(t_{12}) = \tilde{\mathbf{r}}_2(0) + \tilde{\mathbf{u}}(0)_2\,\tilde{t}_{12}, \tag{2.6c}$$

$$\left|\tilde{\mathbf{r}}_{12} + \tilde{\mathbf{u}}_{12}\,\tilde{t}_{12}\right|^2 = \tilde{d}^2, \tag{2.6d}$$

$$\tilde{t}_{12} = \frac{-\tilde{b}_{12} - \left[\tilde{b}_{12}^2 - \tilde{\mathbf{u}}_{12}^2\left(\tilde{\mathbf{r}}_{12}^2 - \tilde{d}^2\right)\right]^{1/2}}{\tilde{\mathbf{u}}_{12}^2}, \tag{2.6e}$$

where $\tilde{b}_{12} = \tilde{\mathbf{r}}_{12}\cdot\tilde{\mathbf{u}}_{12}$. Since $\tilde{t}_{12} > 0$ for a collision to occur, we see that the condition $\tilde{b}_{12} < 0$ must be satisfied. That is if $\tilde{b}_{12} > 0$, the particles are moving away from each other and there is no possibility of collision. If the condition $\tilde{b}_{12} < 0$ is satisfied, then the discriminant in the $\tilde{t}_{12}$ should satisfy $\tilde{b}_{12}^2 - \tilde{u}_{12}^2\left(\tilde{r}_{12}^2 - \tilde{d}^2\right) \geq 0$. Since the equation for $\tilde{t}_{12}$ is quadratic, two roots are obtained, the smaller one corresponds to the physically significant collision because the disks are impenetrable.

2.3 Simulation algorithm

The billiard ball algorithm of Lubachevsky [51] has been implemented in the present problem to simulate hard disks. In this section we would like to discuss this algorithm in detail and then suggest the necessary modifications to simulate a gravity-driven Poiseuille flow in the next section.

A naive serial algorithm advances the state of the billiards from one collision to another. The states of all N balls are examined and updated at times $t_0 \leq t_1 \leq t_2 \leq ...$, where t_0 is the initialization time and t_{i+1} is the nearest next collision time seen at time t_i. This naive scheme is inefficient and expensive for large N because

the following reason:
(a) the same collision is repeatedly scheduled an order of N times until it occurs,
(b) in a typical cycle, most balls are not participating in collisions; still, they are examined by the algorithm.
Aside from costly actions (a) and (b), there exists another problem (c) of finding an inexpensive method of determining the nearest collision for a chosen ball. A straight-forward method is to compare the chosen ball with $N - 1$ others.

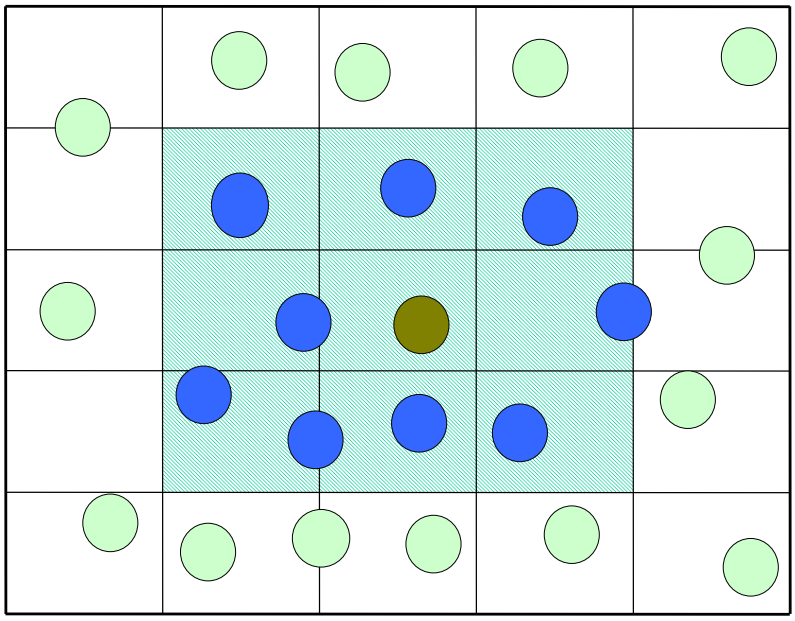

Figure 2.2: Division of simulation box into smaller cells. To predict the next event of particle in red colour, only those particles (blue colored) whose centers lie in the shaded neighbouring cells are considered for computing the collision time. In addition to particle collisions, time required to cross the cell boundaries have to taken into account to predict the next event.

An improvement in the method proposed in [51] is achieved by dividing the simulation domain into cells of $O(N)$ as shown in Fig. 2.2. Only balls in the neighboring cells need to be checked to determine the immediate collision which reduces the work from $O(N)$ to $O(1)$ per one collision scheduled. A natural idea for improvement in (a) and (b) is to postpone examining and updating the state of a ball until its collision. Suppose at time t an event involving ball A is processed, only the state of A is examined and explicitly modified. The states of most other balls at t are not examined by the algorithm. In the present algorithm at any instant two copies of the global state vector, the old and the new, are maintained so that the new vector is computed on the basis of the old one and, in turn, becomes the old one during the next cycle. The attraction of this algorithm is that it utilizes

a simple and easy to handle double-buffering data structure, while avoiding costly actions (a) and (b). Problem (c) is handled in the algorithm using the standard technique of cell division. In most cases the algorithm examines and processes only the events whose processing is unavoidable, e.g., ball collisions and boundary crossings. The processing of cell crossing naturally become additional operations in this method and their processing constitute the methods overhead. However the practical gain in the method is high. Theoretically, the cost reduces to $O(1)$ when using this method. Sometimes, like the naive algorithm, it also processes events whose examining is not necessary. However, the fraction of such overhead events is less than 15% in most experiments, and does not grow with N, while the speed-up due to the simplicity of data handling is substantial. The proposed algorithm achieves the same theoretical optimal performances as other published algorithms [77], i.e., $O(logN)$ instructions per one processed event with cell division and $O(N)$ without.

2.3.1 Basic operations or events

As stated earlier, in event-driven simulation one needs to predict and process a sequence of discrete events. The basic operations or events performed in the simulation are listed below:

(*a*) *Interaction time(state1, time1, state2, time2)* : Given the state of*particle1* at *time1* and the state of *particle2* at *time2*, computes the time of next potential interaction while ignoring the presence of other particles. The state of a particle refers to the velocity and position of the particle. The interaction time is computed using the equations mentioned in Eq. 2.6e.

(*b*) *Jump(state1, state2)* : When two particles collide only their velocities experience a jump and not their positions. Given the state of the interacting particles *1* and *2*, this operation computes the new states of the particles after collision. The collision rules given by Eq. 2.4 are used to find the post collisional velocities.

(*c*) *Advance(state0, time0, time1)* : Given the state of a particle at *time0* and a value *time1* $>$ *time0*, computes the new state of the particle at *time1* ignoring the possible interactions with other particles. Periodic boundary conditions are applied whenever a particle is advanced. A pictorial representation of the periodic boundary condition is given in Fig. 2.3.

d) Boundary crossing of a cell or simulation domain is also considered as an event. When a particle crosses the boundary of simulation domain it reappears at the opposite side due to periodic boundary condition. Whenever a particle crosses the boundary it moves to a new cell and such an event is be examined by the algorithm in order to update the membership in the cells. All such events are treated as one-component interactions. The basic functions with the same names *Interaction time* and *Jump* represent one-component interactions. *Interaction time (state1, time1, obstacle)* and *Jump(state, obstacle)*, where *obstacle* is the identification of a

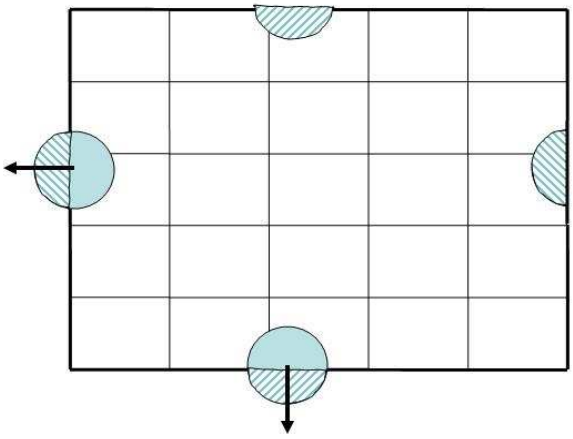

Figure 2.3: Schematic diagram of periodic boundary condition. Whenever a particle crosses the boundary of the simulation box, it enters at the opposite boundary as shown in the figure. In the figure the periodic boundary conditions are applied along both x & y directions.

boundary or an immobile obstacle or a demarcation line (like wall).

2.3.2 Data organization

The basic data unit of the algorithm is called event and has the following format

$$event = (time, state, partner),$$

where *time* is the time to which state of a component corresponds. Note that *state* is the new state of the component immediately after the event, *e.g.*, if a ball has experienced a collision at time, the velocity-coordinate of the state is the new velocity vector after the collision; *partner* identifies the other component, if any, involved in the event. If there is no partner in the event, the program assigns a special no-value symbol to the *partner* coordinate. If $time = \infty$, then the other three coordinates in the event have no value, *i.e.*, $state = type = partner = \Lambda$. At any stage of simulation, the algorithm maintains two events for each component: an old, already processed in the past event and a new, next scheduled event. This information is stored in array *event[1 : N, 1 : 2]*, where N is the number of components of the simulated system. Two arrays *new[1 : N]* and *old[1*

: N] with elements equal *1* or *2* are maintained. The value *new[i]* is the pointer to the new event for component i and the value *old[i]* is the pointer to the old event for component i, so that new event for component i is stored at *event[i, new[i]]* and old event for component i is stored at *event[i, old[i]]*. When *new[i]* is updated, *old[i]* is updated immediately after, so that relation *new[i] + old[i] = 3* remains invariant.

2.3.3 Description of algorithm

We start with particle positions on a rectangular lattice and velocities assigned from Gaussian distribution of unit variance. The new and old states of the particles are same at $t = 0$, time of next event of all the particles is initially set to zero and partners are assigned no value symbol.

The main cycle essentially consists of two steps:
(a) selecting the next component i^* to process its event,
(b) processing the event. Processing of the event comprises of executing the current event of the particle and scheduling the next event for the chosen particle and for the partner involved, if any.

The particle i^* is advanced to a new state using *advance* operation and a $jump$ operation, in case of a collision, or a one-component event such as boundary crossing is executed. Scheduling next event for the particle involves computing nearest next interaction times P_{ij} and Q_{ik}. The short-hand notations P_{ij} and Q_{ik} are defined as:

$$P_{ij} \stackrel{\text{def}}{=} Interactiontime(state[i, old[i]], time[i, old[i]], state[j, old[j]], time[j, old[j]]),$$

where $1 \leq i, j \leq N$ and

$$Q_{ik} \stackrel{\text{def}}{=} Interactiontime(state[i, old[i]], time[i, old[i]], k),$$

where $1 \leq i \leq N$ and $1 \leq k \leq K$. There are two main cases in such scheduling depending on the type of the future event:
1. when $Q_{ik} < P_{ij}$, scheduling an interaction which involves only the chosen component i;
2. when $Q_{ik} \geq P_{ij}$, scheduling an interaction which involves also a second party j and may involve a third party m, the previous partner, if any, of j.

Note that for a small number of balls, say $N = 10$, the best way to find the minimum time is to use the straight-forward element-by-element testing. Such straight-forward method to find the minimum of $time[i, new[i]]$ for i ranging from 1 to N requires $O(N)$ operations per event. Instead, the algorithm organizes values $time[i, new[i]]$ into an implicit heap structure with two pointer arrays $pht[1 : N]$ and $pth[1 : N]$ so that $time[pht[m], new[pht[m]]]$ is the value which is implicitly located at the m-th position of the imaginary heap array and pth is the inverse

map for pht, *i.e.*, $pth[pht[m]] = m$ for all m. In particular, $time[pht[1], new[pht[1]]]$ corresponds to the heap tree root, *i.e.*, the minimum value. We can then simply write

$$i^* \leftarrow pht[1],$$
$$current\ time \leftarrow time[i^*, new[i^*]]$$

The overhead for this computationally cheap method of finding the minimum is the need to update the heap structure, *i.e.*, arrays pht and pth, each time a value of $time[i, new[i]]$ is changed in other sections of the algorithm. The total cost of finding the minimum next event time thus runs to as much as $O(logN)$ operations per one event. For a large N, the cost $O(logN)$ is still much smaller than the original cost of $O(N)$.

The simulation space is divided into cells and only the particles or obstacles incident to the neighboring cells are examined, as shown in Fig. 2.2. The cell boundaries naturally become additional obstacles in this method and their processing constitute the methods overhead. However the practical gain in the method is high. Theoretically, the cost reduces to $O(1)$ when using this method. Among the available grids used for planar cell division, the grid of equal squares is the most convenient. Specifically in the case of equal balls, square sides larger than the ball diameter are chosen, and for each square a membership linked-list [5], is maintained to track the balls whose centers lie in this square. Processing of a square boundary crossing is accompanied by the update of the two lists. Only those P_{i^*j} are computed and are subject to minimization, for which the center of ball j belongs to one of the nine cells neighboring (9 in 2D and 27 in 3D) the one whose member is i.

2.4 Gravity-driven granular Poiseuille flow

The simulated system is a channel of length L along the periodic x-direction and bounded by two plane solid walls, parallel to the x-direction, with a separation of width W (along the y-direction). The granular material consists of N identical rigid and smooth disks of equal mass $\tilde{m}$ and diameter $\tilde{d}$. Since the collisions are inelastic, the kinetic energy is quickly dissipated and the particles come to rest, so to maintain a steady state there has to be a continuous injection of energy into the system. In the present simulation, the gravity acts as a body force on all the particles and prevents the collapse of system to a state of rest. For the ease of understanding, the geometry of the flow is shown in Fig. 2.4.

The control parameter associated with the flow are: volume fraction of particles,

$$\nu = \pi N/4\,(L/W)\,(W/d)^2\,, \tag{2.7}$$

the normal restitution coefficient (e_n) that characterises the loss due to particle-particle collision and the tangential restitution coefficient (β_w) that characterises

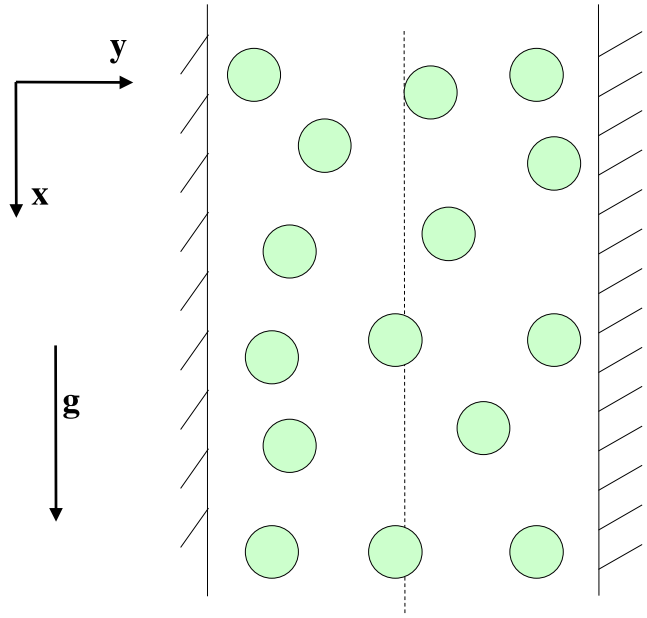

Figure 2.4: Schematic diagram of a gravity-driven granular Poiseuille flow.

the loss due to wall-particle collision.

The collision dynamics and billiard ball algorithm needs to be modified to simulate gravity-driven plane Poiseuille flow due to the presence of gravity and walls. These modifications are discussed in the following paragraphs. Before proceeding further, We would like to make a note about the inelastic collapse. The problem of inelastic collapse is a numerical artifact that is frequently encountered in simulations [56, 57, 99], wherein two particles collide infinitely often in finite time. It has been handled in the present simulation by implementing the *TC model* proposed by McNamara & Luding [54].

Body force due to gravity

Extending the hard-sphere method to include the effect of uniform gravitational field is a simple exercise. Between collisions, the particles follow parabolic rather than linear trajectories. The particle trajectories in Eqs. 2.6b, 2.6c are modified to :

$$\tilde{\mathbf{r}}_1(t_{12}) = \tilde{\mathbf{r}}_1(0) + \tilde{\mathbf{u}}(0)_1\, \tilde{t}_{12} + \frac{1}{2}\tilde{\mathbf{g}}\, \tilde{t}_{12}^2, \tag{2.8a}$$

$$\tilde{\mathbf{r}}_2(t_{12}) = \tilde{\mathbf{r}}_2(0) + \tilde{\mathbf{u}}(0)_2\, \tilde{t}_{12} + \frac{1}{2}\tilde{\mathbf{g}}\, \tilde{t}_{12}^2. \tag{2.8b}$$

But the most important fact is that the collision prediction process is not affected because the same uniform acceleration is experienced by all the particles, and so the computation for determining the existence of a collision and when it occurs is same as given by Eq. 2.6e. Between collisions, the particles follow parabolic rather than linear trajectories.

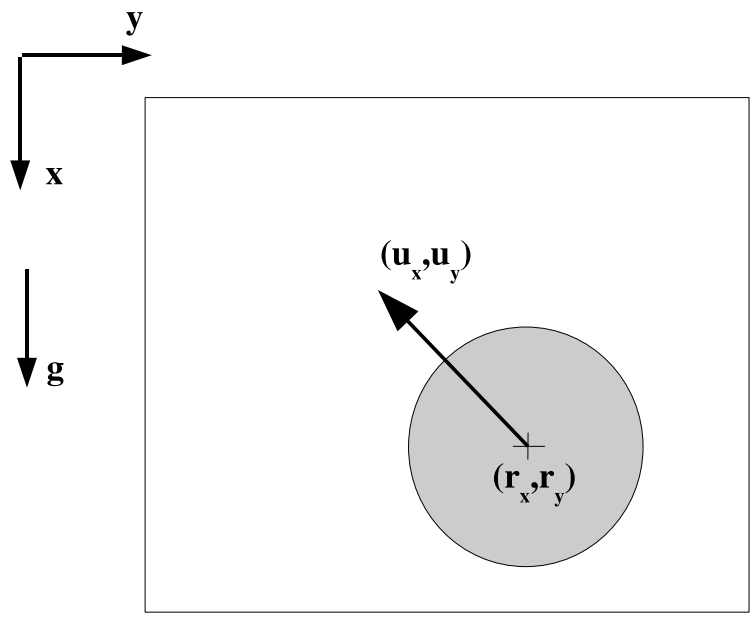

Figure 2.5: The motion of a particle in a cell, in the presence of a body force. Both the upper and lower cell boundaries have to be considered to compute the cell crossing time.

It is only the prediction of cell crossing that calls for special attention because parabolic motion means, for example, that it is possible for a particle to leave a cell through the face of its entry. For example, consider a particle moving in the negative $x-$ direction as shown in the Fig. 2.5. Since the motion of this particle is against gravity, the direction of u_x velocity may reverse after traversing a certain distance, so the times for crossing both the upper and lower cell boundaries need to be computed. There is no body force acting along the $y-$ direction, so the motion in this direction remains unaffected.

Boundary conditions

Due to the presence of walls in $y-$ direction, the simulation domain is periodic only along $x-$ direction. The solid walls are modeled as frictional surfaces, and a particle colliding with a wall is analogous to a particle colliding with a particle of infinite mass moving at the velocity of the wall. A parameter, *coefficient of tangential restitution* for particle-wall collisions β_w, has been used to model the

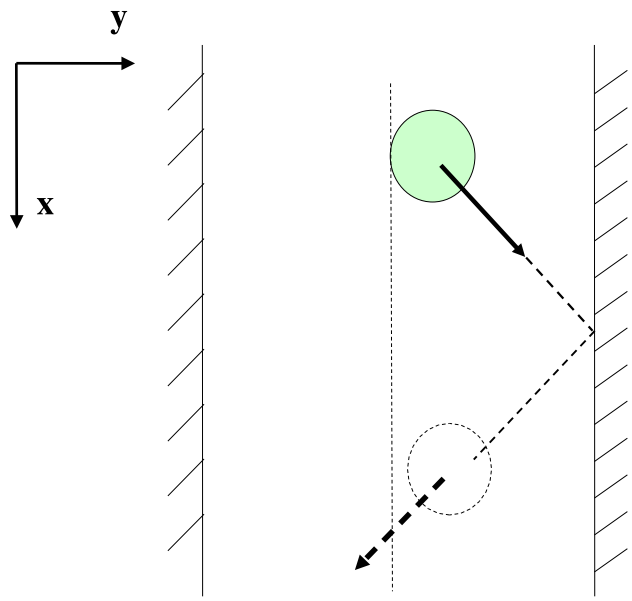

Figure 2.6: Schematic of a wall-particle collision. The particle loses a fraction of streamwise and transverse momentum upon collision with the wall. The loss of streamwise momentum is characterised by *tangential restitution coefficient* for wall-particle collision, β_w, while the the loss of transverse momentum is characterised by normal restitution coefficient for wall-particle collision, e_w.

frictional properties of walls. It is defined as the fraction of relative tangential momentum transmitted from a particle to the wall during a particle-wall collision. The collision rule of a particle-wall collision is given by :

$$\tilde{u}_x = \beta_w \tilde{u}_x \quad , \quad \tilde{u}_y = -e_w \tilde{u}_y, \tag{2.9}$$

where e_w is the coefficient of normal restitution for wall-particle collision, set to unity in the present work. The wall-roughness is controlled by choosing a specific value of β_w. When $\beta_w = 1$ the walls are fully *smooth* and the slip at walls is maximum. At $\beta_w = 0$ the dissipation at walls is maximum and there is no relative tangential slip between the particle surface and the wall upon a wall-particle collision. It is observed that even when $\beta_w = 0$ there is a finite slip at walls. In order to impose no-slip boundary condition for fully *rough* walls the particles trajectories are usually reversed after collision which corresponds to a value of $\beta_w = -1$. Imposing the no-slip boundary condition at walls using $\beta_w = -1$ is a common practice in MD simulations of fluids.

2.5 Method of averaging

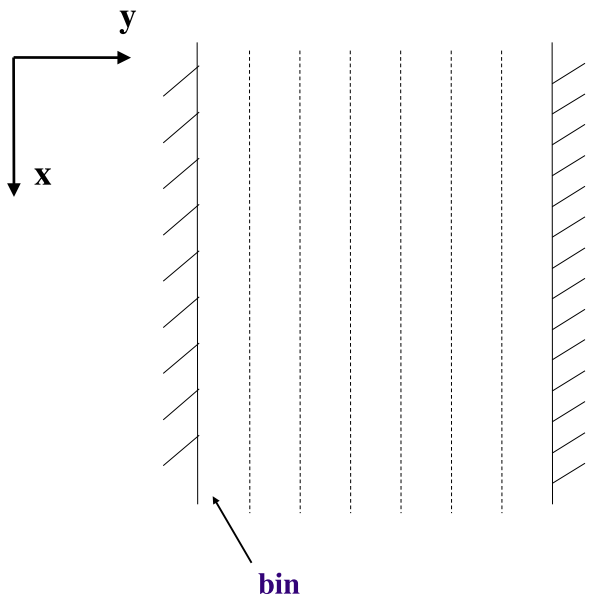

Figure 2.7: Schematic diagram of the division of channel into bins in the $y-$ direction.

As discussed in an earlier section, energy enters into the system due to the acceleration of particles by gravity and is lost due to inelastic collisions. When the two processes *i.e.*, the production and dissipation, balance each other, a steady state is obtained. The statistical measurements of various quantities are performed only after the system has attained a steady state. In a steady state, the macroscopic properties of the mean flow : streamwise velocity (U_x), volume fraction (ν) and granular temperature (T), remain invariant in time, but have spatial variations along the (x & y) directions. All the statistics presented in this paper were computed 'bin-wise' by dividing the channel into several bins, typically of one particle diameter, along the wall normal direction, as shown in Fig. 2.7. The data in each bin is averaged over a large number of collisions, depending on the control parameters and quantities to be measured. The number of collisions considered for computing rheological quantities and slip velocity was around 10000 collision per particle. A relatively large number of collisions, about 300000 collisions, were considered for computing the local velocity distributions in order to capture the velocities in the tail region.

Analogous to molecular gases, the random velocity associated with granular particles is used to define the granular temperature T in Eqn. 2.10e. The method of averaging followed for computing macroscopic properties of mean flow is given below :

$$u_i(t) = c_i(t) - U_x(y_i, t) \tag{2.10a}$$

$$U_x(y_i, t) = \frac{1}{N_y} \sum_{N}^{i=1} c_i(t)\delta(y - y_i) \tag{2.10b}$$

$$U_x(y) = \langle U_x(y_i, t) \rangle \tag{2.10c}$$

$$\nu(y) = \frac{\pi}{4} d^2 \left\langle \frac{1}{A_y N_y} \sum_{N}^{i=1} \delta(y - y_i) \right\rangle \tag{2.10d}$$

$$T(y) = \left\langle \frac{1}{2 * N_y} \sum_{N}^{i=1} u_i(t) u_i(t) \delta(y - y_i) \right\rangle \tag{2.10e}$$

where $c_i(t)$ is the instantaneous velocity of a particle, $u_i(t)$ is the fluctuating velocity of the particle, $U_x(y_i, t)$ is the instantaneous mean velocity in the bin corresponding to the position y_i of the particle and $\langle .. \rangle$ represents time average. Other properties of interest were computed in a similar way.

2.6 Verification of code

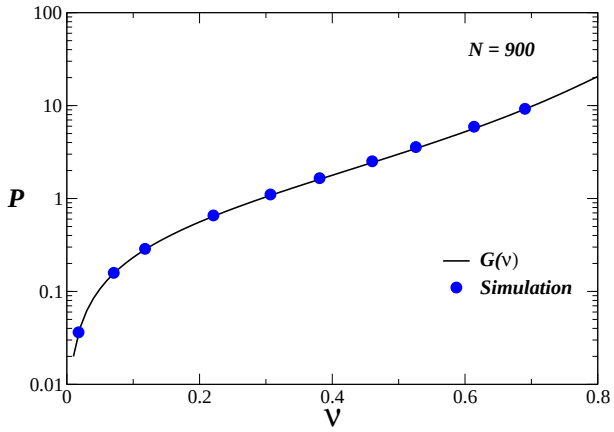

Figure 2.8: Variation of pressure with volume fraction for hard disks. The continuous line represents theoretical results given in Ref. [52] and the symbols are obtained from simulations.

The $2 - D$ code for billiard balls or elastic hard disks, with periodic boundary condition along both x & y directions, was verified by computing pressure at different volume fractions. These results, shown in Fig. 2.8, are in excellent agreement with the theoretical results obtained from the global equation of state for two-dimensional hard sphere systems [52].

Since there are no standard results available for a plane Poiseuille flow in the literature, we have compared the results obtained from the billiard ball algorithm and the FORTRAN code given in Ref. [5]. A comparison of the temperature profile at a volume fraction of $\nu = 0.56$ and coefficient of restitution of $e_n = 0.99, 0.80$ for smooth walls ($\beta_w = 0.9$) and rough walls ($\beta_w = 0.1$) is shown in Fig. 2.9; there is a good agreement between the results obtained from both methods. For each case, the steady state was ascertained by monitoring the constancy of the average kinetic energy (per particle) or the average granular temperature, see Fig. 2.10. In this figure, the main panel shows the time trace of average kinetic energy (computed based on the instantaneous velocities) : $E = \frac{1}{2N}\sum U_\alpha^{i2}$, while the inset shows the time trace of granular temperature for $\nu = 0.56$, $\beta_w = 0.9$ and $e_n = 0.99, 0.80$.

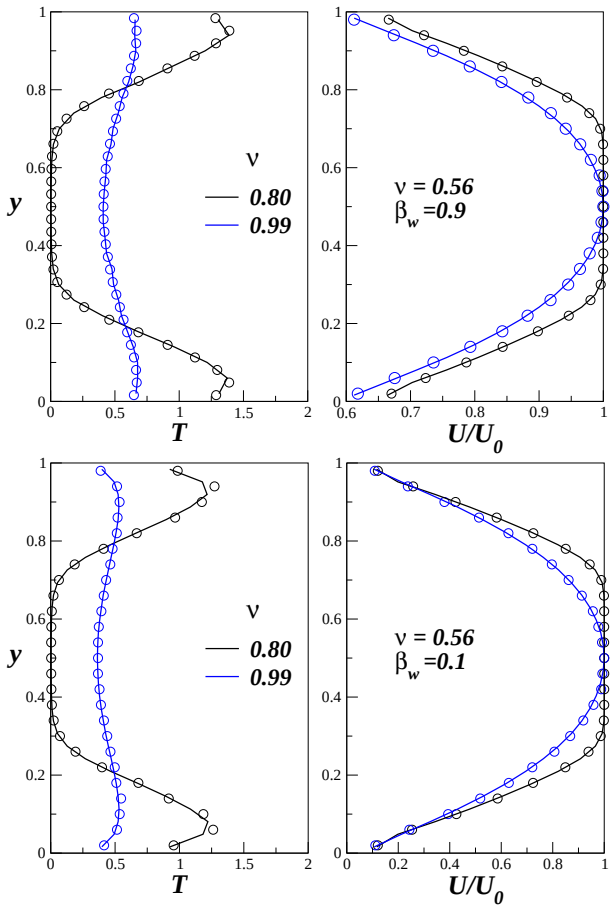

Figure 2.9: Comparision of temperature and velocity profiles obtained using the alogrithm given by Lubachevsky [51] (solid lines) and the code given in Ref. [5] (symbols), for (a) smooth walls ($\beta_w = 0.9$) and (b) rough walls ($\beta_w = 0.1$). at $\nu = 0.56$ and $e_n = 0.99, 0.80$.

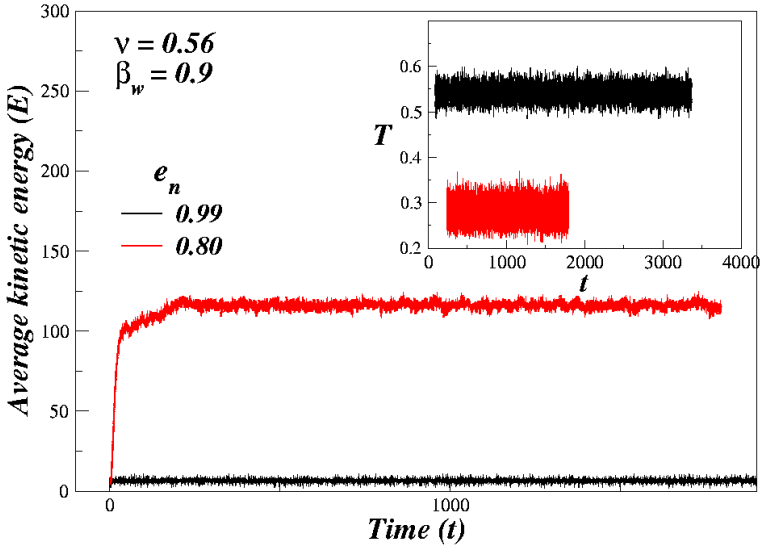

Figure 2.10: Main panel displays the variation of average kinetic energy and the inset displays the variation of temperature with time for $\nu = 0.56$, $\beta_w = 0.9$ and $e_n = 0.99, 0.80$.

CHAPTER 3

VELOCITY DISTRIBUTION FUNCTION AND CORRELATIONS

In the rapid flow regime [30, 45], the theory for flowing granular materials is largely based on the dense gas kinetic theory that incorporates the *inelastic* nature of particle collisions. At the heart of such gas- or liquid-state continuum theories lies the concept of 'coarse-graining' over distribution functions while making a transition from the particle-level properties to the macro-scale fields. Unlike the molecular fluid for which the Maxwell-Boltzmann (Gaussian/Maxwellian) distribution plays the role of the 'equilibrium' distribution function, however, the granular fluid does not possess any 'equilibrium' state [30, 45, 85] due to the microscopic dissipation of particle collisions. However, there are 'non-equilibrium' (driven) steady-states for various canonical granular flow configurations for which the Gaussian distribution is the leading-order velocity distribution [85] in appropriate limits. A systematic study of distribution functions is, therefore, of interest from the viewpoint of developing constitutive models for granular flows as well as to pinpoint the range of validity of any adopted theory. Another important issue that needs attention is the derivation of continuum boundary conditions for granular flows [40, 78] where it is generally assumed that the distribution function in the near wall-region is the same as that in the bulk which is unlikely to hold as we shall show here.

In 'driven' granular flows, the deviation of velocity distribution from a Gaussian has been studied through theory [28, 85, 93], simulation [16, 32, 64, 75, 88, 94] and experiment [9, 11, 50, 63, 68, 81]. Esipov and Poschel [28] have solved the Boltzmann equation for inelastic hardspheres at large velocities. For the freely evolving system, they found a spatially homogeneous distribution function for which the large velocities decay as $f \sim exp\,(-Av)/v_0(t))$, where $v_0(t)$ is the time dependent thermal velocity and $A \sim 1/\epsilon$ a constant, related to the inelasticity $\epsilon = 1 - e_n^2$, defined in terms of the coefficient of normal restitution e_n. For a rapid flow of smooth, inelastic spheres, Sela & Goldhirsch [85] solved the Boltzmann equation perturbatively upto third order by performing a double expansion of velocity distribution in Knudsen number (Kn) and the degree of inelasticity (ϵ). The solution at the order $O(\epsilon)$ estimates the deviation from Gaussian behaviour. The single particle velocity distributions for homogeneous granular fluids of inelastic hard spheres were studied, based on the Enskog-Boltzmann equation for the unforced and heated case by Noije and Ernst [93]. They showed that velocity distribution in the heated steady state exhibits a high energy tail $\sim exp(-Ac^{3/2})$, where c is the velocity scaled by the thermal velocity and $A \sim 1/O(\epsilon)$ with ϵ being the degree of inelasticity. Moon *et*

al. [64] investigated the steady state velocity distributions in three-dimensions using molecular dynamics simulations for homogeneously heated granular media. The high energy tails were consistent with $\sim\ exp(Ac^{3/2})$ for $e < 0.5$ that qualitatively agree with the theoretical results [93]. A simulation of two-dimensional granular gas subject to multiplicative driving proportional to $|v(x)|^{\delta}$ of the local particle velocity $v(x)$ was performed in Ref. [16]. The tails of the velocity distributions were found to be non-Gaussian, $f(v_x) \sim exp\,(-B|v_x - < v_x >|^{\alpha})$, with the exponent α varying continuously between 0.5 and 2 as a function of coefficient of restitution e_n. In Ref. [88] it has been shown that the velocity fluctuations in a vibrated bed of particles follow a Gaussian distribution in the solid phase and a power-law distribution (with an exponent -3) in the fluidized phase. For the plane shear flow [32], the velocity distribution function is well fitted by an exponent of a second-order polynomial in the norm of the fluctuating velocities with angle-dependent coefficients. Experiments [50, 81] for a granular gas confined between two vertical plates and driven into a steady state via vertical vibrations have shown that $P(v) \sim exp\ (-\gamma v^{\alpha})$ with an exponent $\alpha \sim 1.55 \pm 0.1$, for a wide range of frequency and amplitude of vibrations. Some recent experiments [9, 11], however, showed that the high-velocity tails cannot be described by a 'single' universal exponent.

3.1 Velocity distributions in quasi-elastic limit

We have performed most of the simulations by fixing particle number at $N = 900$ and the aspect ratio at $W/d = 31$. So, N and W/d are assumed to be fixed at these values, unless otherwise stated explicitly. To change the volume fraction, L/W ratio was varied. The binwise volume fraction in the simulations is obtained using the following expression :

$$\nu(y) = \frac{\pi}{4} d^2 \left\langle \frac{1}{A_y N_y} \sum_{N}^{i=1} \delta(y - y_i) \right\rangle, \tag{3.1}$$

where d is the diameter of the particle, N_y is the number of particles in the bin and A_y is the area of the bin.

3.1.1 Smooth walls

The mean field quantities such as temperature (T), mean velocity (U_x) and volume fraction (ν) at $e_n = 0.99$ for smooth walls ($\beta_w = 0.9$) are shown in Fig. 3.1. They develop considerable gradients along $y-$direction with increasing density and this is more pronounced for U_x, see lower inset in Fig. 3.1.

In order to avoid the effects of inhomogenities, a localised, binwise study of velocity distributions is presented. The division of simulation domain into bins is

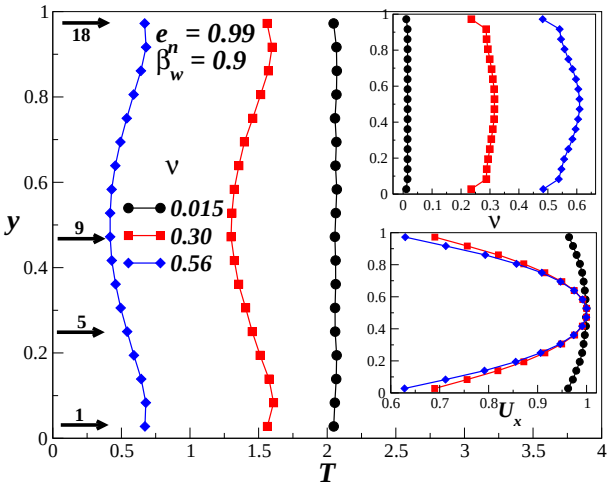

Figure 3.1: The mean velocity (U_x), granular temperature (T) and volume fraction (ν) profiles across the width of the channel at $e_n = 0.99$ and $\beta_w = 0.9$, for a range of volume fractions. The arrows near the left-ordinate indicate the locations of some bins.

shown in Fig. 2.7. The number of bins used at a aspect ratio of $W/d = 31$ is 18. An increase in the number of bins did not affect the results significantly but an explicit mention is made wherever the bin number was increased to eliminate the sensitivity of results to bin width. It should be noted that the effects of inhomogenities along $x-$ direction cannot be avoided by carrying out this kind of binwise study. For the ease of understanding the location of few bins are indicated by arrows in Fig. 3.1, with $bin = 1, 18$ being located adjacent to the walls $bin = 5, 14$ in the shear layer and $bin = 9, 10$ at the center of the channel.

Figures 3.2 (a) & (b) show the probability distribution function of the fluctuating streamwise velocity (u_x) and transverse fluctuating velocity (u_y), respectively, for dilute-to-dense flows ($0.015 \leq \nu \leq 0.56$) in different bins. The wall-roughness has been set to $\beta_w = 0.9$ for smooth walls, and the restitution coefficient to $e_n = 0.99$ for *quasi-elastic* particle collisions. The local (bin-wise) distribution functions on only one-side of the channel-centerline are presented as the distributions on the other side is the same; however, in some cases, the distributions on both sides are presented when they differ. Note that the horizontal axis in the velocity distribution plots is scaled by $\sigma_i = \sqrt{\langle u_i^2 \rangle}$, where the index i denotes the coordinate direction, and the vertical axis has been scaled such that $P(0) = 1$. It is remarkable that the u_x distribution function in all bins remains a Gaussian for a wide range of densities ($\nu < 0.6$). This is a surprising result, especially in the dilute limit, since the Knudsen number [see left inset in Fig. 3.2 (a)], which is the ratio between the mean free path and the channel width, $Kn = \lambda/W$, increases with decreasing ν and becomes of $O(1)$ in the dilute limit, signalling the onset of rarefied flow. Even in this rarefied regime, the velocity distribution function remains a Gaussian in granular Poiseuille flow with smooth walls. The other inter-

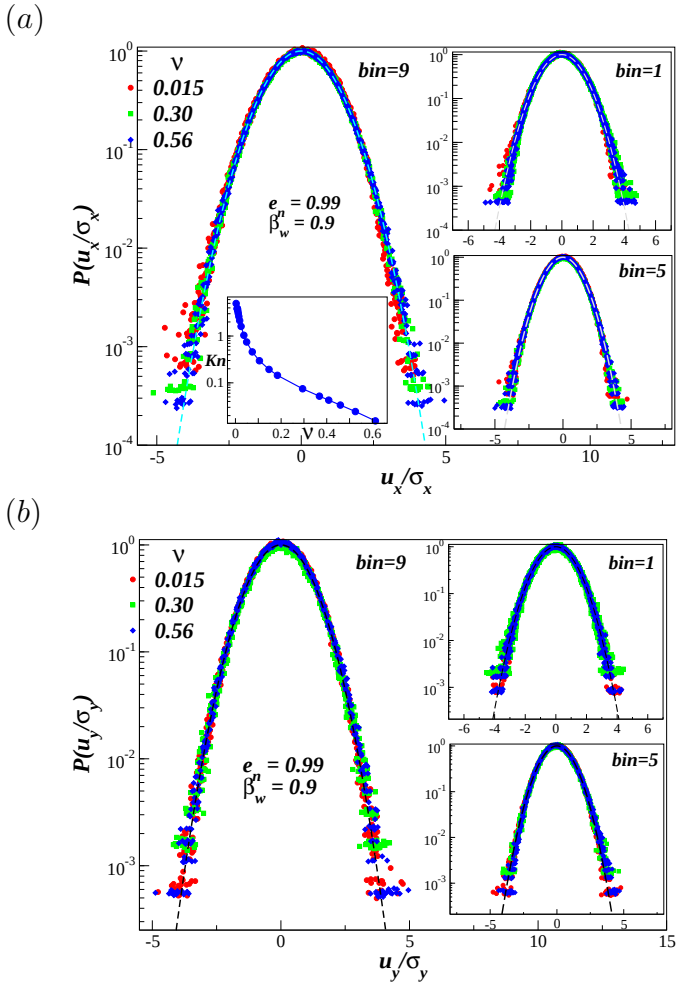

Figure 3.2: Distribution function of (a) u_x and (b) u_y for a range of volume fractions in the quasi-elastic limit ($e_n = 0.99$) for smooth ($\beta_w = 0.9$) walls in different bins. The dashed curve indicates a Gaussian. Left inset in (a) shows the variation of Knudsen number, Kn, with volume fraction. Main Panel: bin=9, Upper Inset: $bin = 1$ and Lower Inset: $bin = 5$.

esting observation is that the mean-field gradients do not seem to play any role in determining the form of 'local' velocity distribution functions as long as the walls are smooth and the particle collisions are quasielastic.

In order to quantify the degree of deviation of distributions from Gaussian, we have computed the kurotsis, which is given by the expression :

$$\kappa = \frac{\mu_4}{\mu_2^2},$$

where $\mu_4 = \int_{-\infty}^{\infty}(x-\bar{x})^4 f(x)dx$ and $\mu_2 = \int_{-\infty}^{\infty}(x-\bar{x})^2 f(x)dx$ are the fourth and second moments about mean of the distribution, respectively. For a normal distri-

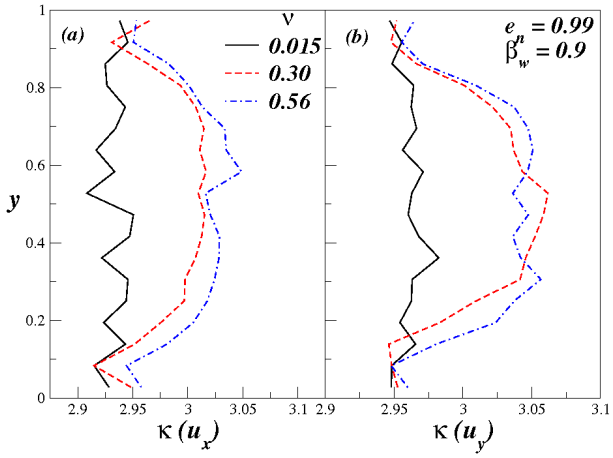

Figure 3.3: Kurtosis (κ) of (a) $P(u_x)$ and (b) $P(u_y)$ distributions for the parameter values given in Fig. 3.2.

bution, the kurtosis is 3. The kurotsis of $P(u_x)$ and $P(u_y)$ distributions in each bin is shown in Figs. 3.3 (a) & (b), respectively, for the parameter values used in Fig. 3.2. We see that kurtosis is close to ~ 3 in all the bins, over the range of volume fractions studied here. Hence the distributions are indeed close to Guassian in the quasi-elastic limit for smooth walls.

3.1.2 Rough walls

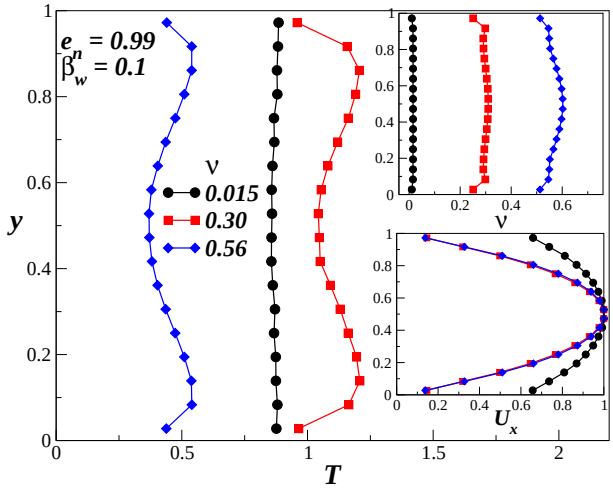

Figure 3.4: The mean velocity (U_x), granular temperature (T) and volume fraction (ν) profiles across the width of the channel at $e_n = 0.99$ and $\beta_w = 0.1$, for a range of volume fractions.

We now look at velocity distribution functions for rough walls. We shall see that

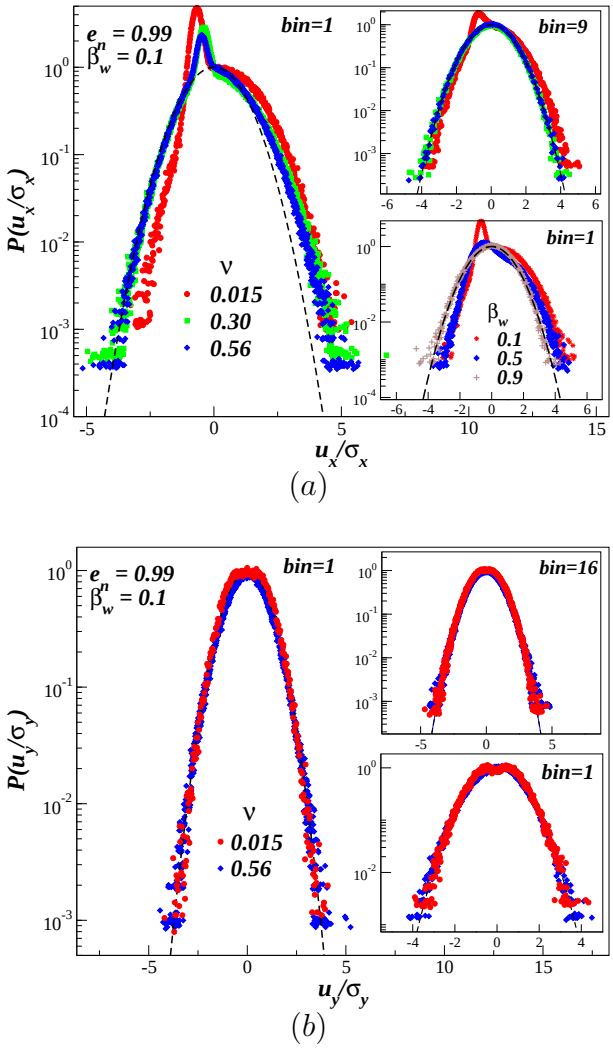

Figure 3.5: Effect of mean volume fraction on (a) $P(u_x)$ and (b) $P(u_y)$ for a rough-wall ($\beta_w = 0.1$) with $e_n = 0.99$ in $bin = 1$. (a) Main Panel: bin=1, Upper Inset: $bin = 9$, Lower Inset: Effect of β_w on $P(u_x)$ at $\nu = 0.015$ in $bin = 1$. (b) Main Panel: $bin = 1$, Upper Inset: $bin = 16$, center of channel. The number of bins used is 31 and $bin = 16$ is located at the center of channel. Lower Inset in (b) : distribution in $bin = 1$ when the number of bins are 18.

a wall roughness of $\beta_w \sim 0$ introduces interesting asymmetric features in u_x distribution, so we would like to concentrate on this particular value of β_w. The mean field quantities and velocity distributions at a wall roughness of $\beta_w = 0.1$, in the quasi-elastic limit ($e_n = 0.99$), are shown in Fig. 3.4 and Fig. 3.5, respectively.

In Fig. 3.5 (a), $P(u_x)$ distribution near the wall ($bin = 1$, the main panel) develops a single-peak asymmetric structure at all densities, with its peak being positioned at some negative velocity. Near the centerline ($bin = 9$, upper inset), however, $P(u_x)$ remains asymmetric only at low densities and becomes a Gaussian

at larger densities. The effect on $P(u_x)$ in $bin = 1$ is shown in the lower inset. It is clear that the asymmetry in $P(u_x)$ diminishes with increasing wall smoothness (β_w) and becomes a Gaussian when the walls are smooth ($\beta_w = 0.9$). The corresponding $P(u_y)$ distribution in Fig. 3.5 (b) remains close to a Gaussian at all densities in the quasielastic limit. Note that to eliminate the effect of bin width on $P(u_y)$ the number of bins were increased to *31* in Fig. 3.5 (b) (main panel and upper inset). For clarity, we show the $P(u_y)$ distribution in $bin = 1$ obtained with 18 bins in the lower inset of Fig. 3.5 (b). The double humped structure of $P(u_y)$ in $bin = 1$ at low volume fraction ($\nu = 0.015$) is clear from Fig. 3.5 (b).

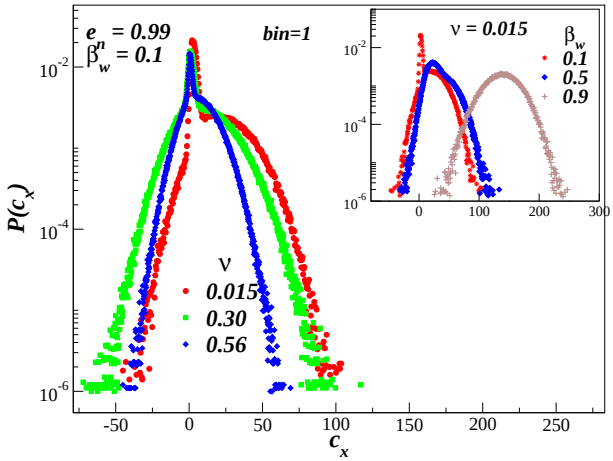

Figure 3.6: Main panel : Distribution function of instantaneous streamwise velocities c_x for a range of volume fractions in the quasi-elastic limit ($e_n = 0.99$) for rough ($\beta_w = 0.1$) walls in $bin = 1$. Inset : Distribution of c_x for a range of wall roughness in the quasi-elastic limit ($e_n = 0.99$) in $bin = 1$.

The wall-roughness-induced asymmetry in $P(u_x)$ is also reflected in the probability distribution of the instantaneous streamwise velocity c_x which is displayed in Fig. 3.6 for $bin = 1$, showing a single peak in the low velocity region. The inset in Fig. 3.6 shows that $P(c_x)$ for $\nu = 0.015$ approaches a Gaussian with increased wall-smoothness. Note that the mean of $P(c_x)$ represents the time-averaged streamwise velocity. Since the particles loose significant amount of tangential velocity on colliding with a *rough* wall in comparison with their collisions with a *smooth* wall, a peak near the low velocity region is expected for rough walls. The greater the loss of tangential velocity at walls, the more is the deviation from a Gaussian, and the related asymmetry in Fig. 3.6 is, therefore, tied to wall-roughness. On the whole, in dilute flows the effect of wall-roughness is felt on the local distribution function $P(u_x)$ throughout the channel, whereas for dense flows only the near-wall region is affected.

The deviation of $P(u_x)$ distribution from a Gaussian due to wall-roughness-induced asymmetry is also apparent from the binwise kurtosis of distributions in Fig. 3.7. It is clear that kurtosis of u_x distribution in Fig. 3.7 (a) deviates from

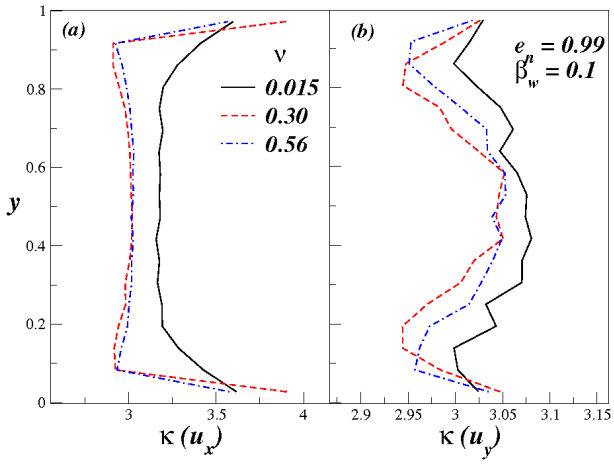

Figure 3.7: Kurtosis (κ) of (a) $P(u_x)$ and (b) $P(u_y)$ distributions for the parameter values given in Fig. 3.5.

3 (kurtosis of a Gaussian distribution) in all the bins for dilute flows, but only in the wall region for moderate and dense flows. On the other hand, kurtosis of u_y distribution in Fig. 3.7 (b) remains close to 3 over the range of volume fraction studied here.

To study the effect of system size and the robustness of results presented so far, we have reproduced some of the plots by increasing the number of particles (N) and aspect ratio (W/d) *i.e.,* particle number was increased by four times from $N = 900$ to $N = 3600$ and the aspect ratio by two times from $W/d = 31$ to $W/d = 62$. A comparison of the results are shown in Fig. 3.8 and Fig. 3.9. We observe that the distributions of u_x and u_y in Fig. 3.8 (a) & (b), respectively, continue to be Gaussian for smooth walls and the wall-roughness-induced asymmetry in u_x distribution for rough walls persists even for larger systems.

3.2 Distributions at higher dissipation

In this section we concentrate on the effect of dissipation on velocity distribution functions. We begin our study by looking at the effect at moderate densities and then move to relatively high densities. An increase in the degree of dissipation gives rise to formation of clusters, which significantly affects various properties of the system [23, 48]. Here we restrict our attention to their effect on velocity distribution alone.

3.2.1 Moderately dense flows

We study moderately dense flow by fixing the volume fraction at $\nu \sim 0.3$. A snapshot of particle positions in the steady state over a range of coefficient of restitution

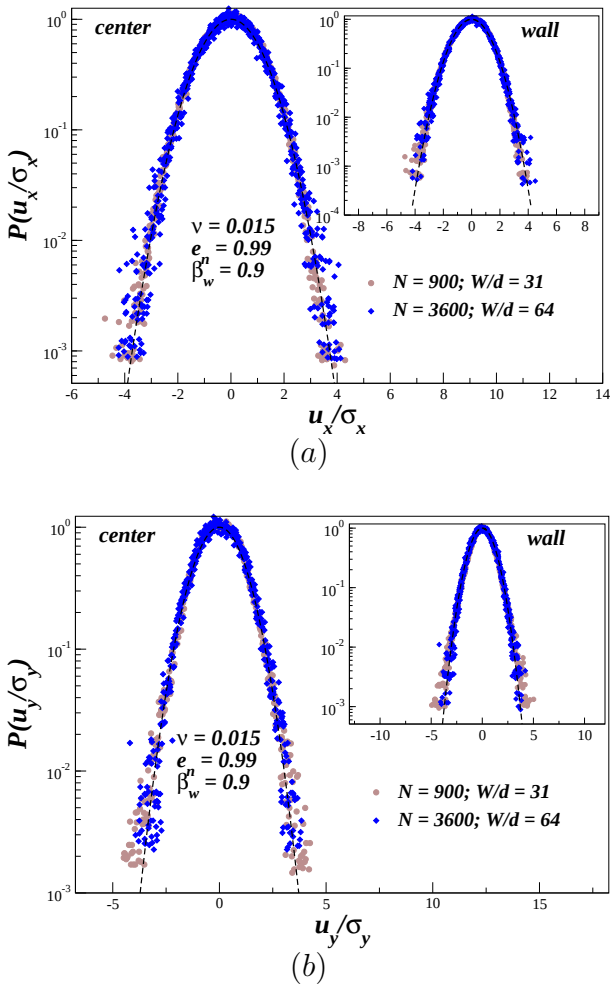

Figure 3.8: Comparison of (a) $P(u_x)$ and (b) $P(u_y)$ distributions obtained by setting $\nu = 0.015$ and $e_n = 0.99$ at different system sizes for smooth walls ($\beta_w = 0.9$). The main panel shows the distributions near the centerline of channel, while the inset shows the distribution in near wall region. The particle number is increased by four times from $N = 900$ to $N = 3600$ and the aspect ratio by two times from $W/d = 31$ to $W/d = 62$.

e_n at a volume fraction of $\nu = 0.30$ for smooth walls ($\beta_w = 0.9$) is shown in Fig. 3.10. We see that at $e_n = 0.9$ and 0.8, the flow is inhomogeneous along both x & $y-$ directions. In Figs. 3.11 (a) & (b), the $P(u_x)$ and $P(u_y)$ distributions for the parameter values of Fig. 3.10 are shown. The $P(u_x)$ distribution is asymmetric in all bins except near the wall, (see the upper inset of Fig. 3.11 (a)), where it is close to a Gaussian. Similarly, $P(u_y)$ is Gaussian near the wall (not shown) and asymmetric in all other bins but its asymmetry changes sign about the channel-centreline. Consider the $P(u_y)$ distribution in $bin = 5$ and $bin = 14$ that are shown in the upper inset and lower inset of Fig. 3.11 (b), respectively. These bins are located symmetrically about the centre of channel and the distributions have

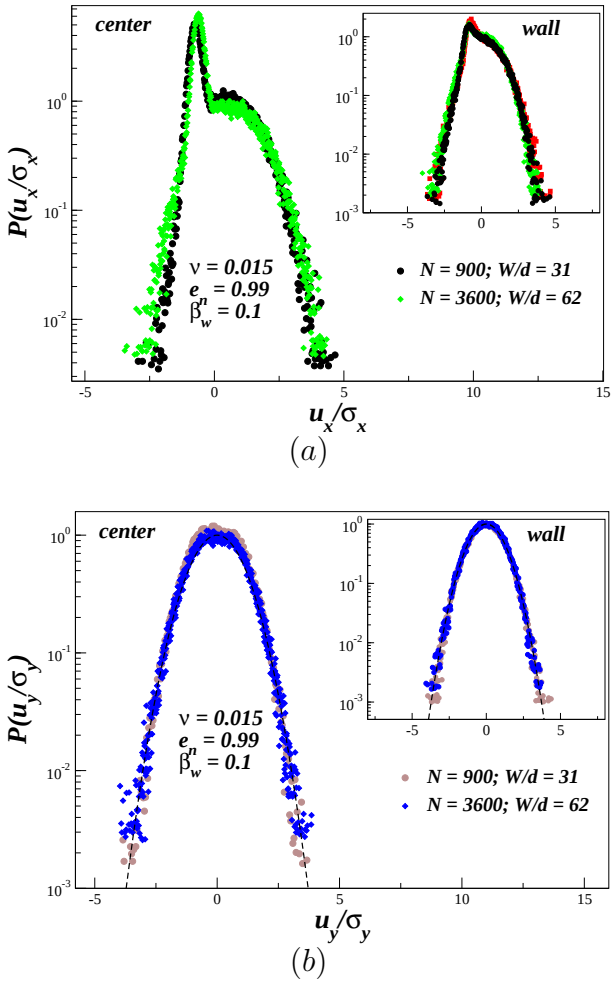

Figure 3.9: Comparison of (a) $P(u_x)$ and (b) $P(u_y)$ distributions obtained by setting $\nu = 0.015$ and $e_n = 0.99$ at different system sizes for rough walls ($\beta_w = 0.1$). The main panel shows the distributions near the centerline of channel, while the inset shows the distribution in near wall region. The particle number is increased by four times from $N = 900$ to $N = 3600$ and the aspect ratio by two times from $W/d = 31$ to $W/d = 62$.

asymmetries in opposite directions.

A study of temporal structures in a gravity-driven channel flow was made by Liss *et al.* [48]. Their phase diagram shows three different kinds of density waves : plug, wave and slug, over a range of volume fractions ($\nu = 0.2 - 0.4$) in the steady state. A plug was observed at small W/d, a wave at intermediate W/d and a slug at higher W/d. We would like to study the way these structures affect the velocity distributions. The volume fraction was fixed at $\nu = 0.3$, coefficient of restitution at $e_n = 0.85$ and W/d at *31* and the parameters L/W and N were varied to get obtain different steady state structures, as shown in Fig. 3.12. A plug was seen at $L/W \sim 1$, a wave at $L/W \sim 2$ and a slug at $L/W > 3$. The macroscopic prop-

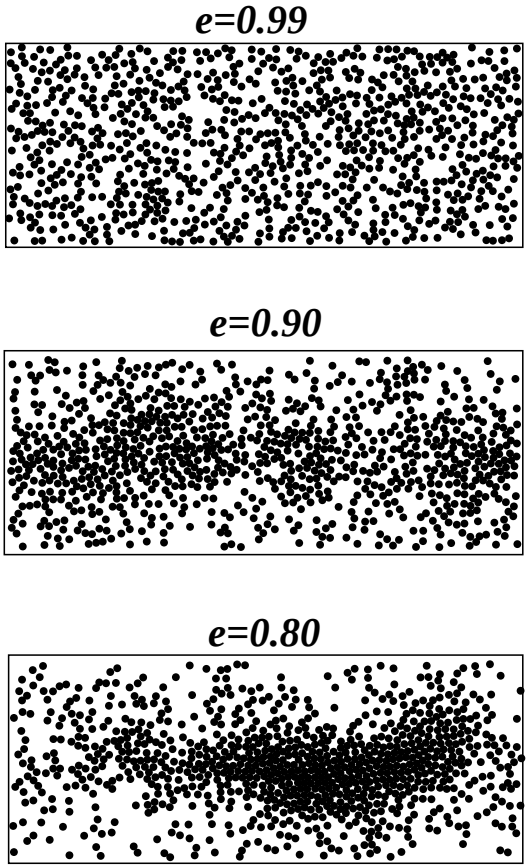

Figure 3.10: Snapshots of particle positions in steady state at $\nu = 0.30$ and $\beta_w = 0.9$, for a range of coefficient of restitution (e_n).

erties and velocity distributions are shown in Fig. 3.13 and Fig. 3.14, respectively. Surprisingly, the profiles of macroscopic properties in Fig. 3.13 are almost identical but the asymmetry associated with velocity distributions near the channel centerline and the shear layer for a slug (Fig. 3.14) is more in comparison to that for a plug or wave. It is a clear indication that the inhomogenities along $x-$ direction enhance the asymmetry of velocity distribution.

3.2.2 Highly dense flows

We discuss the velocity distributions at high densities ($\nu > 0.50$) in the following paragraphs. The L/W ratio at high densities (with $N = 900$) is close to ~ 1, so we expect a formation of plug. Since the region inside the plug is nearly homogenous, the inhomogenities along the $x-$ direction are negligible for dense flows with $N = 900$.

For a dense flow, $\nu = 0.56$, with smooth walls $\beta_w = 0.9$, Fig. 3.15 shows the mean field quantities and Fig. 3.16 (a) shows the effect of collisional dissipation, e_n,

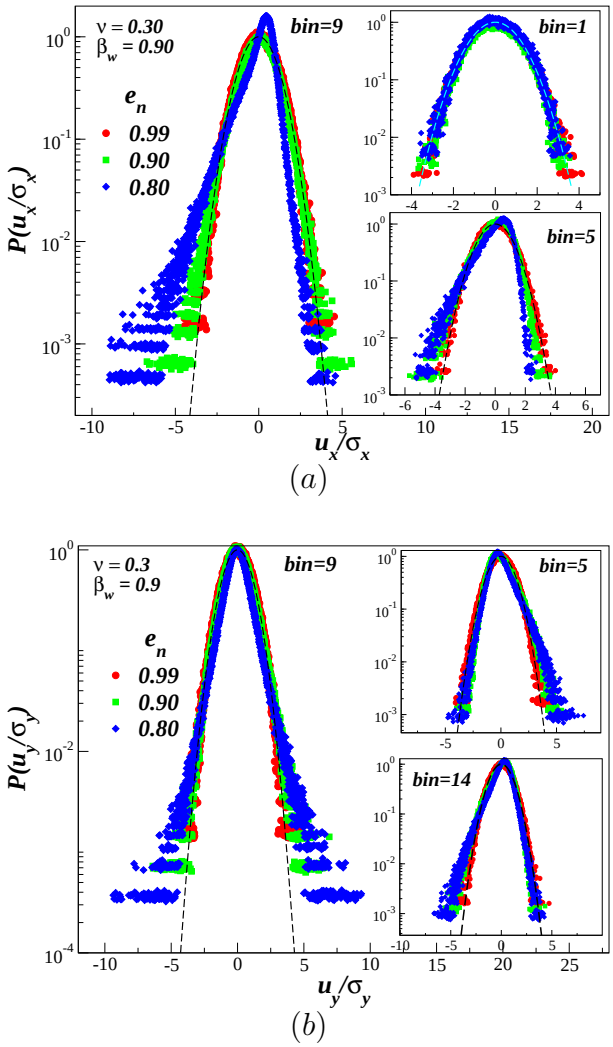

Figure 3.11: Effect of restitution coefficient, e_n, on (a) $P(u_x)$ and (b) $P(u_y)$ at $\nu = 0.30$ for smooth walls ($\beta_w = 0.9$). The velocity distribution in region near wall, $bin = 1$, of both u_x (upper inset in (a)) and u_y (not shown) remain Gaussian. The distribution of u_x at other locations, $bin = 9$ in main panel and $bin = 5$ in upper inset of (a), are asymmetric. Similarly, the $P(u_y)$ distribution is asymmetric at all other locations but the asymmetry in $bin = 5$, upper inset in (b), and $bin = 14$, lower inset in (b), are in opposite direction.

on the form of $P(u_x)$ distribution in different bins. The profiles of the mean field quantities in Fig. 3.15 show the emergence of a 'plug' around the channel-centerline (with negligible gradients in U_x, T and ν) with decreasing e_n, and two 'shear-layers' adjacent to two-walls with steep gradients in U_x, T and ν. The velocity distribution in $bin = 1$ (adjacent to wall), the upper inset in Fig. 3.16 (a), remains close to a Gaussian, irrespective of the value of e_n. The $P(u_x)$ distribution in $bin = 5$ (between the wall and the channel-centerline), the lower inset in Fig. 3.16 (a),

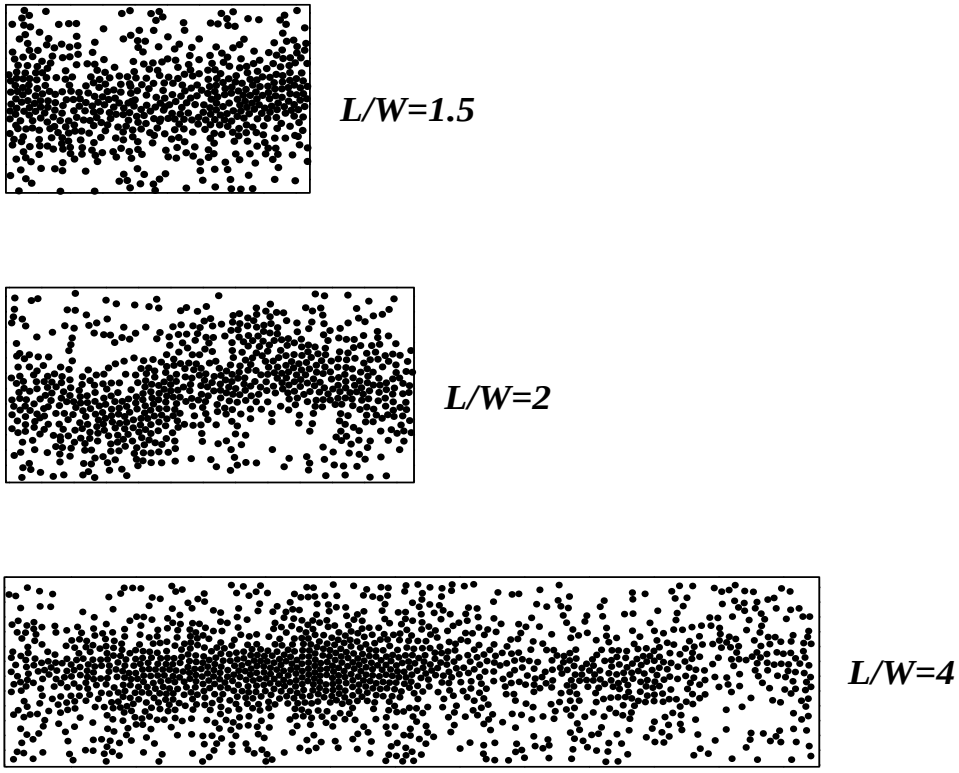

Figure 3.12: Snapshots of different steady state structures at a volume fraction of $\nu = 0.3$, coefficient of restitution of $e_n = 0.85$ and wall roughness of $\beta_w = 0.9$. To obtain different structures, the values of parameters N and L/W were varied.

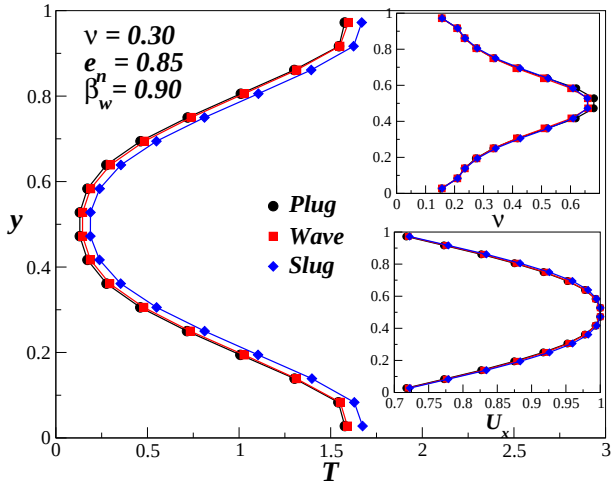

Figure 3.13: The mean velocity (U_x), granular temperature (T) and volume fraction (ν) profiles across the width of the channel for different steady states at a volume fraction of $\nu = 0.3$ and coefficient of restitution of $e_n = 0.85$ for smooth walls ($\beta_w = 0.9$).

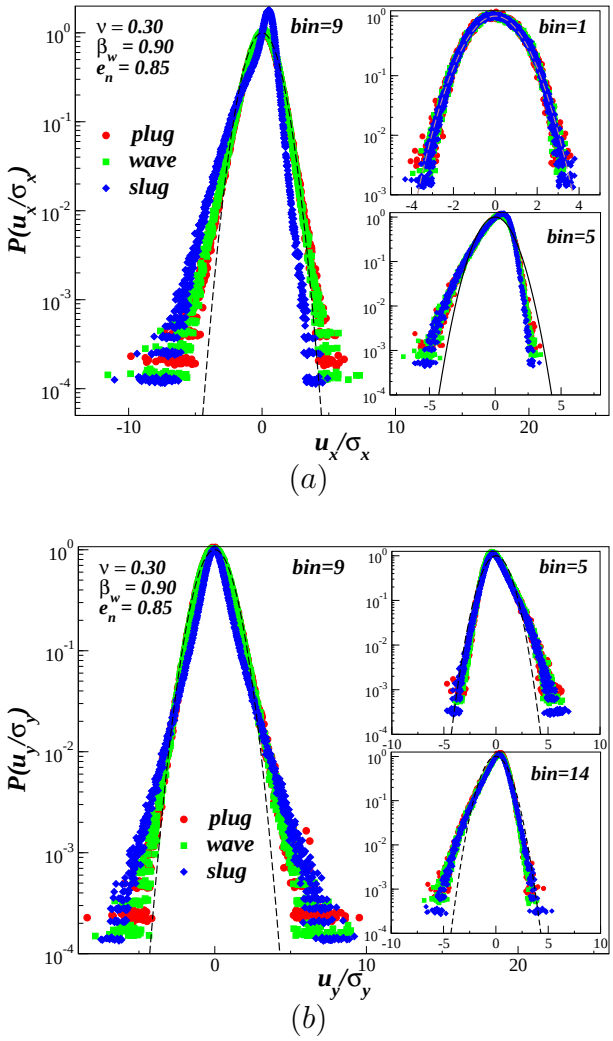

Figure 3.14: Effect of clusters (density waves) on (a) $P(u_x)$ and (b) $P(u_y)$ at $\nu = 0.30$, $e_n = 0.85$ for smooth walls ($\beta_w = 0.9$). The velocity distribution in region near wall, $bin = 1$, of both u_x (upper inset in (a)) and u_y (not shown) remain Gaussian. The distribution of u_x at other locations, $bin = 9$ in main panel and $bin = 5$ in upper inset of (a), are asymmetric. Similarly, the $P(u_y)$ distribution is asymmetric at all other locations but the asymmetry in $bin = 5$, upper inset in (b), and $bin = 14$, lower inset in (b), are in opposite direction.

becomes *asymmetric* with increasing dissipation, with an enhanced probability of negative velocities. At the center of the channel ($bin = 9$), the high velocity tails of the distribution function undergo a transition from a Gaussian to a non-Gaussian (with over-populated tails) with increasing collisional dissipation, as seen in the main panel of Fig. 3.16 (a). The analogue of Fig. 3.16 (a) for the fluctuating transverse velocity u_y is shown in Fig. 3.16 (b). The transition of $P(u_y)$ in the channel-centerline is very similar to that seen in $P(u_x)$. The distribution in $bin = 1$

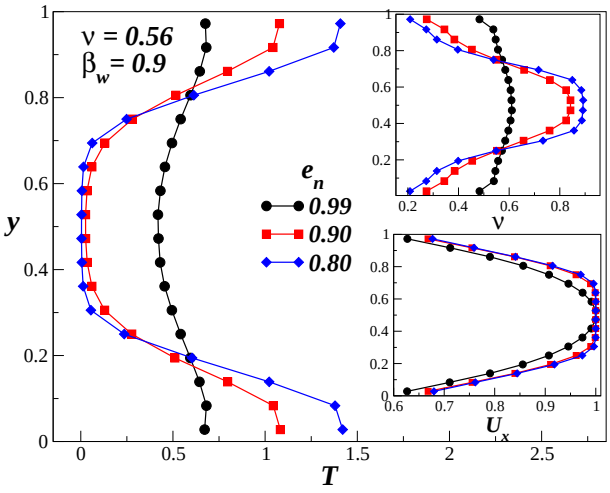

Figure 3.15: Effect of increasing the degree of dissipation on mean field quantites U_x, T and ν for $\nu = 0.56$ and $\beta_w = 0.9$.

remains Gaussian and is not shown here, instead we include the distribution in $bin = 14$ which is symmetrically located about the channel-centerline with respect to $bin = 5$, $P(u_y)$ distribution in these bins are mirror images. The $P(u_x)$ and $P(u_y)$ distributions for rough walls ($\beta_w = 0.1$) at $\nu = 0.56$ are shown in Fig. 3.17 (a) & (b), respectively. Surprisingly, the distributions at the centerline and the shear layer look similar for both smooth and rough walls. The robustness of results presented in Fig. 3.16 was tested by increasing the system size by eight folds *i.e.* at $N = 7200$, $W/d = 31$ and $L/W = 10.4$ as shown in Figs. 3.18 (a) and (b). The behaviour of velocity distributions with decreasing e_n is similar to that observed at $N = 900$ and $W/d = 31$. The open symbols in Figs. 3.18 (a) & (b) represent the distribution obtained by setting $N = 900$ and $W/d = 31$ at $e_n = 0.8$. There is a good agreement between the distributions at $N = 900$ and 7200. Snapshots of particle positions in steady state at $\nu = 0.56$, $e_n = 0.8$, $\beta_w = 0.9$ and $W/d = 31$ for $N = 900$ and $N = 7200$ particles are shown in Fig. 3.19.

With reference to dense flows in Fig. 3.16, the tails of $P(u_i)$ in the plug-region can be fitted via a power-law of the form $P(u_i) \sim u_i^{-\alpha_i}$, with a single exponent, $\alpha_x \sim 7$ and $\alpha_y \sim 5.5$, for a range of restitution coefficients, see the insets in Figs. 3.20 (a) and (b). The open symbols in Figs. 3.20 (a) are exponents of positive velocity tails for rough walls ($\beta_w = 0.1$) and the difference with the corresponding exponent for smooth walls is small, which indicates that the dynamics inside the plug region are unaffected by the wall roughness. The near-constancy of α_i for $e_n < 0.85$ could be due to the fact that the density within the plug saturates to the close-packing limit ($\nu_c \sim 0.9$) for $e_n < 0.85$ and, consequently, the other hydrodynamic fields also remain invariant there with a further decrease in e_n. This weak-variation of α_i on e_n could be tied to its variation with local average density.

We now turn to velocity distributions at very high densities (above the square-

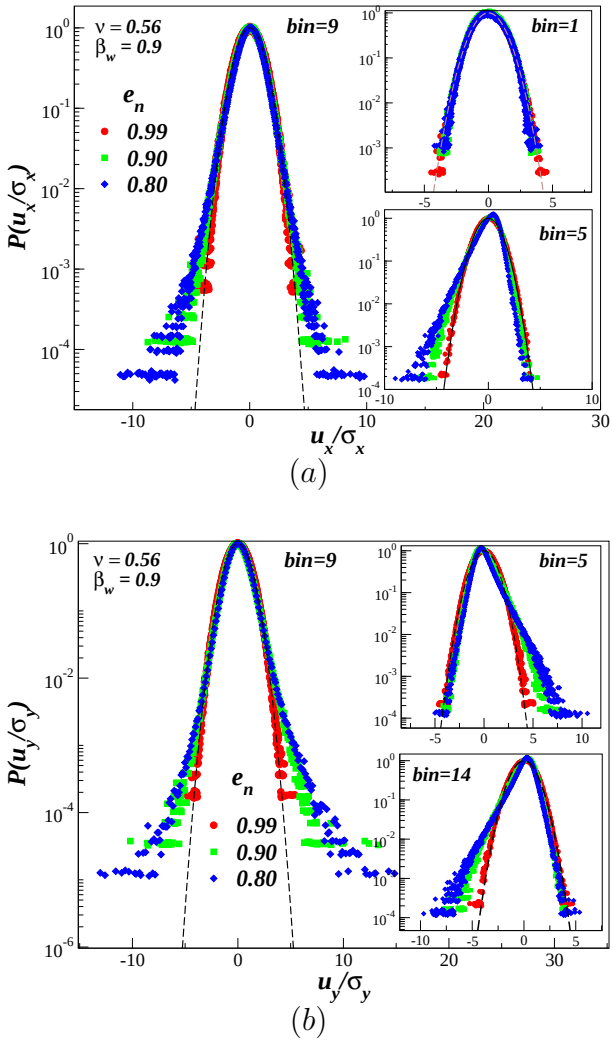

Figure 3.16: Effect of restitution coefficient, e_n, on (a) $P(u_x)$ and (b) $P(u_y)$ at $\nu = 0.56$ for smooth walls ($\beta_w = 0.9$). The tails of velocity distribution in $bin = 9$ in (a) and (b) make a transition from Gaussian to a power-law with increasing dissipation, the distribution in region near wall, $bin = 1$, of both u_x (upper inset in (a)) and u_y (not shown) remain Gaussian and the distribution of u_x $bin = 5$, lower inset in (a), shows asymmetry in the same direction on either sides of centre line but the asymmetry for u_y is in opposite direction as shown in $bin = 5$ and $bin = 14$ in (b).

packing density of $\nu = \pi/4$) *i.e.,* near quasi-static regime. So far we had used a square lattice for intialising the particle positions and the maximum average volume fraction that could be obtained was $\nu \sim 0.78$. To simulate very high density flows *i.e.,* $\nu > \pi/4$, a triangular lattice is used for initialising the particles positions and the maximum average volume fraction that could be obtained is $\nu \sim 0.9$. The mean field quantities at a volume fraction of $\nu = 0.85$ for smooth ($\beta_w = 0.9$) and rough walls($\beta_w = 0.1$) are shown in Fig. 3.21 (a) and Fig. 3.21 (b), respectively.

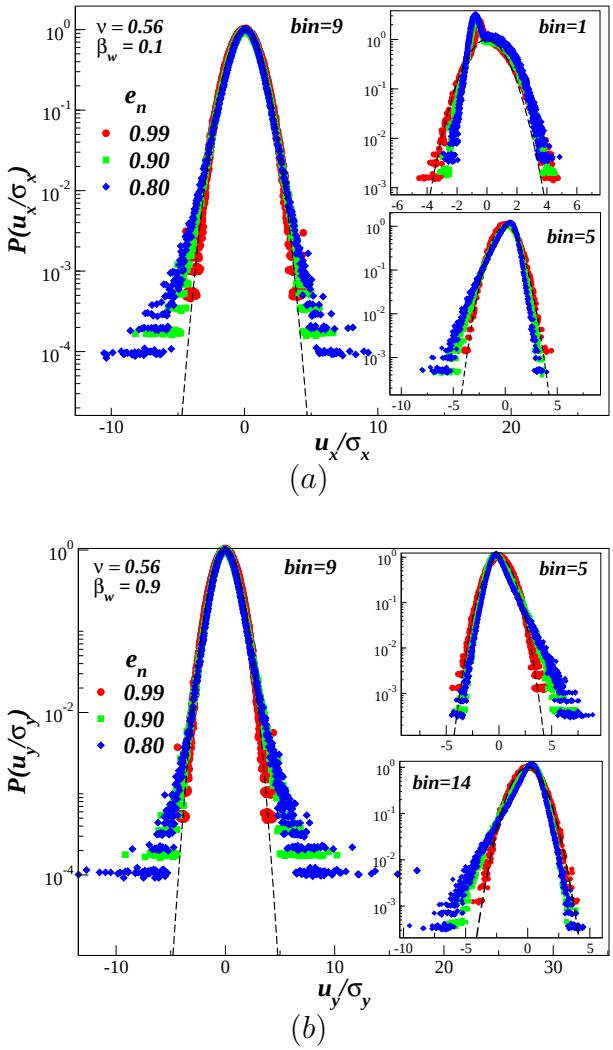

Figure 3.17: Effect of restitution coefficient, e_n, on (a) $P(u_x)$ and (b) $P(u_y)$ at $\nu = 0.56$ for rough walls ($\beta_w = 0.1$). The tails of velocity distribution in $bin = 9$ in (a) and (b) make a transition from Gaussian to a power-law with increasing dissipation, the u_x distribution (upper inset in (a)) has a asymmetric peak in the region near wall, $bin = 1$, and u_y (not shown) remain Gaussian and the distribution of u_x in $bin = 5$, lower inset in (a), shows asymmetry in the same direction on either sides of centre line but the asymmetry for u_y is in opposite direction as shown in $bin = 5$ and $bin = 14$ in (b).

We see that the shear layer outside the plug region is very thin, confined to only a couple of bin widths from the walls. The velocity distributions, $P(u_x)$ and $P(u_y)$, for smooth walls ($\beta_w = 0.9$) are shown in Fig. 3.22 and for rough walls ($\beta_w = 0.1$) in Fig. 3.23. The behaviour of velocity distributions with increasing dissipation is qualitatively similar to the observations made at $\nu = 0.56$ (Fig. 3.16 and Fig. 3.17). Since the shear layer is very thin we have considered the velocity distribution in $bin = 2$ and $bin = 17$ instead of $bin = 5$ and $bin = 14$.

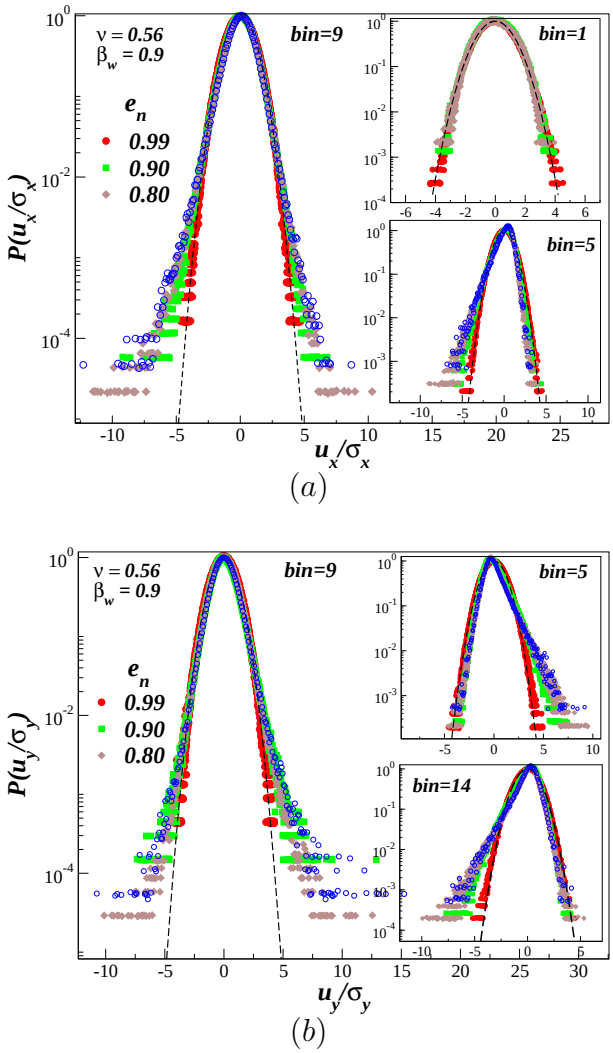

Figure 3.18: Effect of restitution coefficient, e_n, on (a) $P(u_x)$ and (b) $P(u_y)$ at $\nu = 0.56$, $N = 7200$ and $L/W = 10.4$ for smooth walls ($\beta_w = 0.9$). The tails of velocity distribution in $bin = 9$ in (a) and (b) make a transition from Gaussian to a power-law with increasing dissipation, the distribution in region near wall, $bin = 1$, of both u_x (upper inset in (a)) and u_y (not shown) remain Gaussian and the distribution of u_x in the region of high shear rate, lower inset in (a), shows asymmetry in the same direction on either sides of centre line but the asymmetry of $P(u_y)$ is in opposite direction as shown in $bin = 5$ and $bin = 14$ in (b). The open symbols represents the distributions obtained at $N = 900$ and $W/d = 31$ for $e_n = 0.8$.

We repeat the procedure that was followed for $\nu = 0.56$, to fit the tails of $P(u_i)$ using a power-law of the form $P(u_i) \sim u_i^{-\alpha_i}$. The exponent (α_i) initially decays with increasing dissipation, up to $e_n = 0.8$, and then remains nearly constant because the density in the plug region saturates to the close-packing density. The open symbols in Figs. 3.24 (a) are exponents of positive velocity tails for rough walls

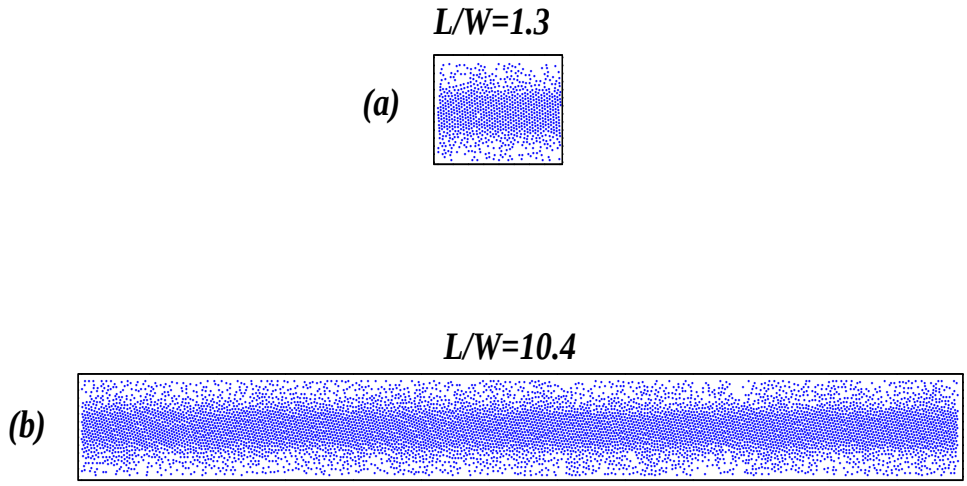

Figure 3.19: A snap shot of particle positions in the steady state for $\nu = 0.56$, $e_n = 0.8$, $\beta_w = 0.9$ and $W/d = 31$ when (a) $N = 900$ and (b) $N = 7200$ particles.

($\beta_w = 0.1$) and the difference between the corresponding exponent for smooth walls is small, which again indicates that dynamics inside the plug region are unaffected by the wall roughness. Further, a comparison of the exponents of the high velocity tails at $\nu = 0.85$ and $\nu = 0.56$ (Fig. 3.24 and Fig. 3.20, respectively) indicates a slower decay of α_i with e_n for $\nu = 0.85$.

A similar power-law behavior of the tails of velocity distribution functions (with $\alpha \sim 2.9 - 7.4$) has recently been observed in experiments of granular Poiseuille flow [63]; however, it is difficult to make a direct comparison since the experimental geometry is different (with a sieve at the bottom) and the experiments were carried out in the dense 'quasi-static' regime where it was noticed that particles were in contact for long-times with sliding and rolling interactions predominating. An appropriate collision model must include Coulomb friction and particle spin in order to make a direct comparision with the experimental results.

We finally present a set of surface plots in Fig. 3.25, delineating the exponent in the dense regime over a range of e_n for smooth walls. The symbols α_+ and α_- represent the exponents of the positive velocity tail and the negative velocity tails, respectively. The plots Fig. 3.25(a) & (b) represent the exponents of the $P(u_x)$ distribution, while the plots Fig. 3.25(a) & (b) represents the exponents of the $P(u_y)$ distribution.

3.2.3 Asymmetric tails

The tails of $P(u_x)$ and $P(u_y)$ distributions develop asymmetry with increasing degree of dissipation, which is evident from Fig. 3.16, Fig 3.17, Fig. 3.22 and Fig. 3.23. A simple way to characterise this asymmetry is to compute the skewness

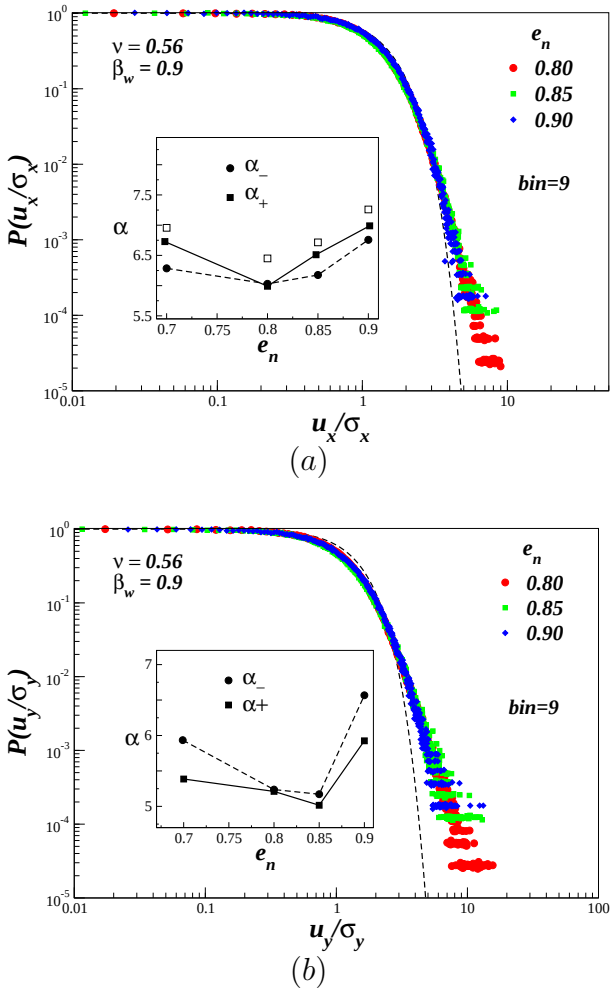

Figure 3.20: The main panel shows the positive velocity tails on a semi-log plot, while the inset shows exponents of the positive velocity tail (α_+) and negative velocity tail (α_-) of (a) $P(u_x)$ and (b) $P(u_y)$ distributions in $bin = 9$ at $\nu = 0.56$. The filled symbols are for smooth walls with a roughness of $\beta_w = 0.9$ and open symbols are for walls with a roughness of $\beta_w = 0.1$.

of the distribution which is given by the expression:

$$\gamma = \frac{\mu_3}{\mu_2^{3/2}}, \tag{3.2}$$

where $\mu_3 = \int_{-\infty}^{\infty}(x - \bar{x})^3 f(x)dx$ and $\mu_2 = \int_{-\infty}^{\infty}(x - \bar{x})^2 f(x)dx$ are the third and second moments about mean of the distribution, respectively. The binwise skewness of $P(u_x)$ and $P(u_y)$ distributions in Fig. 3.16 and Fig. 3.17 are shown in Fig. 3.26 (a) and (b), while the skewness of distributions in Fig. 3.22 and Fig. 3.23 are shown in Fig. 3.27(a) and (b), respectively. The continuous lines represent the skewness for smooth walls ($\beta_w = 0.9$) and the open symbols represents that

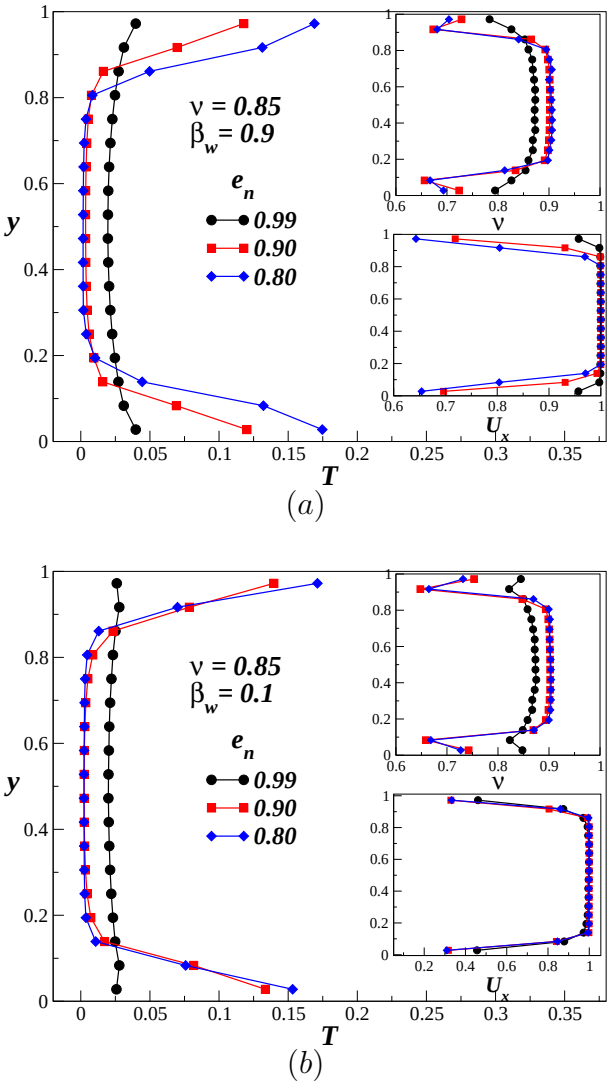

Figure 3.21: Effect of increasing the degree of dissipation of mean field quantites U_x, T and ν for $\nu = 0.85$ at (a) $\beta_w = 0.9$ and (b) $\beta_w = 0.1$.

for rough walls ($\beta_w = 0.1$). Let us focus on the skewness of the distribution at $\nu = 0.56$. In the quasi-elastic limit, the magnitude of skewness is close to zero in all the bins except for $P(u_x)$ distribution in the near wall region for rough walls. The magnitude of skewness of $P(u_x)$ and $P(u_y)$ distributions increases with increasing dissipation and varies non-monotonically along y-coordinate. It is maximum in the region where the shear rate, shown in the inset, is high and minimum in the plug region where the shear rate is negligible/small. The skewness of $P(u_x)$ distribution in Fig. 3.26 (a) remains negative in all the bins while the skewness for $P(u_y)$ distribution in Fig. 3.26 (b) changes sign due to the underlying asymmetry of u_y-velocity

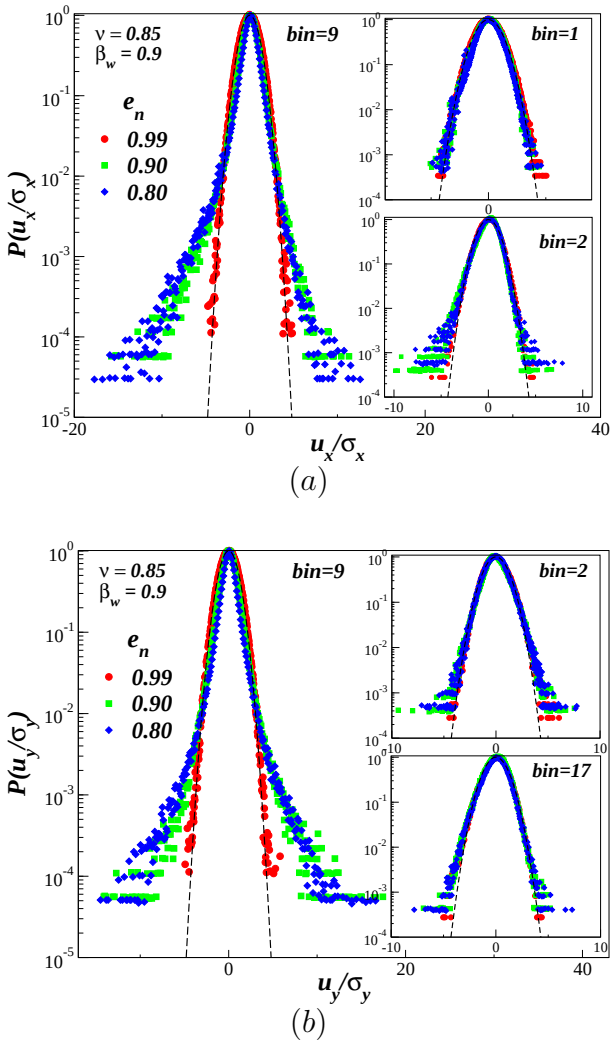

Figure 3.22: Effect of restitution coefficient, e_n, on (a) $P(u_x)$ and (b) $P(u_y)$ at $\nu = 0.85$ for smooth walls ($\beta_w = 0.9$). The tails of velocity distribution in $bin = 9$ in (a) and (b) make a transition from Gaussian to a power-law with increasing dissipation, the distribution in region near wall, $bin = 1$, of both u_x (upper inset in (a)) and u_y (not shown) remain Gaussian and the distribution of u_x $bin = 5$, lower inset in (a), shows asymmetry in the same direction on either sides of centre line but the asymmetry for u_y is in opposite direction as shown in $bin = 2$ and $bin = 17$ in (b).

Figure 3.28 gives an idea of the effect of volume fraction on the skewness of $P(u_x)$ distribution near the channel centerline ($bin = 9$) at $e_n = 0.8$ for smooth walls ($\beta_w = 0.9$). In the dilute limit, the inhomogenities along $x-$ direction have a dominant effect on the distribution, so the skewness is seen to increase with volume fraction upto $\nu \sim 0.3$. Beyond this value of volume fraction, the mean fields near the centerline of the channel become increasingly homogenous due to the formation of a plug and hence the skewness decreases. The skewness of distributions at

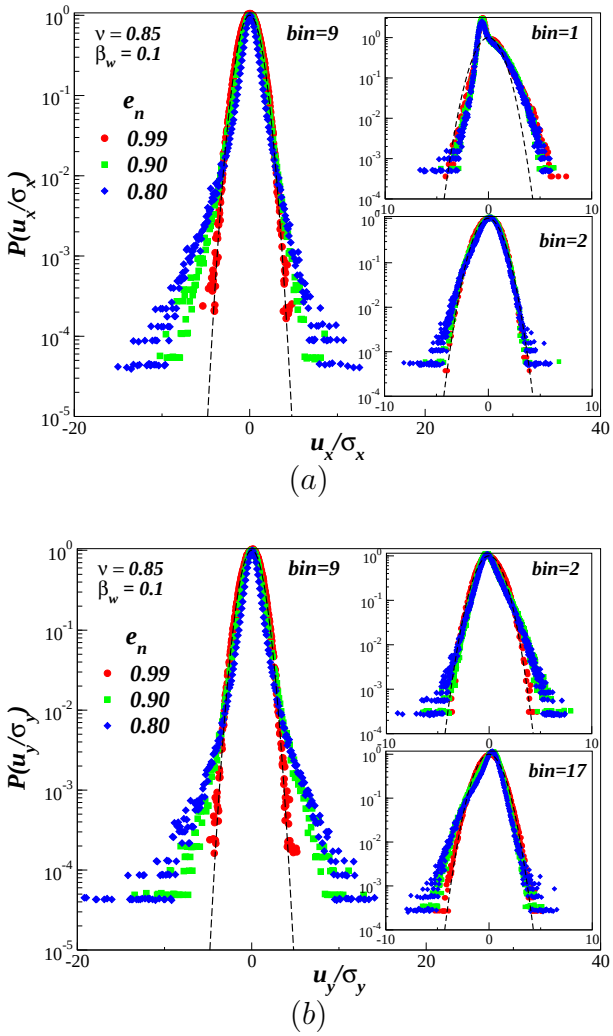

Figure 3.23: Effect of restitution coefficient, e_n, on (a) $P(u_x)$ and (b) $P(u_y)$ at $\nu = 0.85$ for rough walls ($\beta_w = 0.1$). The tails of velocity distribution in $bin = 9$ in (a) and (b) make a transition from Gaussian to a power-law with increasing dissipation, the u_x distribution (upper inset in (a)) has a asymmetric peak in the region near wall, $bin = 1$, and u_y (not shown) remain Gaussian and the distribution of u_x in $bin = 5$, lower inset in (a), shows asymmetry in the same direction on either sides of centre line but the asymmetry for u_y is in opposite direction as shown in $bin = 2$ and $bin = 17$ in (b).

$\nu = 0.85$ is shown in Fig. 3.27. In the inset of Fig. 3.28, the skewness is presented as a function of local (binwise) volume fraction. Since the system is inhomogeneous, the effect of local volume fraction on the skewness is more informative. It is seen that the skewness remains constant for $\nu_{bin} > 0.8$ (which corresponds to mean volume fraction of $\nu > 0.5$).

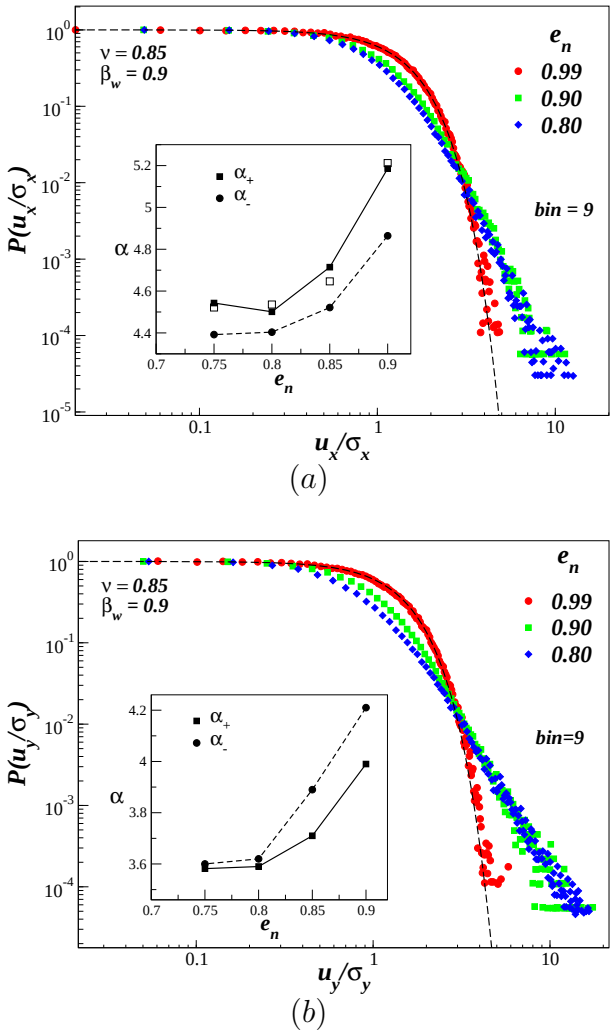

Figure 3.24: The main panel shows the positive velocity tails on a semi-log plot, while the inset shows exponents of the positive velocity tail (α_+) and negative velocity tail (α_-) of (a) $P(u_x)$ and (b) $P(u_y)$ distributions in $bin = 9$ at $\nu = 0.85$. The filled symbols represent smooth walls ($\beta_w = 0.9$) and open symbols represents rough walls ($\beta_w = 0.1$).

3.3 Density and velocity correlations

In dense flows the tails of velocity distributions make a transition from a Gaussian to a power-law with decreasing coefficient of restitution (e_n). It was observed that even the low velocities deviate from Gaussian distribution at $\nu = 0.85$ and $e_n = 0.8$. It has been shown by various authors [10, 11, 64, 73, 74] that inelastic collisions lead to velocity correlations that are responsible for non-Gaussian velocity distribution. To pinpoint the role of e_n on distribution functions, we study its effect on the pair correlation function and the spatial velocity correlations.

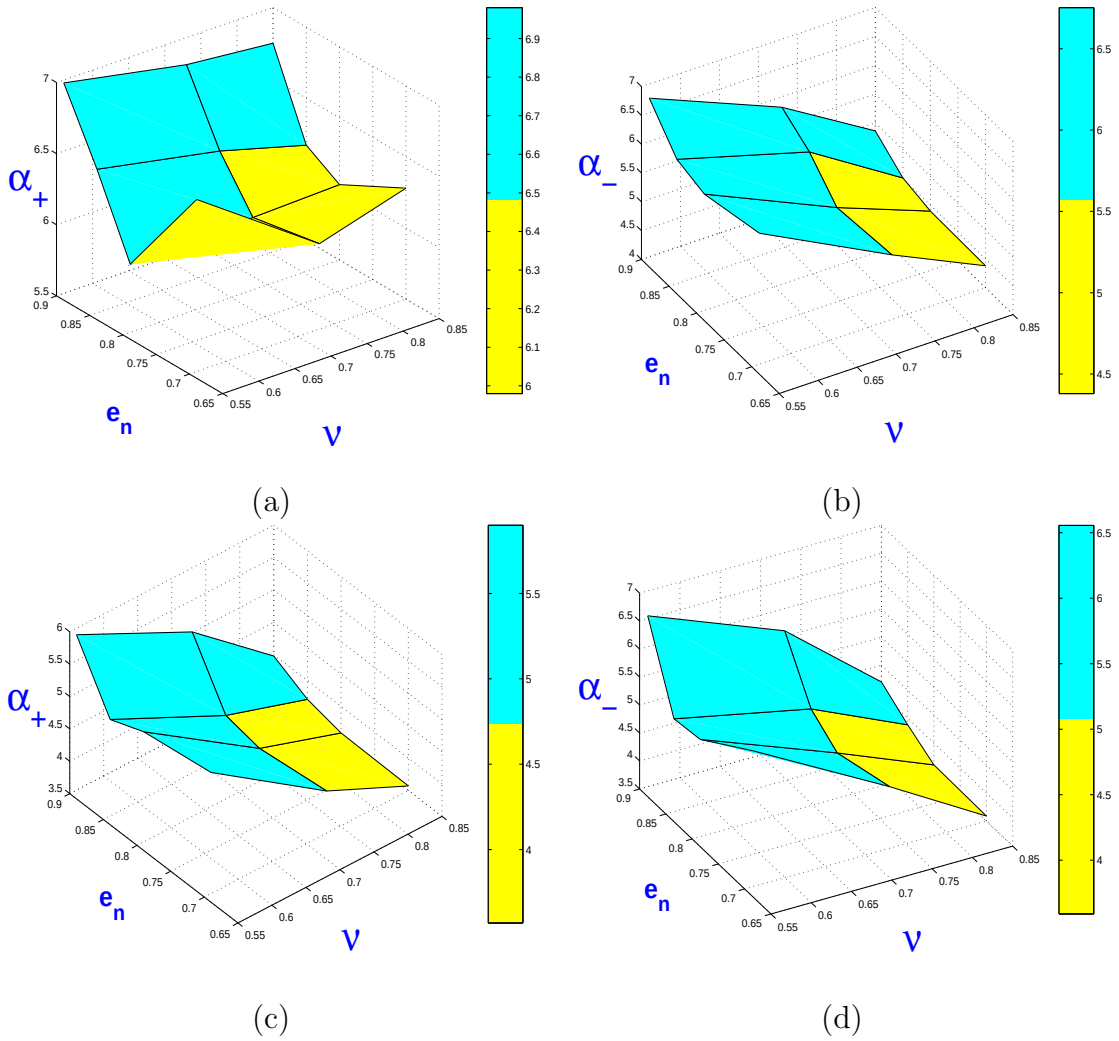

Figure 3.25: Surface plots of the exponents in the dense limit ($\nu > 0.5$) over a range of e_n. The plots (a) and (b) delineate the exponents of the tails of $P(u_x)$ distribution, while the plots (c) and (d) correspond to $P(u_y)$ distribution. The symbols α_+ and α_- represent the exponents of the positive and negative velocity tails, respectively.

Pair correlation function

The pair correlation function ($g(r)$) is defined as the probability of finding a neighbour at a distance r from a particle at the origin. Thus $g(r)$ provides a measure of local spatial ordering of the particles. The expression for $g(r)$ is given below :

$$g(r) = \frac{2A}{N^2} \left\langle \sum_{i=1}^{N} \sum_{j>i}^{N} \delta(r - r_{ij}) \right\rangle \tag{3.3}$$

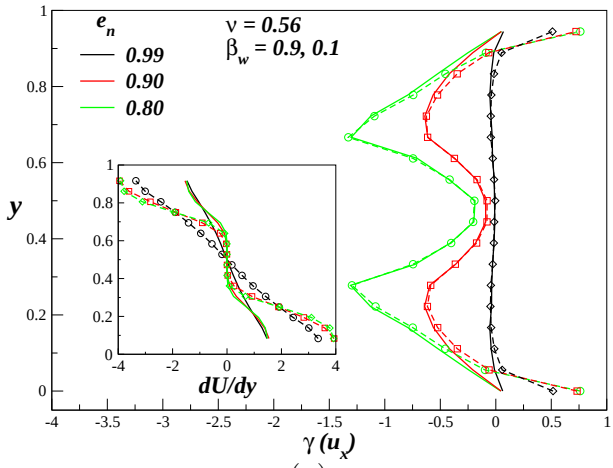

(a)

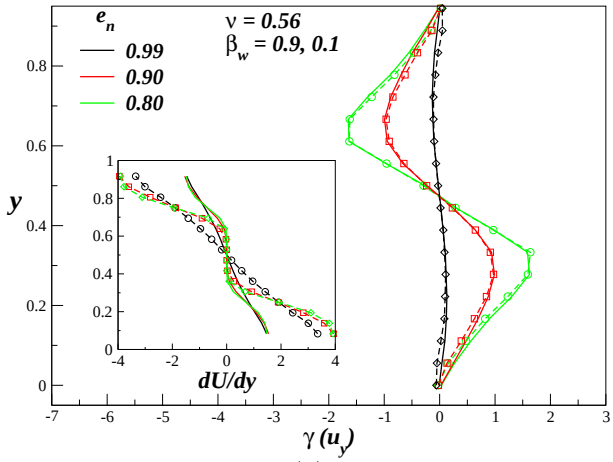

(b)

Figure 3.26: The main panel shows the skewness of (a) $P(u_x)$ and (b) $P(u_y)$ distributions in various bins across the channel width, while insets shows the shear rate at $\nu = 0.56$. The open symbols represent skewness for rough walls ($\beta_w = 0.1$) and continuous lines represents skewness for smooth walls ($\beta_w = 0.9$).

where A is the area, N is the number of particles and the angular brackets indicates an average over time. Since our interest is in binwise computation of pair correlation function, A is area of the bin and N is number of particles in a bin.

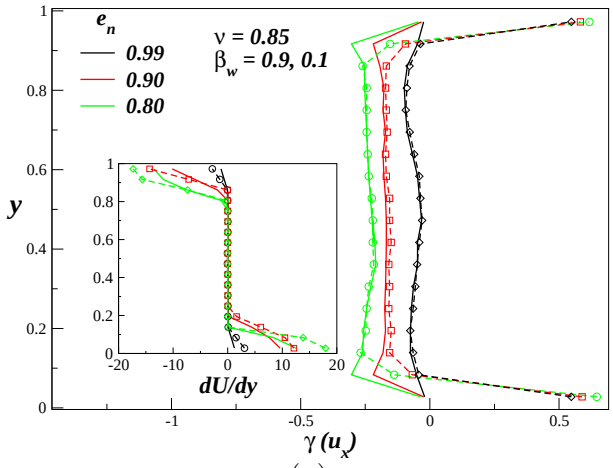

(a)

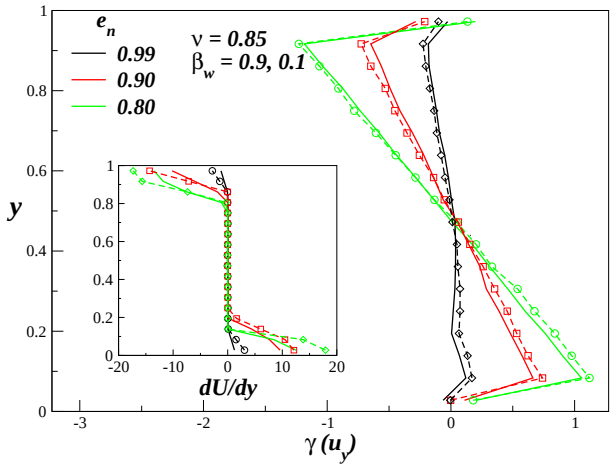

(b)

Figure 3.27: The main panel shows the skewness of (a) $P(u_x)$ and (b) $P(u_y)$ distributions in various bins across the channel width, while insets shows the shear rate at $\nu = 0.85$. The open symbols represent skewness for rough walls ($\beta_w = 0.1$) and continuous lines represents skewness for smooth walls ($\beta_w = 0.9$).

Spatial velocity correlation function

The four velocity correlation functions are defined as :

$$C_{\alpha\beta}(r) = \frac{\left\langle \sum_{i=1}^{N} \sum_{j \geq i}^{N} u_\alpha^i u_\beta^j \delta(r - r_{ij}) \right\rangle}{\left\langle \sum_{i=j}^{N} u_\alpha^i u_\beta^j \right\rangle}, \tag{3.4}$$

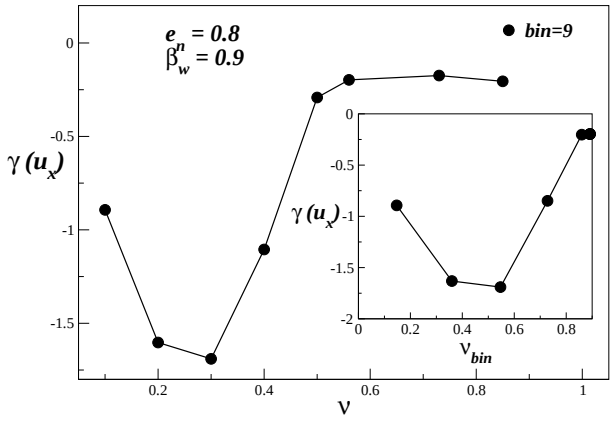

Figure 3.28: The effect of volume fraction on the skewness of the $P(u_x)$ distribution near the centerline of the channel ($bin = 9$) for $e_n = 0.8$ and $\beta_w = 0.9$. In the inset, skewness is plotted as a function of the local (binwise) volume fraction.

where the subscripts α, β denote coordinate directions, superscripts i, j denote the particle number and the angular brackets indicate an average over time. When particle velocities are random the correlations are zero, so a non-zero value indicates correlated velocities.

Velocity auto-correlation function

$$C_i(\delta t) = \frac{\langle u_i(t) u_i(t+\delta t) \rangle}{\langle u_i(t) u_i(t) \rangle} \tag{3.5}$$

where the subscript i denotes the coordinate direction and the angular brackets represent an average over time.

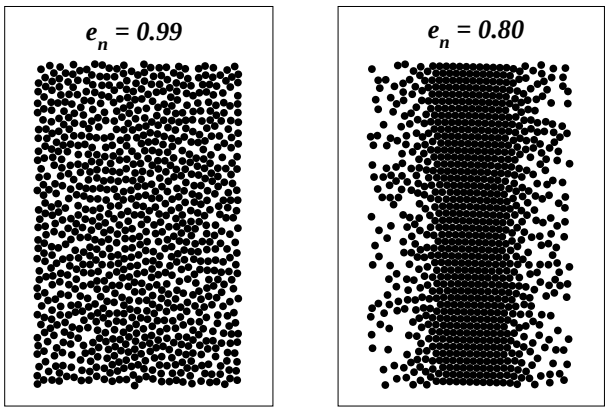

Figure 3.29: A snapshot of instantaneous particle positions in the steady state for $\nu = 0.56$ and $\beta_w = 0.9$ at (a) $e_n = 0.99$ and (b) $e_n = 0.80$.

We begin our study by examining the effect of coefficient of restitution on spatial correlations at a volume fraction of $\nu = 0.56$ for smooth walls ($\beta_w = 0.9$). The

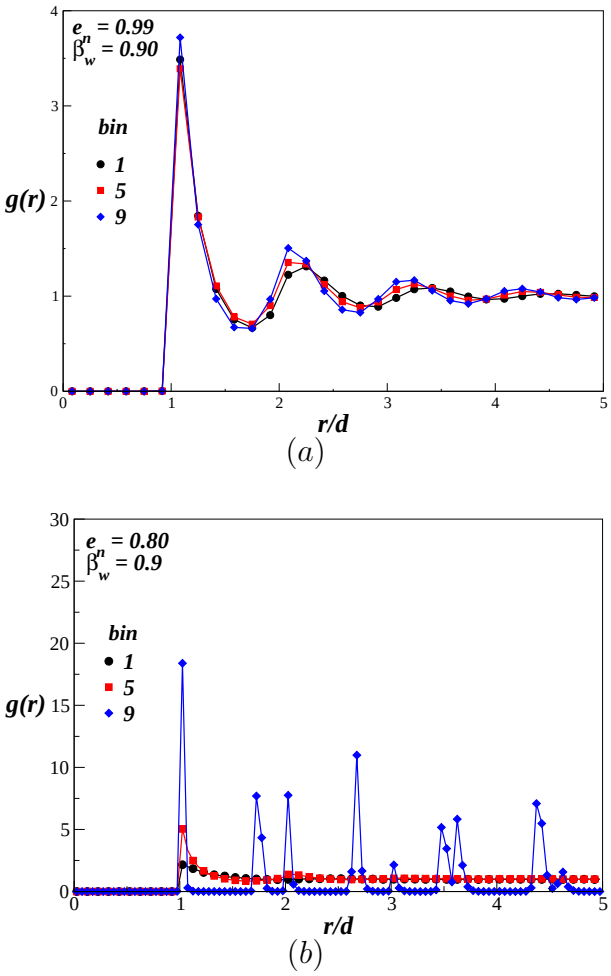

Figure 3.30: The Pair correlation function, $g(r)$, in different bins at a density of $\nu = 0.56$ and at a dissipation value of (a) $e_n = 0.99$ and (b) $e_n = 0.80$ are shown.

snapshots of particle positions at $e_n = 0.99$ and $e_n = 0.8$ are shown in Fig. 3.29 (a) & (b), respectively. An increase in dissipation gives rise to a plug at the channel centerline and the crystal like structure of the plug at $e_n = 0.8$ is apparent from Fig. 3.29 (b). For a better understanding of the local structure of the fluid, we turn our attention to pair correlation function. In the quasielastic limit ($e_n = 0.99$), the pair correlation function, Fig. 3.30 (a), shows a liquid-like structure in all bins. The signatures of plug-formation with increasing dissipation show up in the pair correlation function (Fig. 3.30 (b)); dominant peaks at regular intervals indicate a crystal-like structure at the centerline ($bin = 9$) at $e_n = 0.8$. Outside the plug region, ($bin = 1, 5$ in Fig. 3.30 (b)), $g(r)$ shows a gaseous structure.

We now move on to velocity correlations at $\nu = 0.56$ that are shown in Fig. 3.31, Fig. 3.32 and Fig. 3.33. The streamwise velocity correlation C_{xx} in the quasi-elastic limit, Fig. 3.31 (a), is close to zero in all the bins. With increasing density

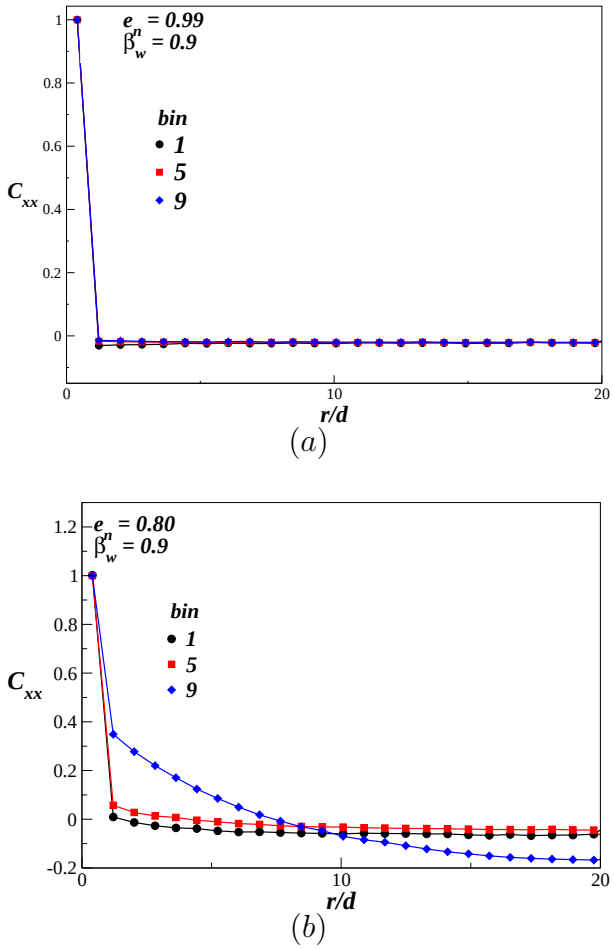

Figure 3.31: The streamwise velocity correlation function C_{xx} at a density of $\nu = 0.56$ and at a dissipation value of (a) $e_n = 0.99$ and (b) $e_n = 0.80$ are shown.

correlation in $bin = 9$, the velocity correlation C_{xx} also becomes strong as shown in Fig. 3.31(b). It is interesting to note that the velocity correlation is negative beyond a certain correlation length, $r/d \sim 10$, which could be an indicator of circulatory-type motion [66] for the fluctuating velocity field. At $e_n = 0.8$, the C_{xx} correlation outside the plug region is weak/absent, (see Fig. 3.31 b). The behaviour of spanwise velocity correlation C_{yy} with increasing dissipation follow that of C_{xx}. Similar observations were made with reference to cross velocity correlation function C_{xy}. The C_{xy} correlation in different bins at $e_n = 0.8$ is shown in Fig. 3.33 (a). Once again the correlation in the plug region ($bin = 9$) is strong compared to shear ($bin = 5$) or wall ($bin = 1$) region. If we now focus on $bin = 9$ at the channel-centreline, we see that C_{xy} correlation is enhanced with increasing dissipation as shown in Fig. 3.33 (b). From the above observations it is apparent that enhanced density and velocity correlations around the channel-centerline are responsible for the emergence of non-Gaussian tails with increasing dissipation (Fig. 3.16).

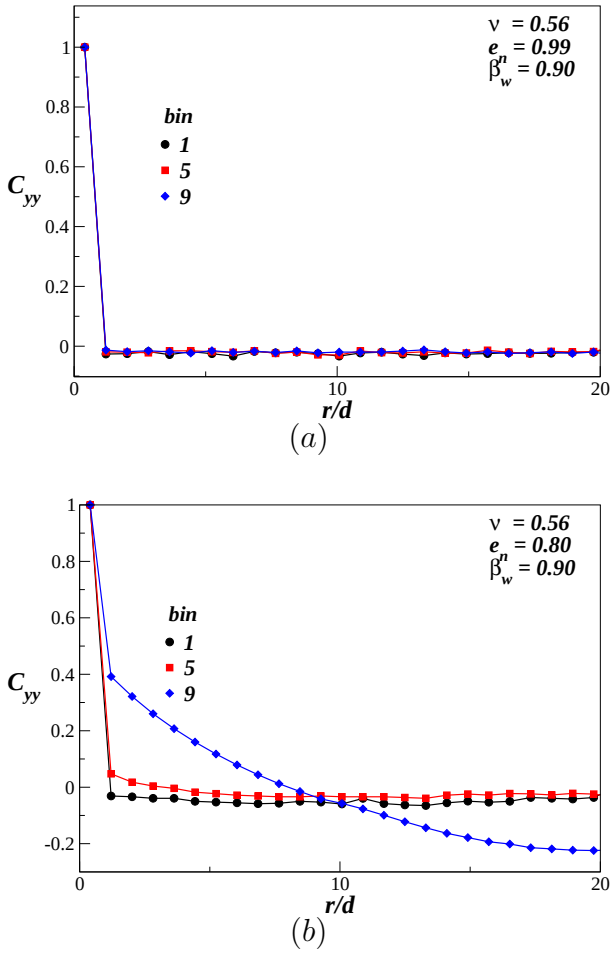

Figure 3.32: The spanwise velocity correlation function C_{yy} at a density of $\nu = 0.56$ and at a dissipation value of (a) $e_n = 0.99$ and (b) $e_n = 0.80$ are shown.

It was observed that C_{xx} correlation near the centerline of the channel ($bin = 9$) becomes negative beyond a certain correlation length at $e_n = 0.8$. To support the existence of circulatory-type of motion, snapshots of the fluctuating velocity vectors of the particles in steady state are shown in Fig. 3.34. For the clarity of understanding, the particles in two bins ($bin = 9, 10$) are shown. From these snapshots, it is clear that velocity vectors of particles reverse after a certain length. To give an idea about the nature of motion in the near-wall region, snapshots of the fluctuating velocity vectors and the instantaneous positions of the particles in $bin = 18, 17$ are displayed in Fig, 3.35.

The pair correlation function and velocity correlations for rough walls ($\beta_w = 0.1$) at $\nu = 0.56$ display the same qualitative behaviour as smooth walls, so only the pair correlation function at $e_n = 0.80$ and the corresponding C_{xx} velocity correlation functions are shown in Fig. 3.36.

Lastly, we present another set of results on correlation functions for very dense

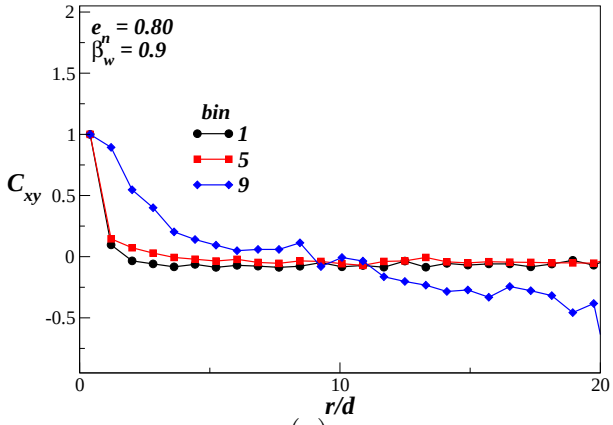

(a)

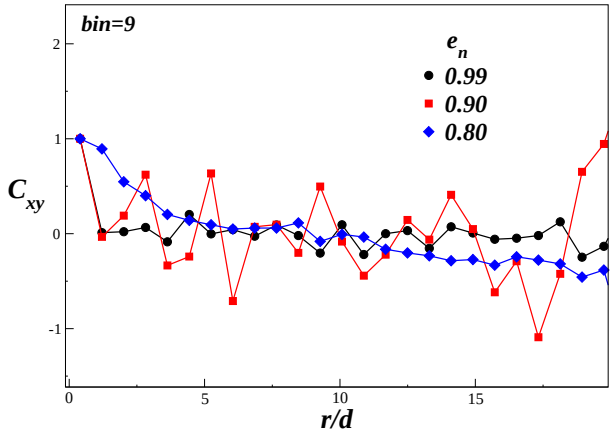

(b)

Figure 3.33: Velocity cross correlation function C_{xy} in different bins for $\nu = 0.56$, $e_n = 0.80$ and $\beta_w = 0.9$ is displayed in (a), while C_{xy} near the centre of channel, $bin = 9$ at different values of dissipation is displayed in (b).

flows, correponding to a volume fraction of $\nu = 0.85$. It may be recalled that for this case the shear layer is very thin and confined to a small region near the walls (Fig. 3.21). So we consider only $bin = 2, 9$ for studying the correlation functions. The pair correlation function at $e_n = 0.80$ and $e_n = 0.99$ is shown in Fig. 3.37 (a) & (b), respectively. A crystal-like structure is seen at the center of channel ($bin = 9$) even in the quasi-elastic limit, Fig 3.37 (a), whereas a liquid like structure exists in the shear layer $bin = 2$. With an increase in the degree of dissipation, the density correlations in the plug region are enhanced but the structure in the shear layer remains to be in liquid form, Fig. 3.37 (b).

For $\nu = 0.85$, the velocity correlations C_{xx} and C_{yy} are nearly absent or close to zero in the quasi-elastic limit as shown in Fig. 3.38 (a) and Fig. 3.39 (a), respectively. It is interesting to notice that C_{xx} (and C_{yy}) is zero near the channel centerline ($bin = 9$) in Fig 3.38 (a) (and Fig 3.39 (a)) even though the pair correla-

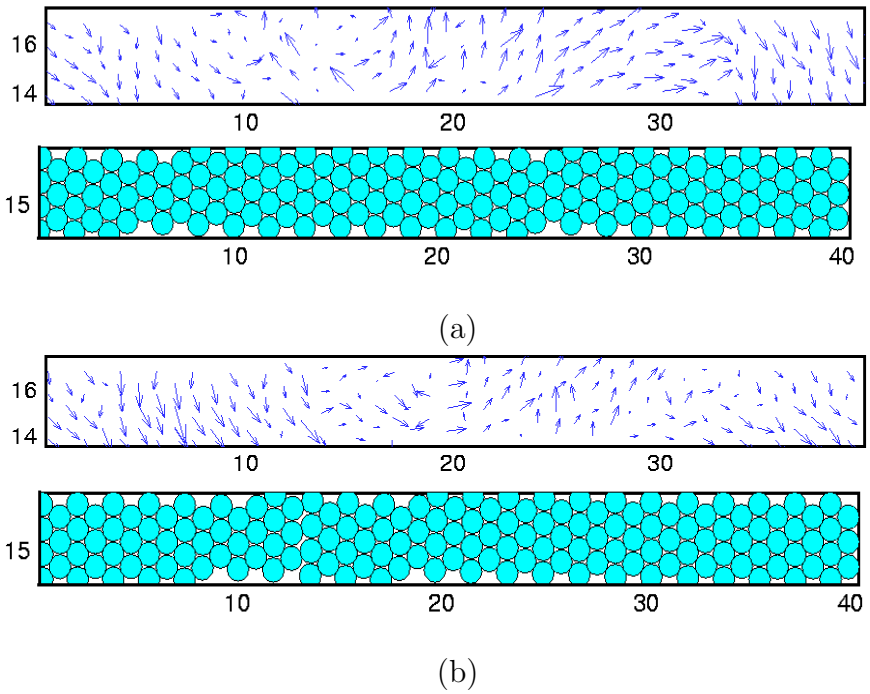

Figure 3.34: Snapshots of the fluctuating velocity vectors of the particles near the centerline of the channel at two different times (a) $t = 330$ and (b) $t = 340$ in the steady state are shown for $\nu = 0.56, e_n = 0.8$ and $\beta_w = 0.9$. The particles in both $bin = 9, 10$ are shown for clarity. The numbers in the plots represent the coordinate values.

tion function $g(r)$ in Fig. 3.37 (a) shows a crystal-like structure. At $e_n = 0.80$, the C_{xx} and C_{yy} correlations in $bin = 2, 9$ are shown in Fig 3.38 (b) and Fig. 3.39 (b), respectively. The enhanced correlations in Fig. 3.38 (b) and Fig. 3.39 (b) once again support the fact that inelastic collisions induce velocity correlations. In Fig. 3.41, the fluctuating velocity vectors of the particles in $bin = 9, 10$ are shown at two different times, after the system has attained a steady state. The reversal of velocity vectors after a certain distance supports the negative velocity correlations seen in Fig. 3.38 and Fig. 3.39.

For further information on the correlated motion of the particles in time, we turn our attention to velocity autocorrelation functions, Eq. 3.5. Few results for the streamwise velocity autocorrelation function C_x at high densities ($\nu = 0.56$ and 0.85) and $e_n = 0.99, 0.80$ are presented in Fig. 3.42 and Fig. 3.43. We notice that the velocity correlations decay to zero almost immediately in both the shear layer and plug region.

Several interesting findings emerge from our study of correlation functions. Firstly, our results confirm and support the previous findings that inelastic collisions indeed leads to enhanced velocity correlations [10, 11, 64, 73, 74], which in turn explains the deviation of the tails of velocity distribution from a Gaussian.

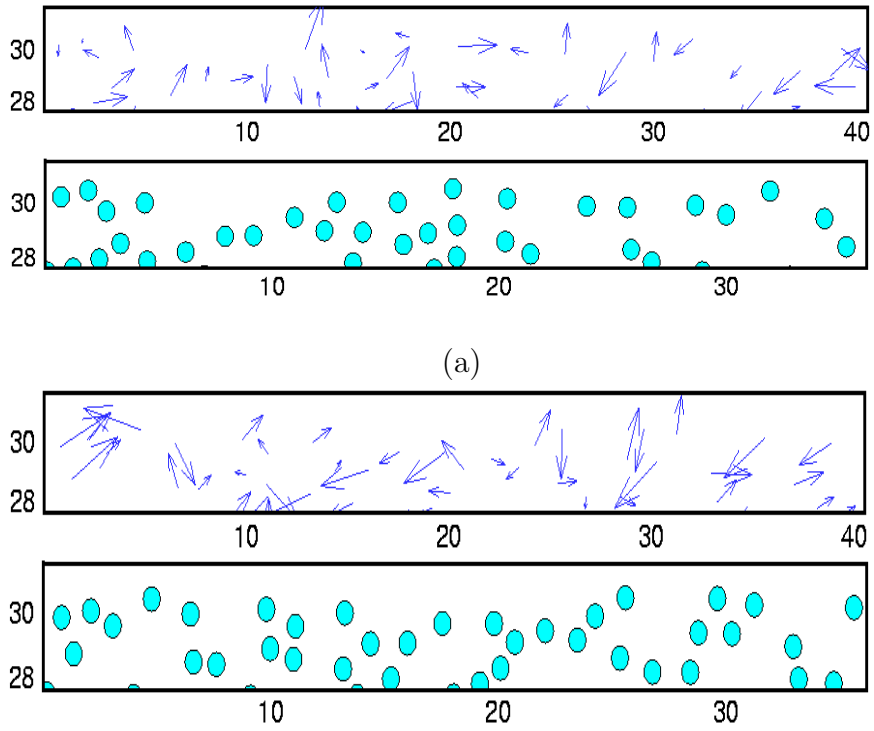

(a)

(b)

Figure 3.35: Snapshots of the fluctuating velocity vectors of particles in the near-wall region at two different times (a) $t = 330$ and (b) $t = 340$ in the steady state are shown for $\nu = 0.56, e_n = 0.8$ and $\beta_w = 0.9$. The particles in $bin = 18, 17$ are shown for clarity.

Secondly, our study reveals that though density correlations play a significant role in enhancing the velocity correlations when the collision are inelastic, however, they do not induce velocity correlations when the collisions are quasi-elastic, which is evident in Figs. 3.31 (a), 3.33 (a) and 3.38 (a).

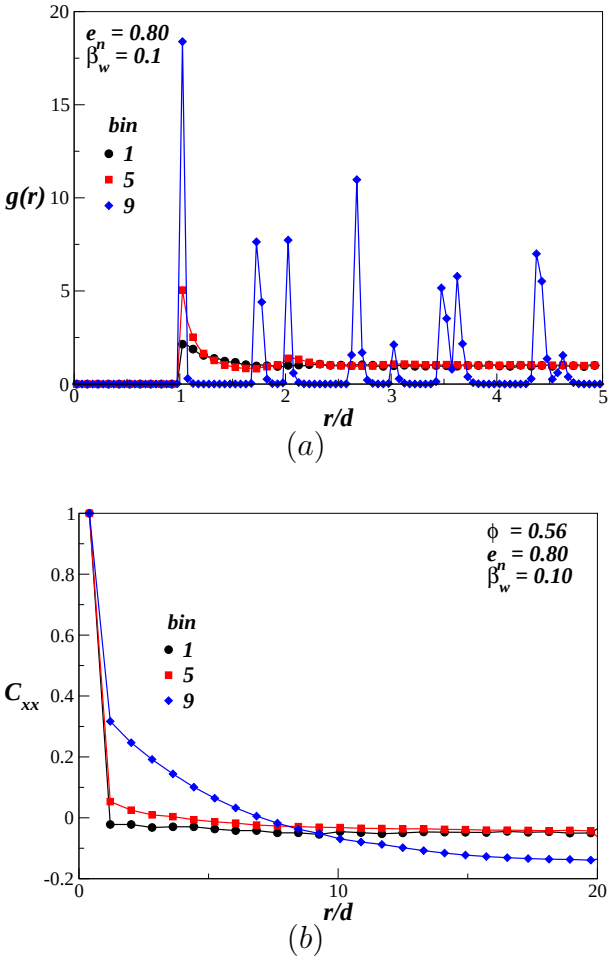

Figure 3.36: (a) The Pair correlation function, $g(r)$, and (b) streamwise velocity correlation function C_{xx} in different bins at a density of $\nu = 0.56$ and a coefficient of restitution of $e_n = 0.80$.

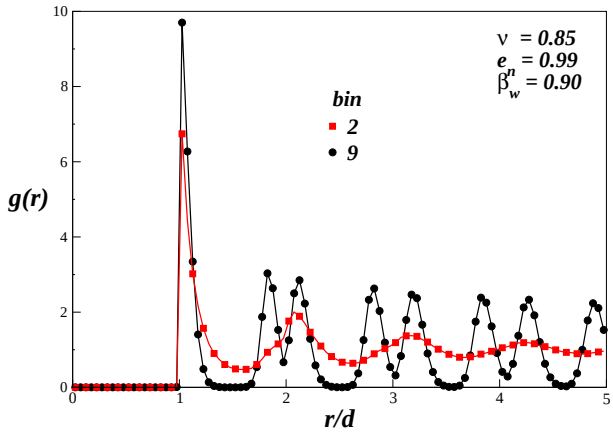

Figure 3.37: Pair correlation function, $g(r)$, of a very dense flow ($\nu = 0.85$) at (a) $e_n = 0.99$ and (b) $e_n = 0.80$. Since the shear layer is thin, only $bin = 2, 9$ are considered.

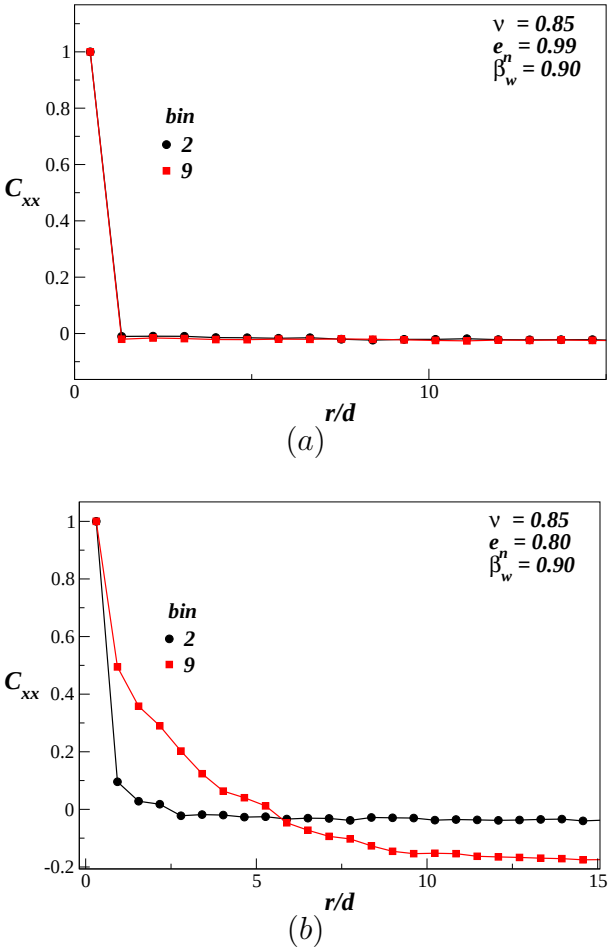

Figure 3.38: Streamwise velocity correlation function, C_{xx}, of a very dense flow ($\nu = 0.85$) at (a) $e_n = 0.99$ and (b)$e_n = 0.80$. Since the shear layer is thin, C_{xx} only in $bin = 2, 9$ are shown.

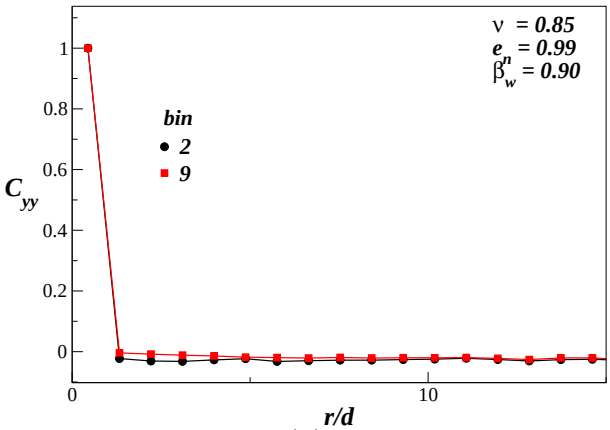

(a)

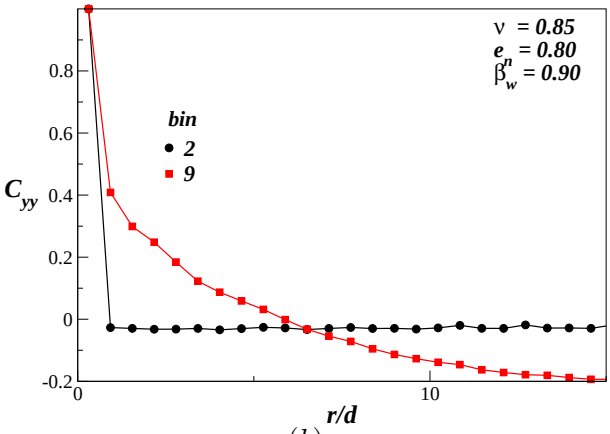

(b)

Figure 3.39: Spanwise velocity correlation function, C_{yy}, of a very dense flow ($\nu = 0.85$) at (a) $e_n = 0.99$ and (b)$e_n = 0.80$. Since the shear layer is thin, C_{yy} only in $bin = 2, 9$ are shown.

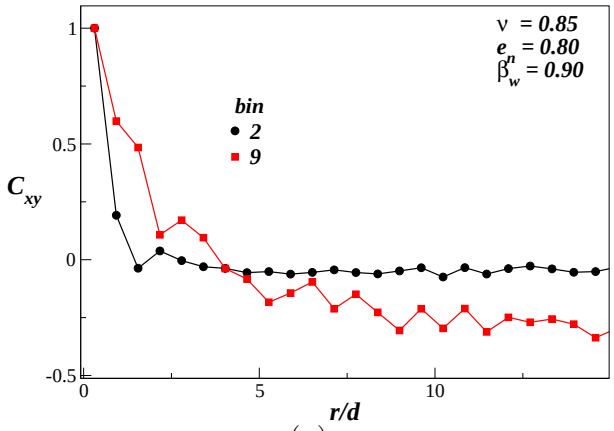

(a)

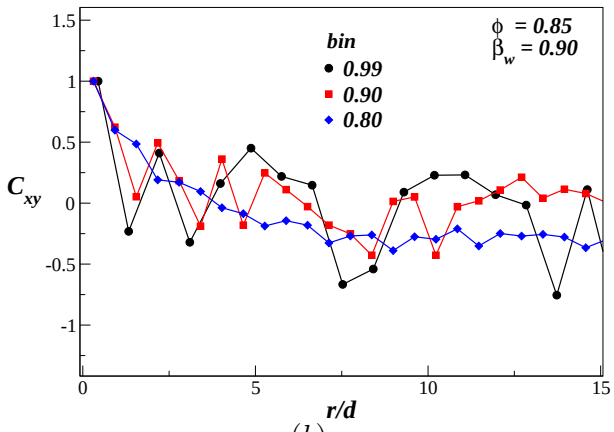

(b)

Figure 3.40: Velocity cross correlation function C_{xy} in different bins at $\nu = 0.85$, $e_n = 0.80$ and $\beta_w = 0.9$ is shown in (a), while C_{xy} near the centre of channel, $bin = 9$ at different values of dissipation is shown in (b).

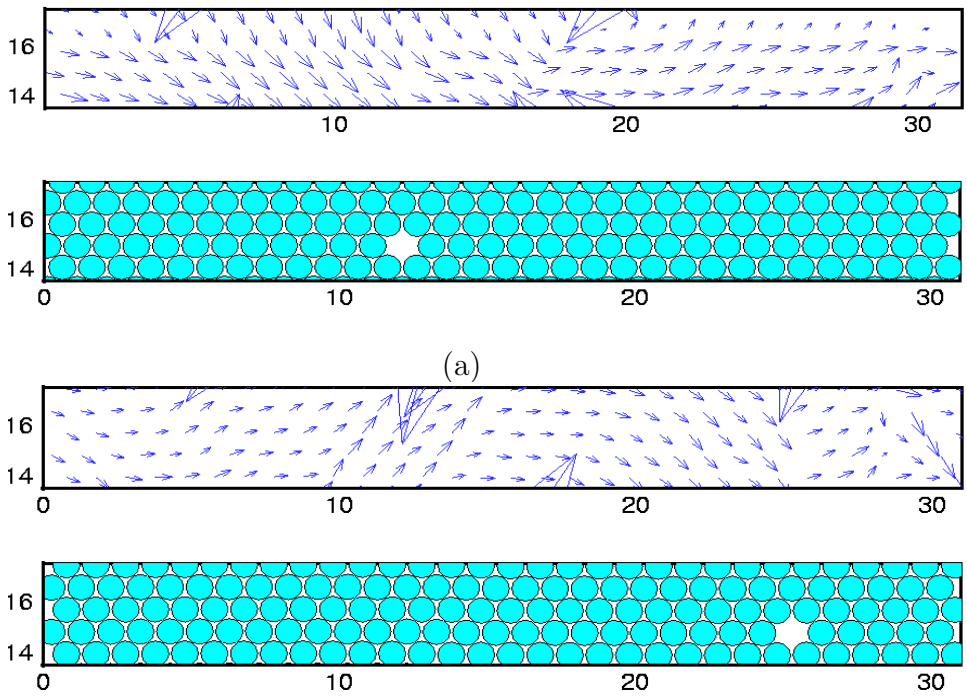

Figure 3.41: Snapshots of the fluctuating velocity vectors of particles along with their positions at two different times (a) t=130 and (b) t=135. The value of the parameters are $\nu = 0.85, e_n = 0.8$ and $\beta_w = 0.9$. For clarity of understanding, the particles in $bin = 9, 10$ are displayed.

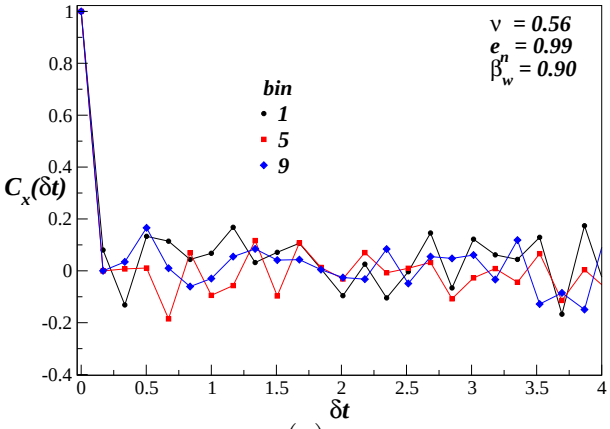

(a)

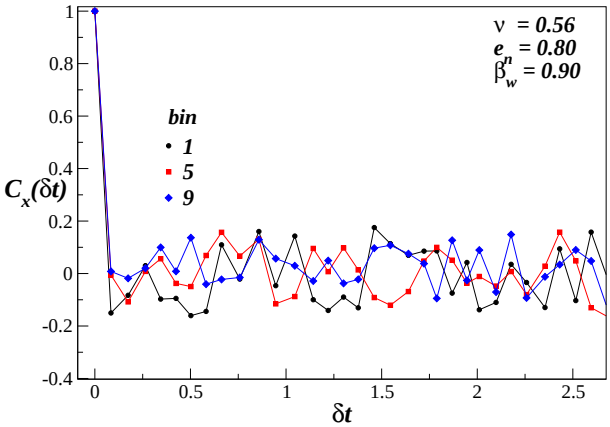

(b)

Figure 3.42: Streamwise velocity autocorrelation function C_x in different bins at $\nu = 0.56$ and $\beta_w = 0.9$ for (a) $e_n = 0.99$ and (b) $e_n = 0.80$.

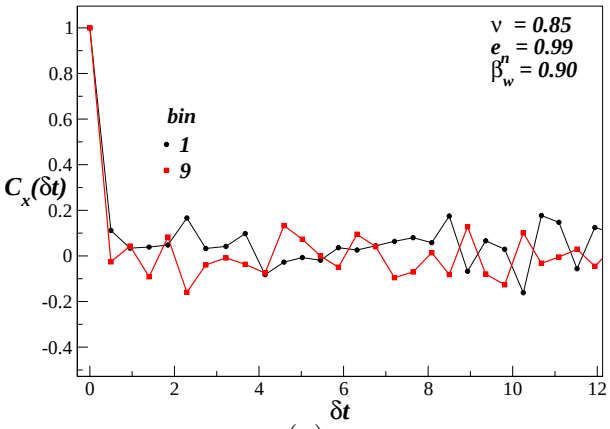

(a)

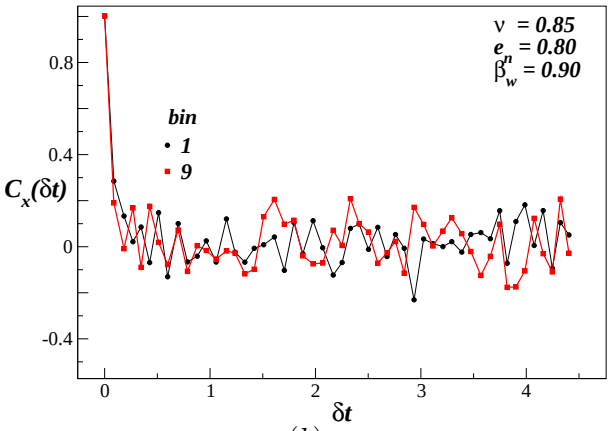

(b)

Figure 3.43: Streamwise velocity autocorrelation function C_x in different bins at $\nu = 0.85$ and $\beta_w = 0.9$ for (a) $e_n = 0.99$ and (b) $e_n = 0.80$.

CHAPTER 4

RHEOLOGICAL QUANTITIES, SLIP VELOCITY AND TEMPERATURE JUMP

4.1 Rhelogical quantities

The focus in the present thesis is on rapid flow regime where the particle collisions are assumed to be binary and instantaneous. This picture of granular flow has many similarities with the thermal motion of molecules and has motivated in defining temperature and stresses for granular flow in a way similar to molecules. The energy associated with the fluctuating motion of granular particles is defined as the granular temperature, though it is not same as the thermodynamic temperature, and the momentum transfer due to their motion and collisions is used to define stresses. However, the behaviour of granular particles deviate from molecules due to inelastic collisions and macroscopic size of particles [30].

One of the major challenges has been the continuum modelling of granular flow. The first attempt to derive constitutive equations for rapid granular flows from microscopic considerations, based on heuristic arguments was made by Bagnold [6]. He showed that at reasonably large concentrations and shear rates, the stresses generated depend on the square of the imposed shear rate. Following Ogawa's idea [69], Haff [36] proposed a balance equation for the fluctuation energy using heuristic arguments, drawing an analogy with thermal motion in gases. Later, the constitutive equations were developed based on the formalism of kinetic theory [41, 43, 55, 83, 85]. Savage & Jeffrey [83] have developed constitutive relations for smooth, hard and inelastic spheres in a simple shear. They assumed Maxwellian velocity distribution function and Carnahan & Starling [20] hard sphere pair distribution function. Their results showed a good agreement with the experimental results of Bagnold [6]. Jenkins & Savage [43] solved the energy balance equation for the granular temperature assuming Maxwellian distribution as the single particle velocity distribution and using an approximated linear anisotropic pair distribution function, valid only in the quasi-elastic limit. Further, Lun *et al.,* [55] followed a more rational approach of expanding the pair correlation function in Taylor series form and assuming the Maxwellian distribution with a first-order correction as the single particle distribution function. For the first time they accounted both the kinetic and collisional contributions to the stress tensor. Constitutive equations that take into account both frictional and collisional transport of momentum were proposed by Savage [82] and Johnson & Jackson [44]. Jenkins & Richman [41] followed an extension of Grad's method of moments [34] to find the approximate velocity

distribution function for deriving the constitutive relations of a dense gas of identical, rough, inelastic and circular disks. Their theory was found to be valid only for small values of particle surface friction and nearly elastic collisions. Based on the observation that in the double limit of $\epsilon \to 0$ and $Kn \to 0$, where ϵ $(= 1-e_n^2)$ is the degree of inelasticity and Kn is the Knudsen number, the collisionally relaxed state (under homogeneous and isochoric deformation) corresponds to a Maxwellian, Sela & Goldhirsch [85] proposed a modified Chapman-Enskog expansion in which both ϵ and Kn are small paramters. They were able to show that the normal stress effects and the temperature anisotropy in granular fluids are Burnett order effects.

Some of these models have been reasonably successful in describing the fluidised and quasi-elastic regime, but fail to explain the whole range of behaviour of granular flows. Under such circumstances, the discrete particle simulation of these flows could be very helpful in validating various continuum models and also establishing their range of validity.

In this chapter we have computed various rheological quantities and compared them with the theoretical results.

4.1.1 Stresses and viscosity

The momentum transfer at particle level manifests at the macroscopic level as continuum stresses. The total stress tensor could be decomposed into two components : 'kinetic stress' and 'collisional stress'. The momentum transfer due to streaming motion of particles contributes to kinetic stress, while the momentum transfer due to particle collisions contribute to collisional stress. In this section we present the non-dimensional expressions for computing rheological quantities like shear stress, pressure, viscosity and first normal stress difference.

With $\tilde{W}$, $\tilde{W}/\tilde{g}$, $(\tilde{W}\tilde{g})^{1/2}$ and $\tilde{m}$ as the reference length, time, velocity, and mass, respectively, the relevant dimensionless quantities are:

$$d = \frac{\tilde{d}}{\tilde{W}}, \quad \rho = \frac{\tilde{\rho}}{\tilde{\rho_p}}, \quad t = \frac{\tilde{t}}{\left(\tilde{W}/\tilde{g}\right)^{1/2}}, \quad \mathbf{u} = \frac{\tilde{\mathbf{u}}}{\left(\tilde{g}\tilde{W}\right)^{1/2}}, \quad \mathbf{P} = \frac{\tilde{\mathbf{P}}}{\left(\tilde{\rho_p}\tilde{g}\tilde{W}\right)},$$

$$T = \frac{\tilde{T}}{\tilde{m_p}\tilde{g}\tilde{W}}, \quad \mu = \frac{\tilde{\mu}}{\tilde{\rho_p}\tilde{g}^{1/2}\tilde{W}^{3/2}} \tag{4.1}$$

where $\mathbf{u}$ is the fluctuation (peculiar) velocity, $\tilde{\rho_p}$ the material density of particles, $\mathbf{P}$ the stress tensor, T the granular energy and μ the shear viscosity.

Since the kinetic stresses arise due to the streaming motion of the particles, the expression for kinetic stress tensor is given by [22]:

$$\tilde{\mathbf{P}}_k = \tilde{m}\frac{\langle \tilde{\mathbf{u}}_i \otimes \tilde{\mathbf{u}}_i \rangle}{(\tilde{dy} * \tilde{L})} = \frac{n_b * \frac{\pi}{4} * \tilde{\rho_p} * \tilde{d}^2}{\tilde{dy} * \tilde{L}} \langle \tilde{\mathbf{u}}_i \otimes \tilde{\mathbf{u}}_i \rangle = \nu_b \tilde{\rho_p} \tilde{g} \tilde{W} \langle \mathbf{u}_i \otimes \mathbf{u}_i \rangle$$

$$\Rightarrow \mathbf{P}^k = \frac{\tilde{\mathbf{P}}_k}{(\tilde{\rho_p}\tilde{g}\tilde{W})} = \nu_b \langle \mathbf{u}_i \otimes \mathbf{u}_i \rangle \tag{4.2}$$

where $\tilde{m}$ is the binwise mass of the granular fluid, ν_b is binwise volume fraction, $(\tilde{dy} * \tilde{L})$ is the area of each bin and $\langle .. \rangle$ denotes binwise averaging over collisions.

Our interest is in the rapid flow regime where the particle collisions are assumed to be instantaneous and only binary collisions are considered. The momentum change during a collision is given by the expression for impulse $\tilde{I}_{ij}$ in Eqn. (2.5). Hence the collisional stress due to this momentum exchange can be expressed as :

$$\tilde{\mathbf{P}}^c = \frac{\tilde{d}}{\tau_d} \sum_{bin} \frac{\tilde{\mathbf{I}}_{ij} \otimes \mathbf{k}}{(\tilde{dy} * \tilde{L})} = \left(\frac{\pi}{4}\right) \left[\tilde{\rho_p}\tilde{g}\tilde{W}\right] \left[\frac{d^3}{\tau_d(dy * L)}\right] \sum_{bin} \mathbf{I_{ij}} \otimes \mathbf{k}$$

$$\Rightarrow \mathbf{P}^c = \frac{\tilde{\mathbf{P}}^c}{(\tilde{\rho_p}\tilde{g}\tilde{W})} = \left(\frac{\pi}{4}\right) \left[\frac{d^3}{\tau_d(dy * L)}\right] \sum_{bin} \mathbf{I_{ij}} \otimes \mathbf{k} \tag{4.3}$$

where τ_d is the duration of the averaging time window and the sum is taken over all collisions during τ_d, where the particles i and j are involved. Note that kinetic stress (4.2) involves only bin averaging whereas collisional stress (4.3) involves both bin and time averaging. At low densities the kinetic stress is dominant since the collision rate is small and the mean free path of particles is large, whereas at high densities the collisional stress is dominant since the collision rate is large and the mean free path is small.

The total stress can be decomposed into pressure and shear stress :

$$\mathbf{P} = \mathbf{P}^k + \mathbf{P}^c = p\mathbf{1} + \mathbf{\Pi}, \tag{4.4}$$

where p is the pressure, $\mathbf{\Pi}$ is the stress deviator and $\mathbf{1}$ the unit tensor. From the off-diagonal components of the deviatoric stress, we can calculate the *shear viscosity* which relates the rate of strain to the shear stress:

$$\mu = -\Pi_{xy} / \frac{\mathrm{d}u}{\mathrm{d}y}. \tag{4.5}$$

The diagonal components of the stress deviator could be different from zero, giving rise to an anisotropic stress tensor. The magnitude of the stress anisotropy can be quantified by the first normal stress difference [1, 2, 3, 4]

$$\mathcal{N}_1 = \frac{\Pi_{xx} - \Pi_{yy}}{p}. \tag{4.6}$$

Note that this quantity is scaled by pressure to obtain its relative magnitude with respect to pressure. For a standard Newtonian fluid $\mathcal{N}_1 = 0$ and a non-zero $\mathcal{N}_1$ indicates the non-Newtonianess of the fluid.

The granular energy or the granular temperature which is a measure of the

random motion of the particles with respect to the mean motion is given by Eqn. (2.10e).

The simulations are carried out for a wide range of average volume fractions, varying from the dilute to the dense limit, over a range of values for the coefficient of restitution ($e_n = 0.99-0.8$) and tangential coefficient of restitution ($\beta_w = 0.9-0.1$). As mentioned in an earlier section of the paper, all the simulations were performed at $N = 900$ and $W/d = 31$. An increase in the N by about four times ($N \sim 4000$) did not affect the reported quantities noticeably, in the quasi-elastic limit.

4.1.2 Theoretical expressions for rheological quantities

The theoretical expressions for viscosity, shear stress and pressure for identical, rough, inelastic and circular disks were derived from kinetic theory by Jenkins and Richman[41]. For quasi-elastic collisions and nearly smooth particles, these expressions reduce to the forms given below.

The total stress is given by :

$$\hat{P}_{\alpha\beta} = p\,\delta_{\alpha\beta} - 2\mu\hat{D}_{\alpha\beta} \tag{4.7}$$

where, p is the pressure, μ is the shear viscosity and $\hat{D}_{\alpha\beta}$ is the deviatoric part of the deformation tensor $D_{\alpha\beta}$ that are given by

$$p \equiv \rho T(1+2G), \tag{4.8}$$

$$2\mu \equiv (m\nu/d)\,(T/\pi)^{1/2}\left[(8/\pi)\,G + \left(G^{-1}+2+G\right)\right], \tag{4.9}$$

$$\hat{D}_{\alpha\beta} \equiv \frac{1}{2}(\nabla u + (\nabla u)^T). \tag{4.10}$$

In the equation (4.8) $G \equiv \nu g_0$, where ν is the volume fraction and g_0 is the radial distribution function for disks at contact [95], given by

$$g_0 = \frac{1-\frac{7}{16}\nu}{(1-\nu)^2}. \tag{4.11}$$

Note that shear stresses, $\hat{\tau}_{\alpha\beta}$, are given by the off-diagonal components of $\hat{P}_{\alpha\beta}$:

$$\hat{\tau}_{\alpha\beta} = -(m\nu/d)\,(T/\pi)^{1/2}\left[(8/\pi)\,G + \left(G^{-1}+2+G\right)\right]. \tag{4.12}$$

We substitute the temperature, volume fraction and velocity profiles from our simulations into the above equations to obtain shear stress, pressure and viscosity as functions of y-coordinate.

4.1.3 Comparison of simulation and theoretical results

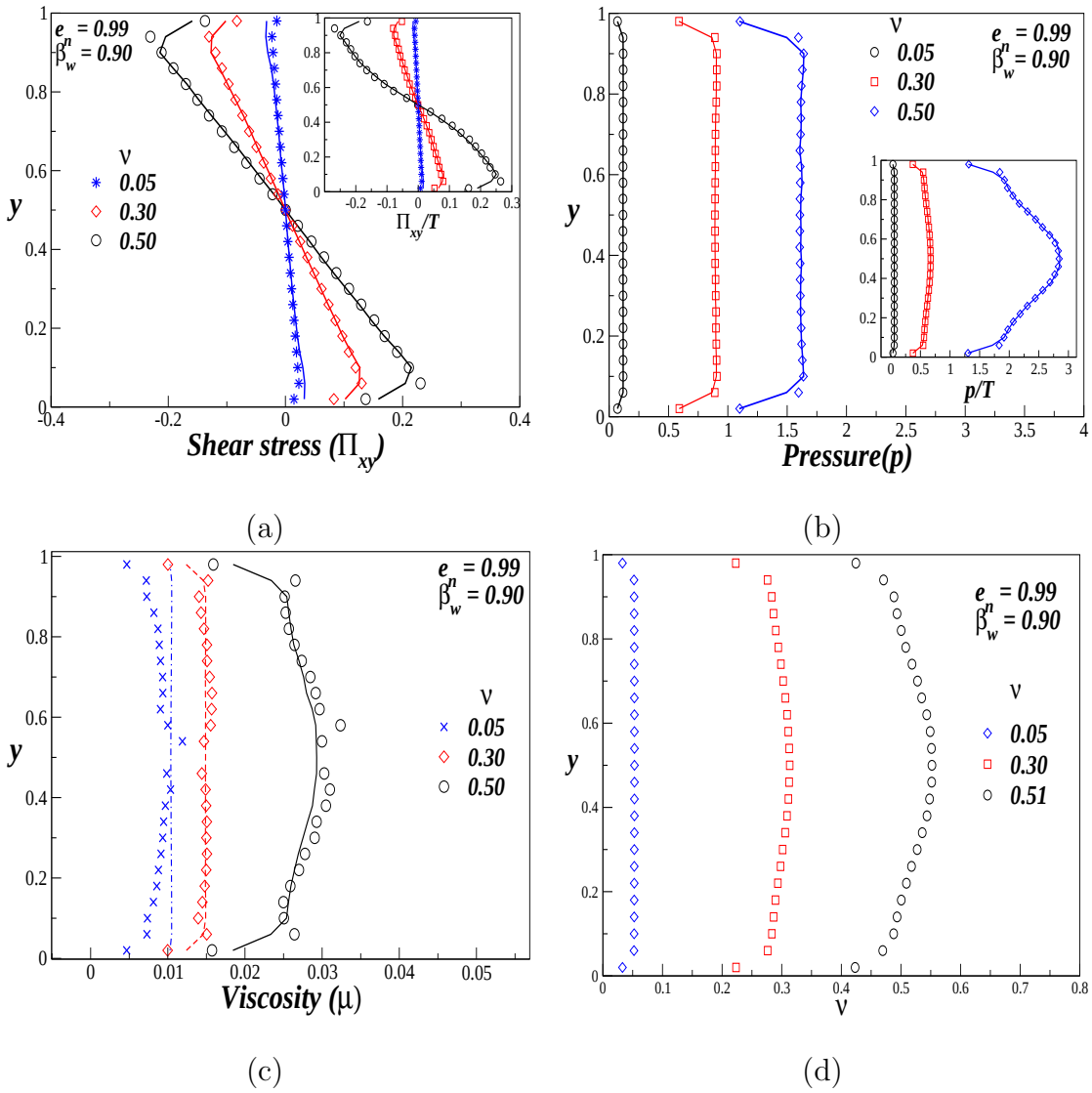

Figure 4.1: Variations of (a) shear stress, (b) pressure, (c) viscosity and (d) volume fraction across the width of the channel for a smooth wall and quasi-elastic collision. The symbols represent simulation results and continuous lines represent theoretical results. The parameter values are $\beta_w = 0.9$ and $e_n = 0.99$ at $\nu = 0.05, 0.3, 0.50$.

We compare our simulation results on shear stress, pressure and viscosity with the prediction of equations (4.7), (4.8) and (4.9), respectively. Most of the simulations were performed by fixing the particle number at $N = 900$ and aspect ratio at $W/d = 31$ and whenever these parameters are changed it would be stated explicitly. A comparison of simulation (symbols) and theoretical (continuous lines) results in the quasi-elastic limit for smooth walls ($\beta_w = 0.9$) are shown in Fig. 4.1 and the

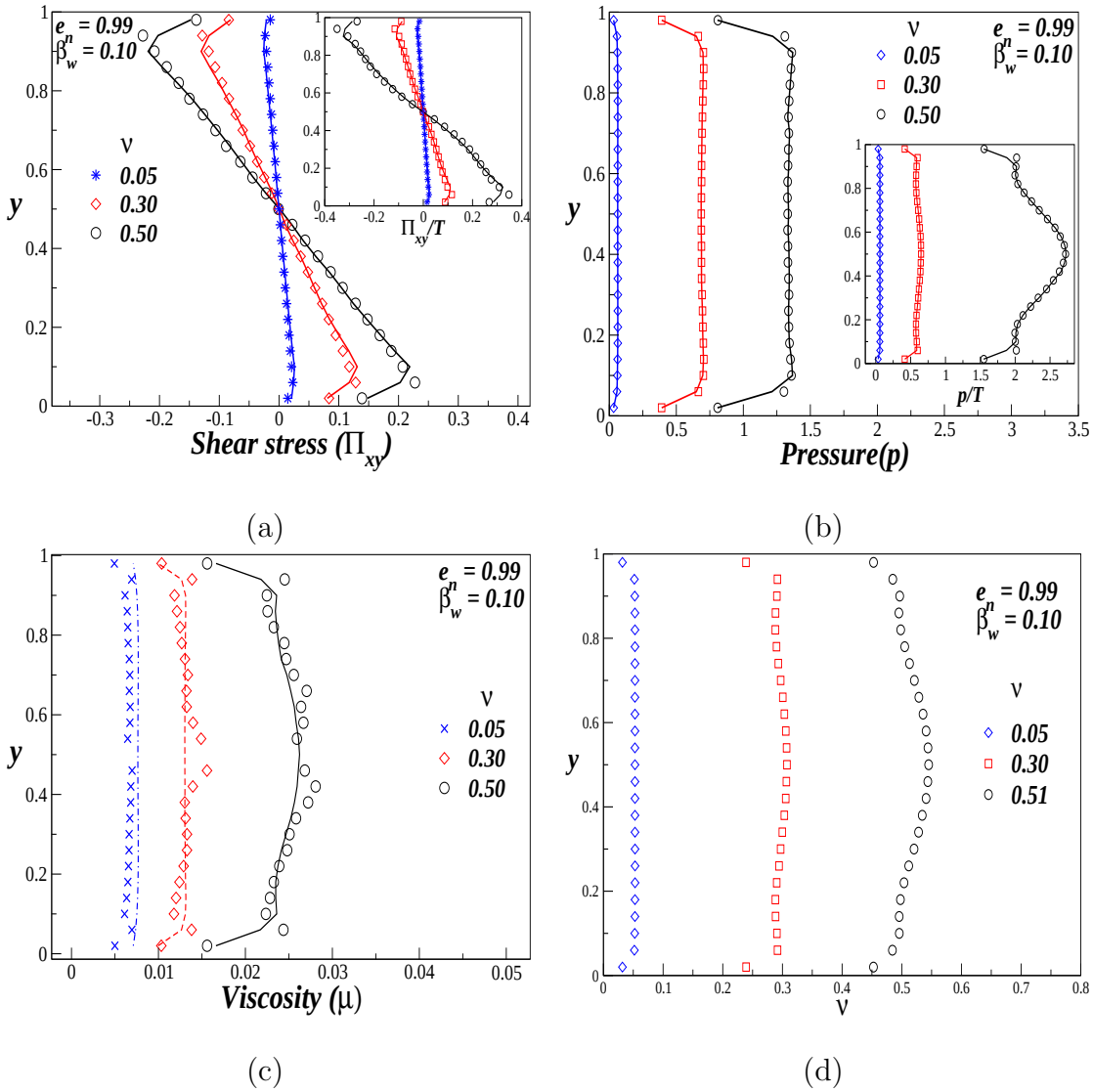

Figure 4.2: Variations of (a) shear stress, (b) pressure, (c) viscosity and (d) volume fraction across the width of the channel for a rough wall and quasi-elastic collision. The symbols represent simulation results and continuous lines represent theoretical results for a wall roughness of $\beta_w = 0.1$ at $\nu = 0.05, 0.3, 0.50$ and $e_n = 0.99$. The shear stress and pressure profiles scaled by temperature is shown in the insets of (a) and (b), respectively.

results for rough walls ($\beta_w = 0.1$) are shown in Fig. 4.2. There is a good agreement between simulation and theory over a wide range of densities. The shear stress and pressure profiles scaled by the temperature are shown in the inset of respective plots. The density/volume fraction profiles at different average volume fractions are shown in Fig. 4.1(d) and Fig. 4.2(d). An increase in the average volume fraction enhances the gradients of density along y-direction, which is an indication of clustering of particles at the centre of the channel.

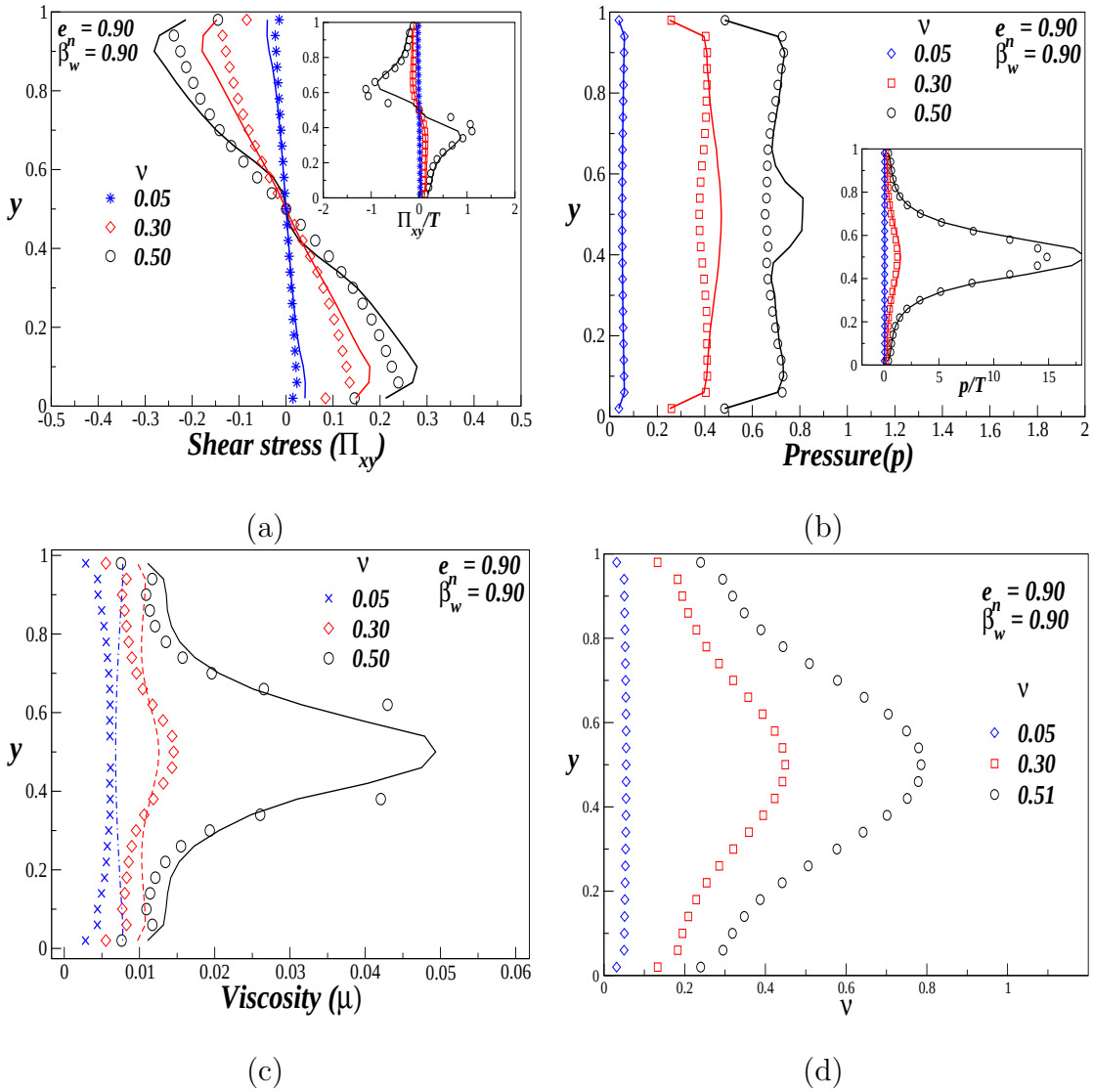

Figure 4.3: Variations of (a) shear stress, (b) pressure, (c) viscosity and (d) volume fraction across the width of the channel for a smooth wall and quasi-elastic collision. The symbols represent simulation results and continuous lines represent theoretical results for a wall roughness of $\beta_w = 0.9$ at $\nu = 0.05, 0.3, 0.50$ and $e_n = 0.90$. The shear stress and pressure profiles scaled by temperature is shown in the insets of (a) and (b), respectively.

Now we would like to concentrate on the effects of restitution coefficient on rheological quantities. The results presented in Figs. 4.3 (a) - (d) and 4.4(a) - (d) were computed for wall roughness of $\beta_w = 0.9$ and 0.1, respectively, at $e_n = 0.9$. From these figures it is clear that the discrepancies between the theoretical and simulation results become appreciable only at moderate and high densities. The density profiles in Figs. 4.3 & 4.4 indicate the formation of a plug at the centre of the channel for $\nu \sim 0.5$, and the viscosity profile shows a divergence in the plug

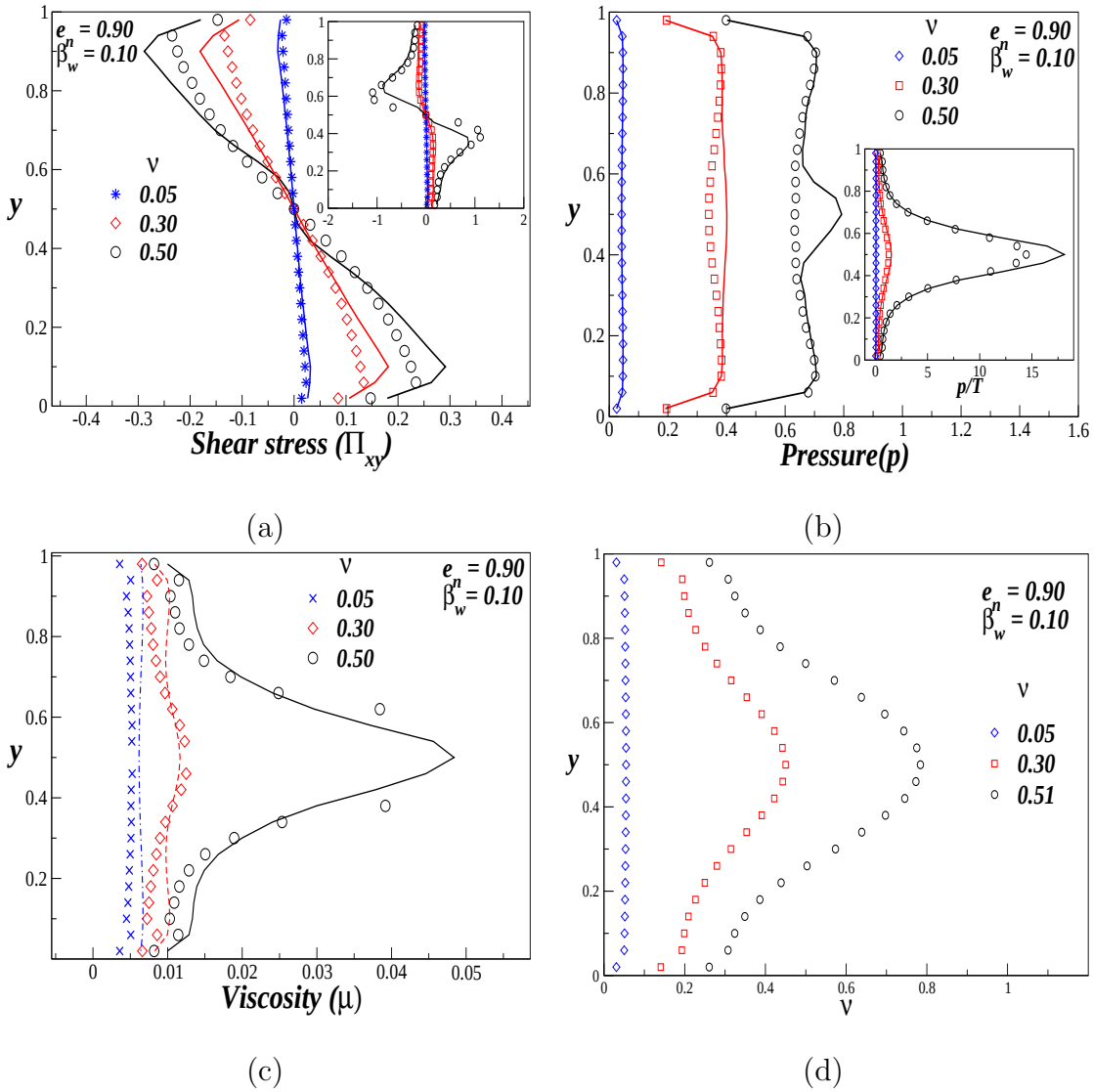

Figure 4.4: Variations of (a) shear stress, (b) pressure, (c) viscosity and (d) volume fraction across the width of the channel for a rough wall and quasi-elastic collision. The symbols represent simulation results and continuous lines represent theoretical results for a wall roughness of $\beta_w = 0.1$ at $\nu = 0.05, 0.3, 0.50$ and $e_n = 0.90$. The shear stress and pressure profiles scaled by temperature is shown in the insets of (a) and (b), respectively.

region. The discrepancies are due to inelastic collisions which are further enhanced at $e_n = 0.8$, shown in Fig. 4.5.

4.1.4 First normal stress difference

The first normal stress difference $\mathcal{N}_1$, Eqn. (4.6), is a measure of the degree of non-Newtonianess of the fluid. Figs. 4.6(a) and (b) show first normal stress difference

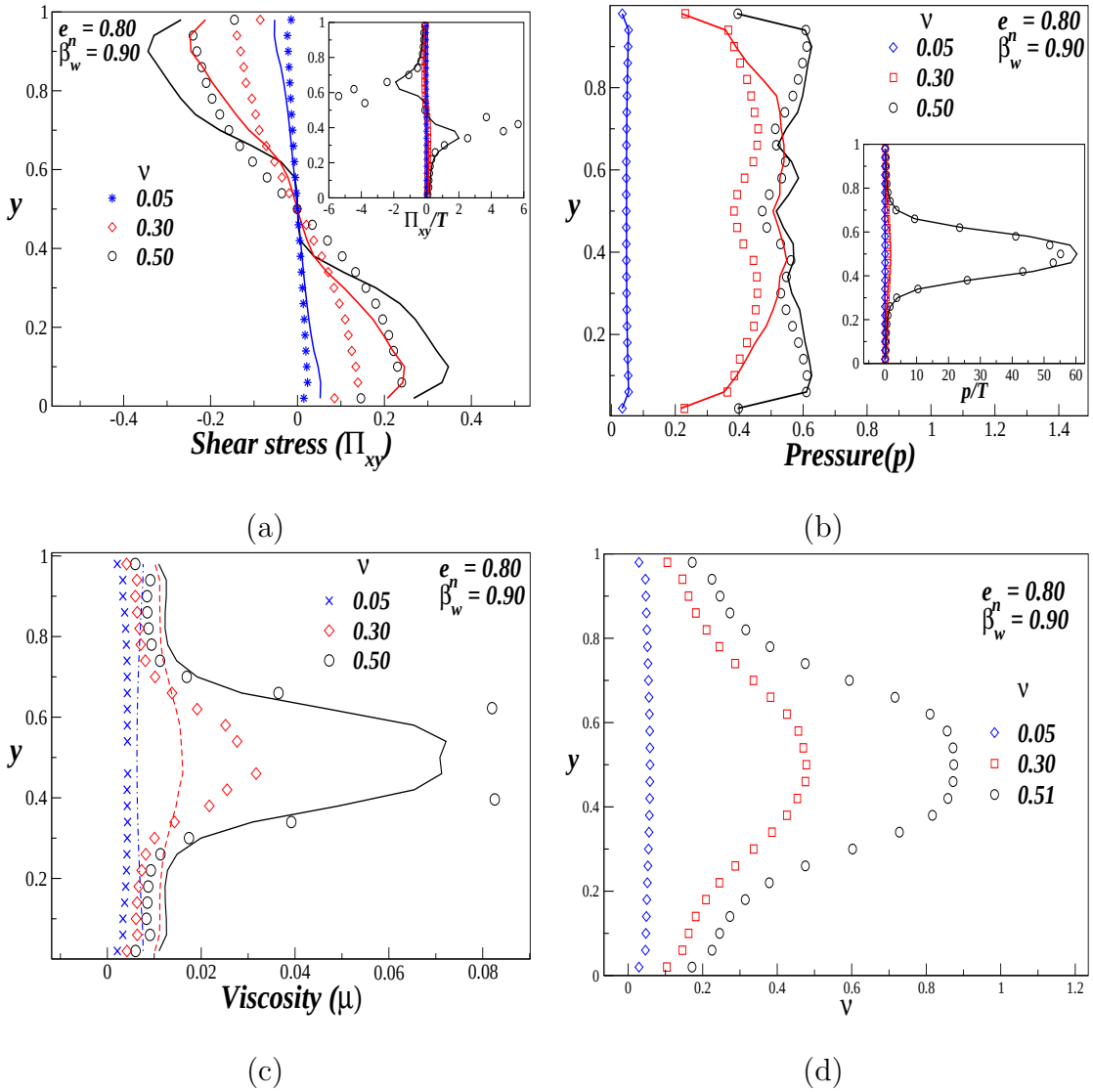

Figure 4.5: Variations of (a) shear stress, (b) pressure, (c) viscosity and (d) volume fraction across the width of the channel for a rough wall and quasi-elastic collisions. The symbols represent simulation results and continuous lines represent theoretical results for a wall roughness of $\beta_w = 0.9$ at $\nu = 0.05, 0.3, 0.50$ and $e_n = 0.80$. The shear stress and pressure profiles scaled by temperature is shown in the insets of (a) and (b), respectively.

profiles at different average volume fractions at $e_n = 0.99$ and for wall roughness of $\beta_w = 0.9$ and 0.1, respectively. The magnitude of $\mathcal{N}_1$ is small for $e_n = 0.99$ over a wide range of volume fractions. It is observed that the effect of walls roughness on $\mathcal{N}_1$ in the dense limit is confined to a small region near the wall, whereas in the dilute limit even the region near the center-line of channel is affected.

The first normal stress difference, $\mathcal{N}_1$, at different volume fractions for $e_n = 0.8$ and smooth ($\beta_w = 0.9$) and rough ($\beta_w = 0.1$) walls are shown in Fig. 4.7(a) & (b),

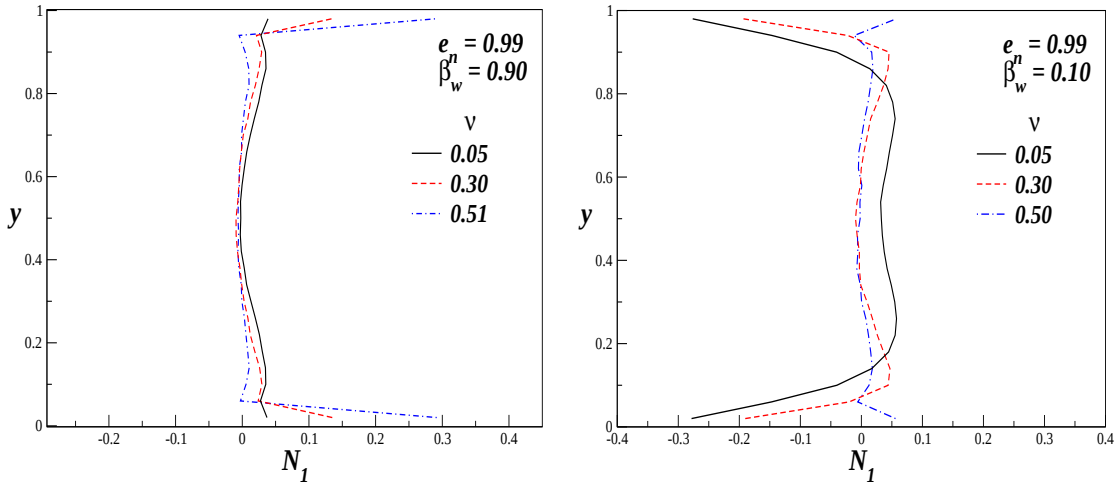

(a) (b)

Figure 4.6: The first normal stress difference profiles across the channel for (a) $\beta_w = 0.9$ and (b) $\beta_w = 0.1$, at different average volume fraction and $e_n = 0.99$

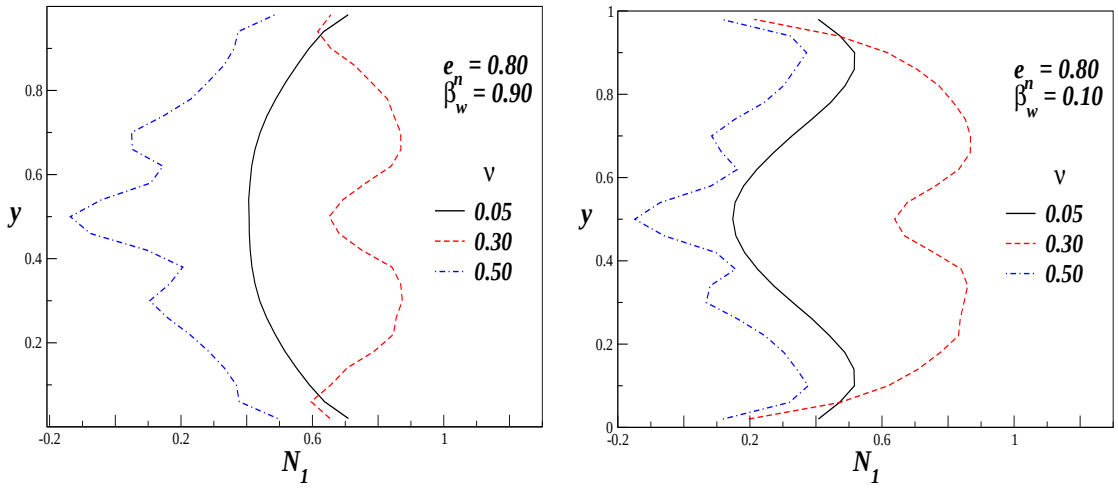

(a) (b)

Figure 4.7: The first normal stress difference profiles across the channel for (a) $\beta_w = 0.9$ and (b) $\beta_w = 0.1$, at different average volume fraction and $e_n = 0.80$

respectively. Clearly, the value of $\mathcal{N}_1$ increases due to increase in dissipation. Further, $\mathcal{N}_1$ has a nonmonotonic variation with volume fraction. Initially $\mathcal{N}_1$ increases at low densities, reaches a maximum value at some moderate density and then decreases with further increase in density. Interestingly, $\mathcal{N}_1$ reverses sign near the channel center-line beyond a critical density, Fig. 4.7. At $\nu = 0.50$ and $e_n = 0.8$, the first normal stress difference is negative at the center of the channel as shown

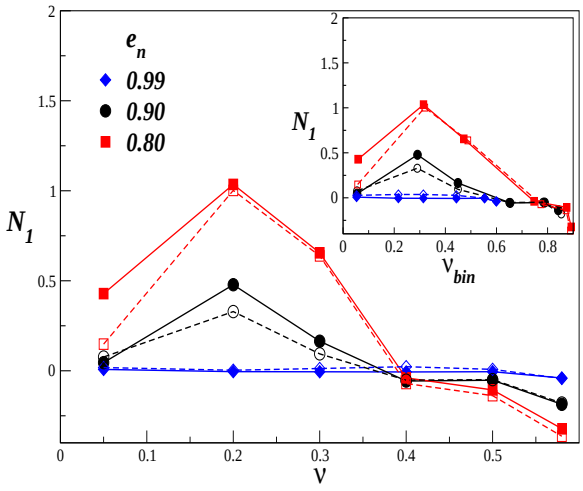

Figure 4.8: Variation of first normal stress difference with average volume fraction at the center of channel for $e_n = 0.8, 0.9$. In the inset $\mathcal{N}_1$ is plotted against the local volume fraction or the bin volume fraction. The filled symbols represents smooth walls ($\beta_w = 0.9$) and open symbols represents rough walls ($\beta_w = 0.1$).

in Fig. 4.7. To get a better picture of the negative first normal stress difference, we shift our focus to the center-line region of the channel. In Fig. 4.8, the effect of average volume fraction on the first normal stress difference at the channel center-line is shown. $\mathcal{N}_1$ varies non-monotonically with volume fraction and reverses its sign at a critical density depending on the value of e_n. The inset in Fig. 4.8 displays $\mathcal{N}_1$ as a function of the local (binwise) volume fraction at the center-line of the channel. Since the system is inhomogeneous, the variation of $\mathcal{N}_1$ with the local volume fraction is more meaningful. We observe that decreasing the coefficient of restitution increases the critical density beyond which $\mathcal{N}_1$ is negative.

The first normal stress difference $\mathcal{N}_1$ in a dense sheared granular fluid was earlier studied by Alam & Luding [1]. They showed that the kinetic component of first normal stress difference, $\mathcal{N}_1^k$, is maximum in the dilute limit and decays to zero at high volume fractions, whereas the collisional part, $\mathcal{N}_1^c$, is a non-monotonic function of density, which increases from zero in the dilute limit, reaches a maximum value at some intermediate density and then decreases, attaining a negative value above a critical density depending on the coefficient of restitution. In the dilute limit, the total normal stress difference follows the behaviour of $\mathcal{N}_1^k$ but at high densities its behaviour is dictated by $\mathcal{N}_1^c$. The reversal in the sign of $\mathcal{N}_1^c$ was further related to a preferred value of the collision angle due to the microstructural re-organisation of particles. This explained the sign reversal of $\mathcal{N}_1$ in the dense sheared granular fluid.

We take a similar approach here to understand the origin of negative first normal stress difference in granular Poiseuille flow. The first normal stress difference at $e_n = 0.99$, Fig. 4.8, indicates a small negative value at a low volume fraction of

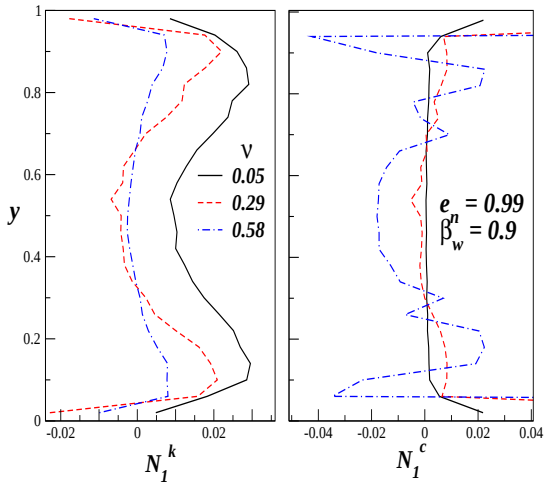

(a) (b)

Figure 4.9: Profiles of (a) kinetic part and (b) collisional part of first normal stress difference across the channel at $e_n = 0.99$ and different average volume fractions for smooth walls ($\beta_w = 0.9$).

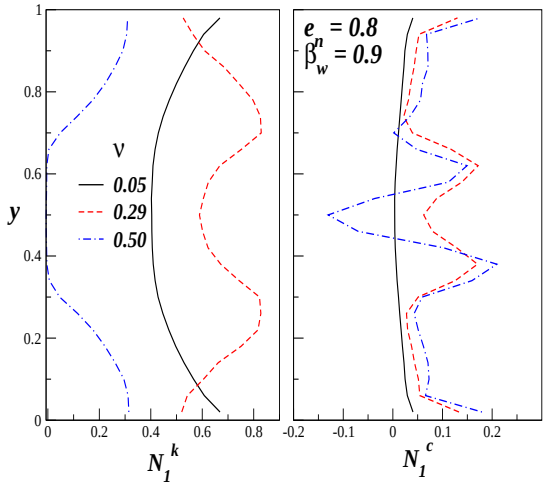

(a) (b)

Figure 4.10: Profiles of (a) kinetic component $\mathcal{N}_1^k$ and (b) collisional component $\mathcal{N}_1^c$ of first normal stress difference across the channel at $e_n = 0.80$ and different average volume fractions for smooth walls ($\beta_w = 0.9$).

$\nu \sim 0.2$ and it appears due to the kinetic component of $\mathcal{N}_1$, as shown in Fig. 4.9. The reason for this behaviour is not clear at this moment, so we concentrate on the high density region where the negative $\mathcal{N}_1$ is observed due to the collisional component. In Figs. 4.10(a) and (b), the kinetic and collisional parts of the first

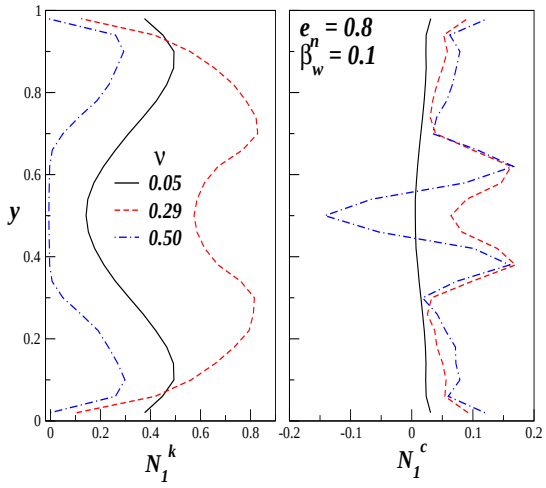

(a) (b)

Figure 4.11: Profiles of (a) kinetic component $\mathcal{N}_1^k$ and (b) collisional component $\mathcal{N}_1^c$ of first normal stress difference across the channel at $e_n = 0.80$ and different average volume fractions for rough walls ($\beta_w = 0.1$).

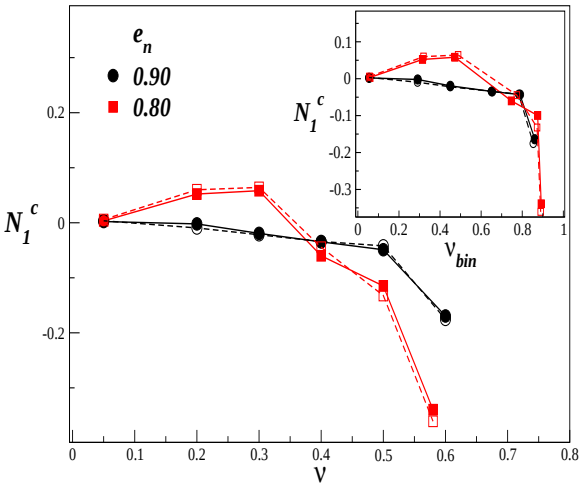

Figure 4.12: Variation of collisional component of first normal stress difference with average volume fraction at the center of channel for $e_n = 0.8, 0.9$. In the inset $\mathcal{N}_1^c$ is plotted against the local volume fraction or the bin volume fraction. The filled symbols represents smooth walls ($\beta_w = 0.9$) and open symbols represents rough walls ($\beta_w = 0.1$).

normal stress difference at different densities at $e_n = 0.8$ for smooth walls ($\beta_w = 0.9$) are shown. A similar plot for rough walls ($\beta_w = 0.1$) is shown in Fig. 4.11. We see that both $\mathcal{N}_1^k$ and $\mathcal{N}_1^c$ vary non-monotonically with increasing average volume fraction. The kinetic component of the first normal stress difference, at the centerline of the channel, decays to zero at high volume fractions (Fig. 4.10(a) &

Fig. 4.11(a)), whereas the collisional component reverses its sign beyond a critical volume fraction (Fig. 4.10(b) and Fig. 4.11).

We turn our attention to the collisional component of $\mathcal{N}_1$, $\mathcal{N}_1^c$, at the center-line of the channel, Fig. 4.12. At $e_n = 0.90$, $\mathcal{N}_1^c$ has a small negative value over a range of average volume fractions ($\nu \sim 0.3 - 0.5$), and becomes significant only at large volume fractions ($\nu \sim 0.6$). Similar observations could be made in the inset of Fig. 4.12, where $\mathcal{N}_1^c$ is presented as a function of the local volume fraction. These results at $e_n = 0.9$ are in variance with those presented in Ref. [1], where a negative $\mathcal{N}_1^c$ was observed only at high volume fractions ($\nu > 0.6$).

We now present the sign reversal of $\mathcal{N}_1$ concisely in the form of a phase diagram in the ($\nu_{bin} - e_n$) and ($\nu - e_n$) planes as shown in Fig. 4.13. It is to be noted that the zeros of the first normal stress difference are plotted against the local volume fraction or the average volume fraction where the first normal stress changes its sign. In Fig. 4.13, the solid line indicates the zeros of $\mathcal{N}_1$, the region below it has positive $\mathcal{N}_1$ and the region above it has negative $\mathcal{N}_1$. The dashed line with cross marks indicate the zeros of the collisional component of the first normal stress difference, $\mathcal{N}_1^c$. In Fig. 4.13(a) & (b), we note that the zero lines of $\mathcal{N}_1$ and $\mathcal{N}_1^c$ coincide with each other at lower e_n and deviate at higher e_n, with the $\mathcal{N}_1^c$ attaining a zero a lower volume fraction compared to $\mathcal{N}_1$.

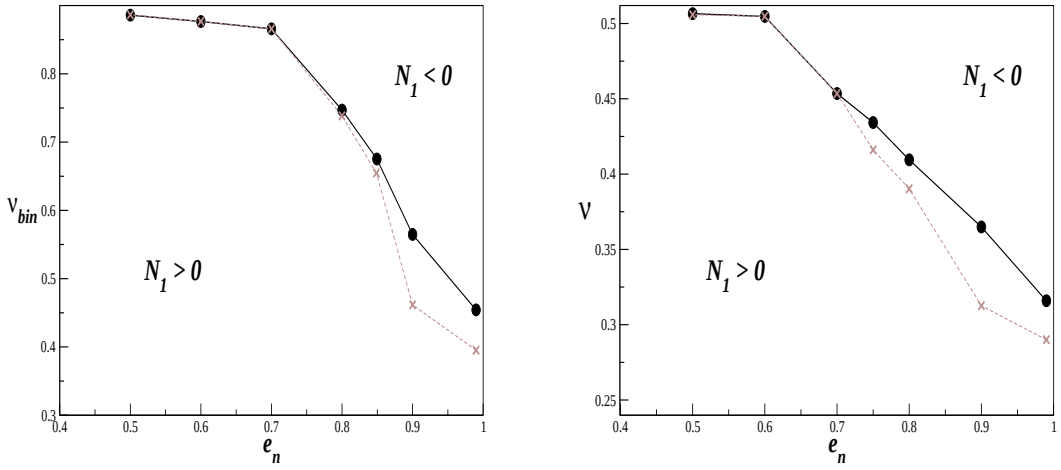

(a) (b)

Figure 4.13: The phase-diagram shows the regions of positive and negative first normal stress difference, $\mathcal{N}_1$, on a (a) ($\nu_{bin} - e_n$) plane and (b) ($\nu - e_n$) plane. The solid line indicates $\mathcal{N}_1 = 0$, the region above has negative $\mathcal{N}_1$ and the region below has positive $\mathcal{N}_1$. The dashed line with cross marks indicate $\mathcal{N}_1^c = 0$.

4.2 Velocity and temperature boundary conditions

4.2.1 Background

The boundary conditions at the solid-liquid interface has been widely debated. Traditionally, in continuum analysis, the no-slip condition at the fluid-solid interface is imposed to avoid finite discontinuities in the velocity gradient and viscous stresses at the wall. But it has been confirmed by numerous experimental and numerical works that fluid flows indeed exhibit finite slip [8, 12, 15, 24, 25, 65]. The magnitude of slip depends on various factors like the length scale of the flow, surface roughness, hydrophobicity, *etc.,* and also on the nature of the fluid, whether a Newtonian liquid, non-Newtonian liquid or gas.

Gas flows show significant slip when the Knudsen number, which is the ratio of the mean free path of the gas molecules to the characteristic length of the flow, is large for which the continuum assumption breaks down [27, 46]. In addition to slip, gases also exhibit temperature jump. The temperature jump is defined as the difference in the temperature of the fluid near the wall (T_w) and the temperature of the wall (T_s).

In the following paragraphs we present a brief review of different slip and temperature jump models for compressible flows. According to the theory of compressible fluids [21], $Kn < 0.01$ is known as the *continuum* range, where the Navier-Stokes (NS) equations with no-slip boundary conditions govern the flow. In the $slip-flow$ regime ($0.01 < Kn < 0.1$), usually the no-slip boundary condition fails; the slip velocity in this regime is given by Maxwell's model, and the temperature jump at the boundary is given by a model proposed by von Smoluchowski (Kennard, [47]). In the *transition* regime ($Kn \geq 0.1$), the constitutive laws that define the stress tensor and heat flux breaks down, requiring higher-order corrections to the constitutive equations, given by the Burnett equations.

In the $slip-flow$ regime, the Navier-Stokes (NS) equations are solved in combination with slip and temperature jump boundary conditions [46], given by :

$$U_w - U_s = \frac{2-\sigma_v}{\sigma_v}\, Kn\, \frac{\partial U_s}{\partial y}, \tag{4.13}$$

$$T_w - T_s = \frac{2-\sigma_T}{\sigma_T}\, \left[\frac{2\gamma}{\gamma+1}\right] \frac{Kn}{Pr}\, \frac{\partial T}{\partial y}, \tag{4.14}$$

where U_w and T_w are the velocity and temperature of the flow at the wall, respectively, U_s and T_s are the reference wall velocity and temperature, respectively, σ_v and σ_T are the tangential momentum and energy accommodation coefficients, respectively, Pr is the Prandtl number and γ is the ratio of specific heats. Here the $y-$ coordinate is the wall normal direction. The above models are called as first order models and are applicable to the $slip-flow$ regime where the NS equations are valid. The tangential momentum accommodation coefficient (σ_v) characterises

the exchange of momentum and the temperature accommodation coefficient characterises (σ_T) the exchange of energy between the particles and wall. The case of $\sigma_v = 1$ is called specular reflection for which the tangential velocity of the molecules reflected from the walls is unchanged and the normal velocity of the molecules is reversed. On the other hand, $\sigma_v = 0$ is called the diffuse reflection for which the average tangential momentum of the reflected molecules is zero.

We now move on to higher order models that are applicable in the *transition* regime where $Kn > 0.1$ and the Navier-Stokes description breaks down. The effects of higher order terms in the Chapman-Enskog expansion become significant at high Knudsen numbers, so Burnett equations are more suited for describing such flows. Similarly, higher order corrections to the slip and temperature jump models may also become necessary. One of the first second-order slip model was given by Cercignani [21]. Using the BGK approximation, for a steady flow along the $x-$ direction and parallel to a stationary wall whose normal is pointing into the flow along the $y-$ direction, he obtained :

$$U_w = 1.016\ \theta\ \frac{\partial u}{\partial y}\ |_w\ -0.7667\ \theta^2\ \frac{\partial^2 u}{\partial y^2}\ |_w, \tag{4.15}$$

where $\theta = \mu\sqrt{2RT}/P$. Here u is the velocity of the gas, μ is the viscosity of the gas, R is the gas constant, T is the temperature, P is the pressure and $|_w$ denotes the magnitude near the wall. The above model was modified for a hardsphere gas by Hadjiconstantinou [35], who refined the coefficients based on the numerical results of Ohwada *et al.,* [70] to give :

$$U_w = \alpha\ Kn\ \frac{\partial u}{\partial y}\ |_w\ -\delta\ \theta^2\ \frac{\partial^2 u}{\partial y^2}\ |_w, \tag{4.16}$$

where $\alpha = 1.11$, $\delta \sim 0.61$ and Kn is the Knudsen number of the hardsphere gas. The flow-rate measured using this model and the DSMC results were in excellent for $Kn \leq 0.4$.

A higher order temperature jump boundary condition, based on the derivation given in Kennard [47], was proposed by Beskok and Karniadakis [46] :

$$T_s - T_w = \frac{2-\sigma_T}{\sigma_T}\ \left[\frac{2\gamma}{\gamma+1}\right]\frac{1}{Pr}\ \left[Kn\left(\frac{\partial T}{\partial n}\right)|_w + \frac{Kn^2}{2}\left(\frac{\partial^2 T}{\partial n^2}\right)|_w \ ...\right] \tag{4.17}$$

4.2.2 Slip and velocity gradient at the wall

In this section, we present the results on slip velocity in reference to gravity-driven granular Poiseuille flow. Our simulations show that the slip velocity depends on various control parameters *i.e.,* normal restitution coefficient (e_n), volume fraction (ν) and wall roughness (β_w).

We define the nondimensional slip velocity as the ratio of average velocity in the bins adjacent to walls (U_w) and the center line velocity (U_0) that are obtained from $U(y)$ profile in Eqn. (2.10c). In the present context, the Knudsen number is $Kn = \lambda/W$, where the mean free path λ is computed by averaging the displacement ($s = \sqrt{\delta x^2 + \delta y^2}$) of particles during successive collisions over a large number of collisions, and W is the channel width.

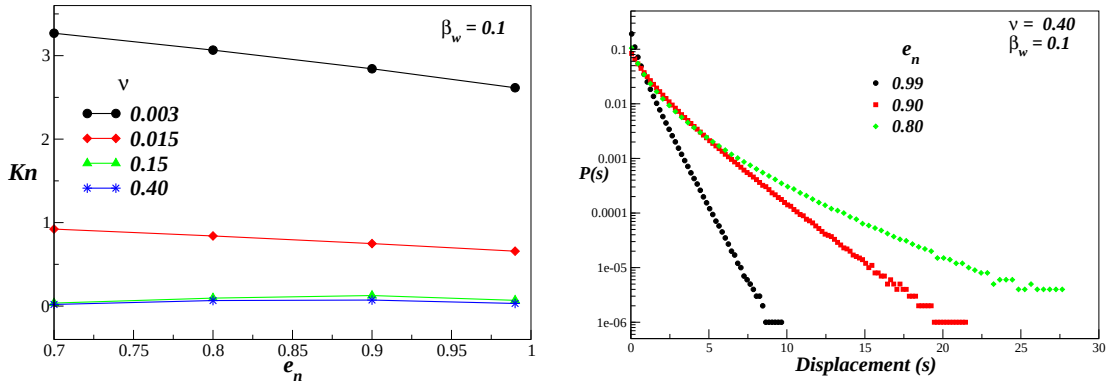

(a) (b)

Figure 4.14: Effect of e_n on Knudsen number (a) and distribution of particle displacement between collisions (b) at a wall roughness of $\beta_w = 0.1$. The change in Knudsen number with e_n is negligible, which is also evident from the distribution of displacement.

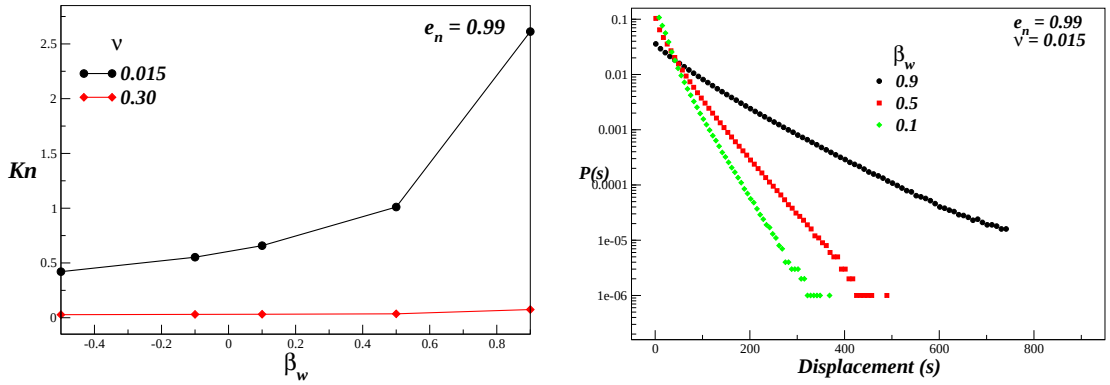

(a) (b)

Figure 4.15: Effect of wall roughness on (a) the Knudsen number and (b) distribution of particle displacement between collisions (b) at $e_n = 0.99$ is shown. The change in Knudsen number is appreciable in the dilute limit.

Before investigating the Knudsen number and slip velocity relation, we study the effect of different control parameters on Knudsen number and slip velocity and the velocity gradient near the wall. Figures 4.14(a) & (b) show the effect

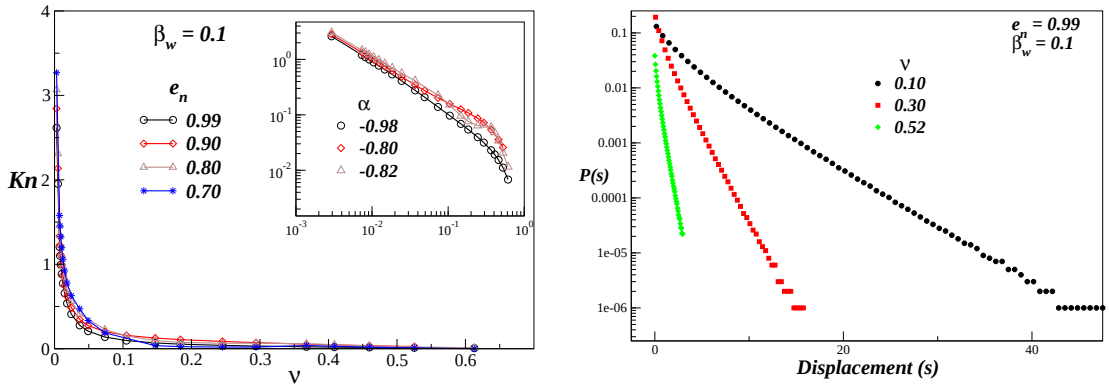

(a) (b)

Figure 4.16: Effect of volume fraction on (a) the Knudsen number and (b) distribution of particle displacement between collisions (b) at different values of dissipation. The inset in (a) shows the information presented in the main panel on a log-log plot and α indicate the slope.

of restitution coefficient (e_n) on Knudsen number and the distribution of particle displacement at a wall-roughness of $\beta_w = 0.1$. The results in Fig. 4.14(a) are presented at different volume fractions, each line corresponds to a particular volume fraction. It is observed that the effect of e_n on Kn is negligible over a wide range of volume fractions. The distribution of particle displacements in Fig. 4.14(b) shows an exponential decay and the decay rate is significantly affected by change in e_n.

In Figs. 4.15(a) & (b) the effect of wall roughness on Knudsen number and the distribution of particle displacement are shown. The effect is appreciable in the dilute limit and negligible in the moderate and dense limit. This could be inferred also from the distribution of displacement in Fig. 4.15(b).

In Figs. 4.16(a) & (b) the effect of volume fraction on Knudsen number is presented. The Knudsen number changes rapidly in the dilute regime and it approaches almost a constant value in the dense regime. The log-log plot in the inset of Fig. 4.16(a) shows that Kn is proportional to a negative power of ν, $Kn \propto \nu^{\alpha}$, over a wide range of volume fraction, when $e_n < 0.80$. The exponents are indicated as α in the inset. When the coefficient of restitution is reduced below $e_n = 0.80$, the variation of Knudsen number with volume fraction becomes non-monotonic and cannot be predicted by a power-law. The effects of clustering of particles become significant at low e_n and the observed non-monotonicity could be a consequence of clustering.

We present the effect of various control parameters on slip velocity in Fig. 4.17 - Fig. 4.21. The coefficient of restitution has a negligible effect on the slip velocity in the dilute as well as dense limit as shown in Figs. 4.17(a) & (b), which is surprising considering the fact that inelastic collisions lead to cluster formation that affects the dynamics of the flow. As seen in Fig. 4.17(b) the velocity profile around the

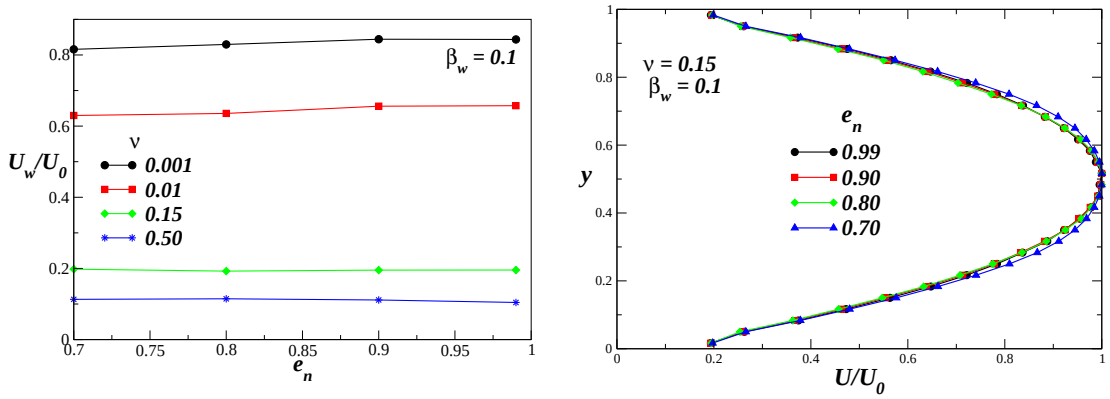

(a) (b)

Figure 4.17: Effect of the restitution coefficient (e_n) on (a) slip velocity and (b) velocity profile. Velocity profile undergoes changes at centre of the channel due to formation of clusters but clearly the velocity at the wall is unaffected.

centre of the channel changes but the velocity at walls is relatively unaffected. The slip velocity in Fig. 4.17(a) is computed at a wall-roughness of $\beta_w = 0.1$ and velocity profiles in Fig. 4.17(b) are at a volume fraction of $\nu = 0.15$ and a wall-roughness of $\beta_w = 0.1$. Further, the effect of dissipation on the velocity gradient near the walls is presented in Fig. 4.18, which is also relatively unaffected.

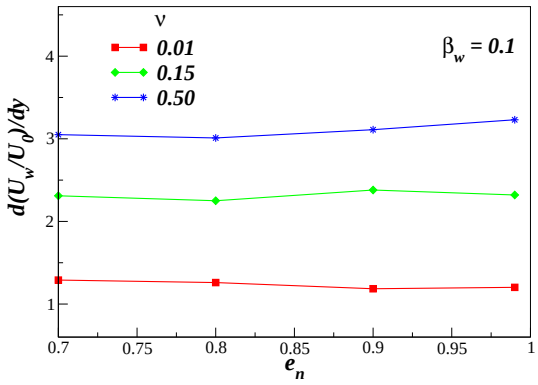

Figure 4.18: Effect of the restitution coefficient (e_n) on the velocity gradient near the wall for a wall-roughness of $\beta_w = 0.1$ at different densities.

Figures 4.19(a) & (b) show the effect of wall roughness (β_w) on slip velocity. As expected, the slip velocity increases with increase in wall smoothness in Fig. 4.19(a), which is also evident from the velocity profiles in Fig. 4.19(b). The values of parameters used in Fig. 4.19(a) are $e_n = 0.99$ and $\nu = 0.015, 0.30$ and in Fig. 4.19(b) are $e_n = 0.99$, $\nu = 0.015$ and $\beta_w = 0.1, 0.5, 0.9$. The velocity gradient near the wall varies non-monotonically with the wall-roughness as shown in Fig. 4.20.

The effect of volume fraction on slip velocity is shown in Fig. 4.21(a) & (b).

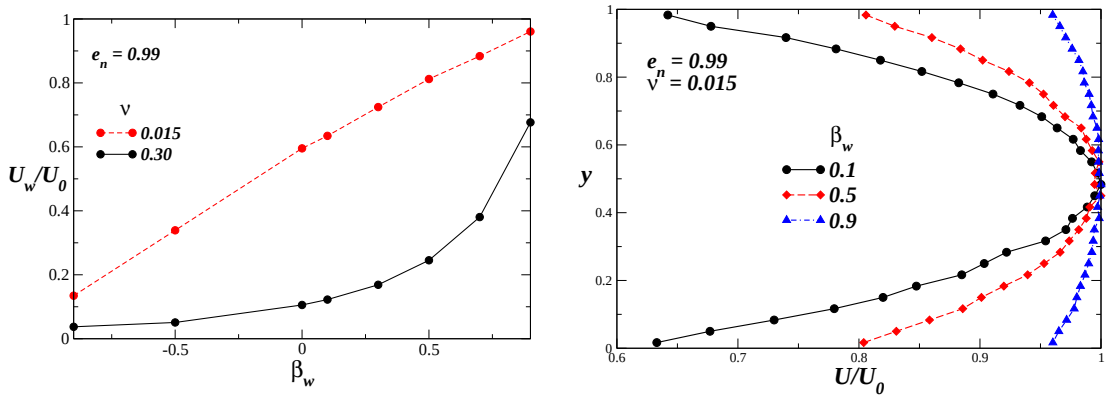

Figure 4.19: Effect of wall roughness (β_w) on (a) slip velocity and (b) velocity profile. Both plots indicate that wall roughness has a significant effect on slip velocity and the velocity gradients.

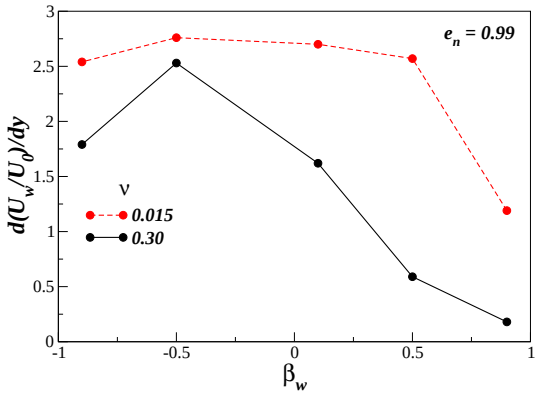

Figure 4.20: Effect of wall roughness on the velocity gradient near the wall for $e_n = 0.99$ at different densities.

The inset in Fig. 4.21(a) shows slip velocity and volume fraction curve on a log-log plot and the slip velocity varies as a negative power of the volume fraction over a range of volume fraction $\nu \sim (0.02 - 0.4)$ for the coefficient of restitution varying from $e_n \sim (0.99 - 0.80)$. At further lower values of e_n, clustering effects dominate the dynamics of the flow and the slip velocity behaves non-monotonically with volume fraction. These observations are similar to those made with reference to the variation of the Knudsen number with volume fraction. The variation of velocity gradient with the volume fraction is presented in Fig. 4.22. The inset displays the information of the main panel on a log-log plot. From this plot it is apparent that velocity gradient near the wall varies as a positive power of volume fraction over the range $e_n \sim (0.99 - 0.8)$ and $\nu \sim (0.005 - 0.5)$ with an exponent of $\alpha = 0.273$.

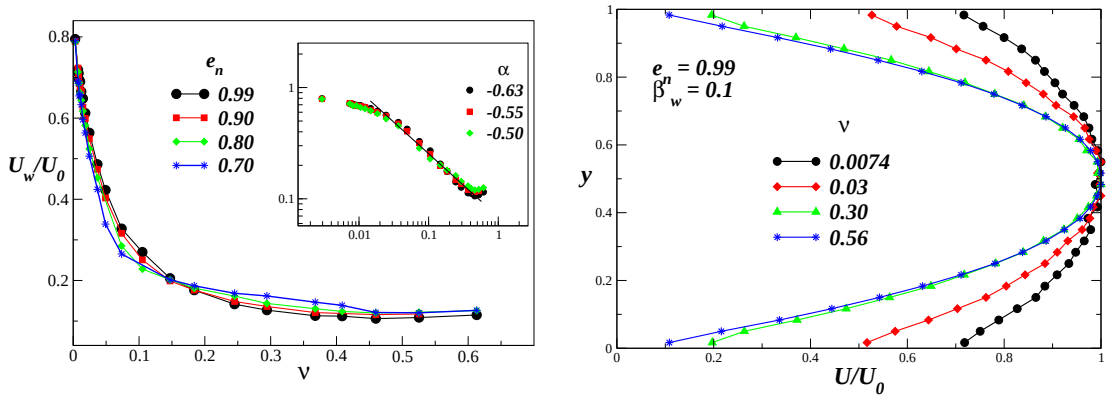

(a) (b)

Figure 4.21: Effect of volume fraction on (a) slip velocity and (b) velocity profiles. The plot (a) shows a rapid change in slip velocity in the dilute and approaches a constant value in the dense regime, which is also reflected in (b). The inset in (a) shows the information presented in the main panel on a log-log plot and α indicate the slope.

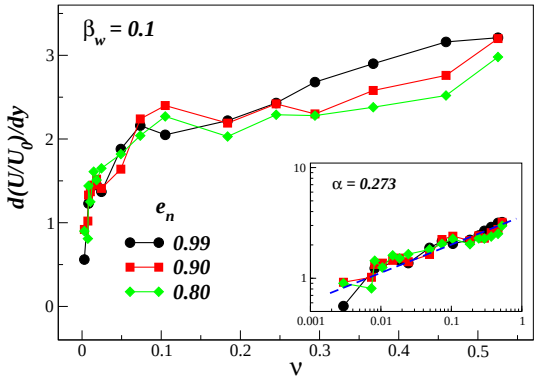

Figure 4.22: Effect of volume fraction on the velocity gradient near the wall for a rough wall at different values of dissipation. The inset shows the information in main panel on a log-log plot and the symbol α indicates the slope of the dashed line, obtained by least curve fitting.

Now we focus on $slip - Kn$ relation. In all the following plots, relating to $slip - Kn$ curve, the Knudsen number was varied by changing volume fraction from $\nu \sim (0.00074 - 0.6)$. Figure 4.23 shows the variation of slip velocity with Knudsen number for a wall-roughness of $\beta_w = 0.1$ at different values of dissipation (e_n). It is observed from the inset of Fig. 4.23 that the slip velocity varies as a positive power of the Knudsen number ($\frac{U_w}{U_0} \propto Kn^{\alpha}$) over a decade of Kn when $e_n \sim (0.99 - 0.9)$. The volume fraction was found to vary from moderate to very dilute values (*i.e.*, $\nu \sim 0.4 - 0.015$) over this range of Knudsen number. The robustness of these observations were confirmed by performing simulations using larger system size. In Fig. 4.23 the curve represented by open circles was

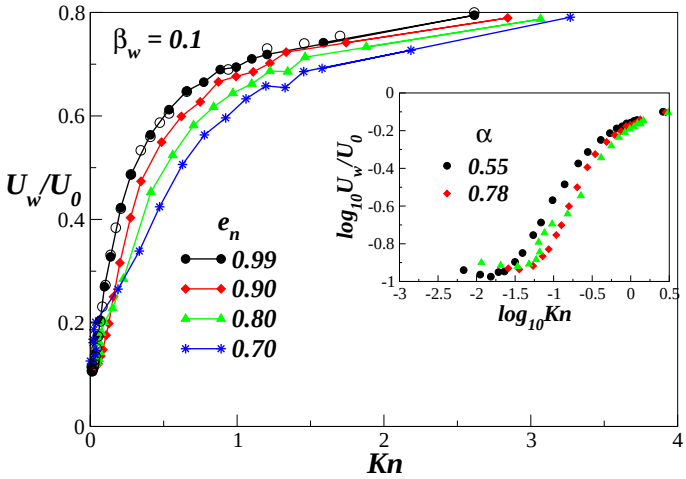

Figure 4.23: Variation of slip velocity with Kn at a wall roughness of $\beta_w = 0.1$ and different values of dissipation. The open circles were computed for $N = 1800$ particles at $e_n = 0.99$. The inset shows the information in the main panel on a log-log plot.

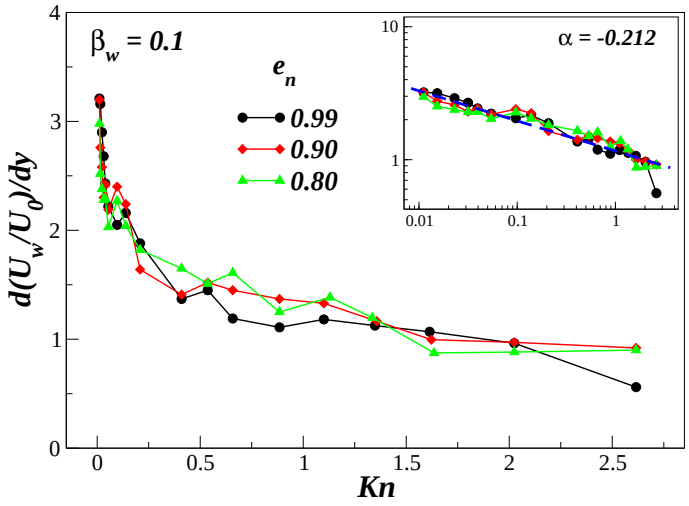

Figure 4.24: Variation of velocity gradient at the wall with Knudsen number for a wall-roughness of $\beta_w = 0.1$ and different values of dissipation. The inset shows the information in main panel on a log-log plot and the symbol α indicates the slope of the dashed line, obtained by least curve fitting.

computed using $N = 1800$ and $W/d = 31$ and there is a good agreement with the results obtained with $N = 900$ and $W/d = 31$ (filled circles). We have also investigated the relation between velocity gradient near the wall and the Knudsen number, which is presented in Fig. 4.24. It is observed that velocity gradient varies as a negative power of the Knudsen number (inset of Fig. 4.24) over the range $(Kn \sim (0.001 - 3))$ and $e_n \sim (1 - 0.8)$, with an exponent of $\alpha = 0.212$.

In the Fig. 4.25, $Slip - Kn$ curves at different wall roughness and $e_n = 0.99$ are

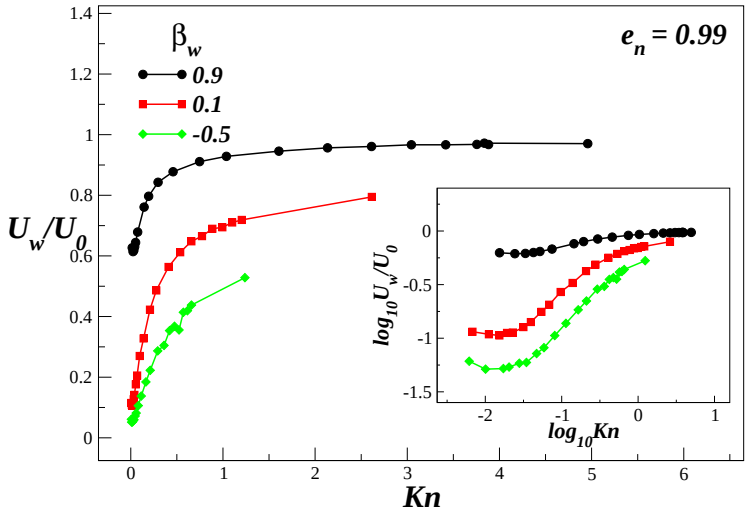

Figure 4.25: Slip velocity versus Kn plot at $e = 0.99$ and $\beta_w = 0.9, 0.1$ and -0.5. The inset shows the information in the main on a log-log plot.

shown. It is observed that at a given Knudsen number the slip velocity decreases with increasing wall roughness.

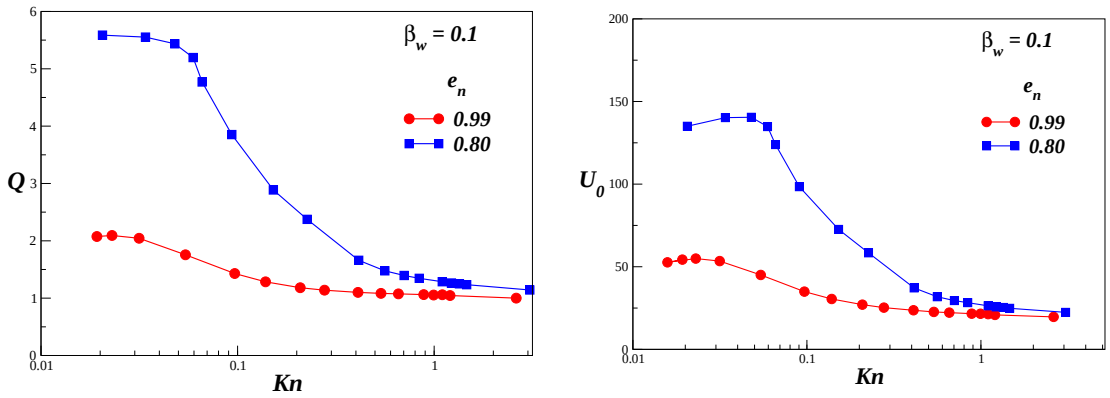

(a) (b)

Figure 4.26: The variation of (a) nondimensional average velocity (Q) and (b) centerline velocity (U_0) with the Knudsen number at a wall-roughess of $\beta_w = 0.1$.

We present a set of results on the variation of average velocity (Q) and velocity at the centerline of the channel (U_0) with the Knudsen number in Fig. 4.26(a) & (b), respectively. The nondimensional average velocity, Q, is given by the expression :

$$Q = \frac{\int U dy}{g^{1/2} W^{3/2}} \tag{4.18}$$

It is observed that both Q and U_0 are nearly constant for $Kn < 0.05$ and decreases

rapidly with further increase in Knudsen number Kn.

4.2.3 Wall temperature and temperature gradient

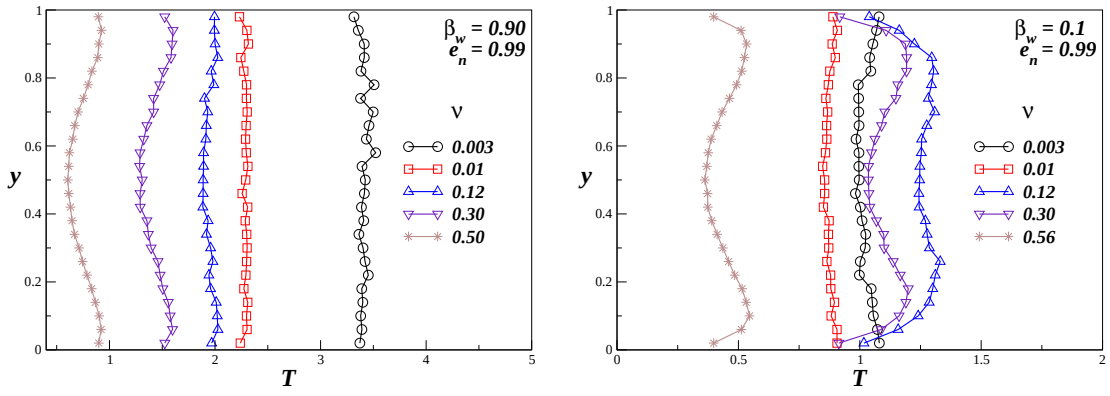

(a) (b)

Figure 4.27: Nondimensional temperature profiles at different particle volume fractions for (a) a smooth wall ($\beta_w = 0.9$) and (b) a rough wall ($\beta_w = 0.1$).

In this section we present the results on the effect of control parameters on the temperature and temperature gradient near the walls. The non-dimensional temperature profile at different volume fractions for a smooth wall ($\beta_w = 0.9$) and a rough wall ($\beta_w = 0.1$) are displayed in Figs. 4.27(a) & (b), respectively. At a wall roughness of $\beta_w = 0.9$, Fig. 4.27(a), the temperature across the channel decreases monotonically with increasing volume fraction, whereas at $\beta_w = 0.1$, Fig. 4.27(b), the temperature varies non-monotonically with the volume fraction.

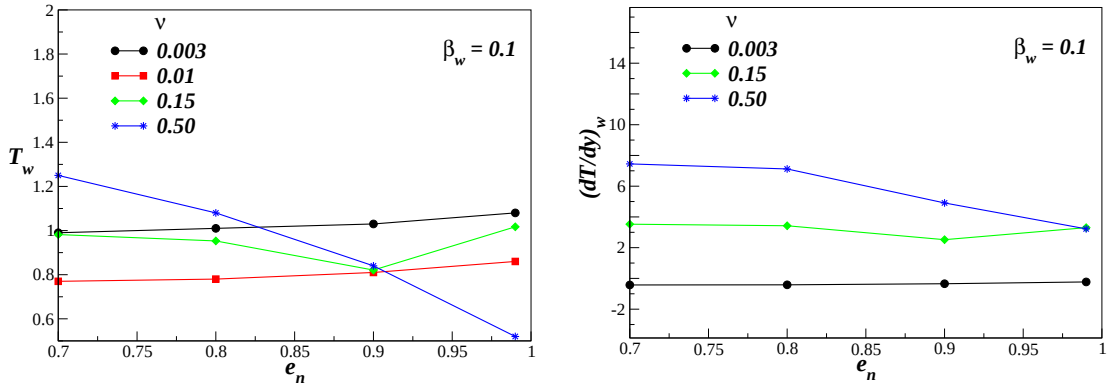

(a) (b)

Figure 4.28: Effect of dissipation on the (a) wall-temperature (T_w) and (b) temperature gradient at the wall, at different densities for a wall-roughness of $\beta_w = 0.1$.

The effect of restitution coefficient (e_n) on the temperature and temperature gradient at the wall, is shown in Figs. 4.28(a) & (b), respectively, for a wall-roughness of $\beta_w = 0.1$. From these plots it is apparent that the effects of dissipation are appreciable only at higher densities.

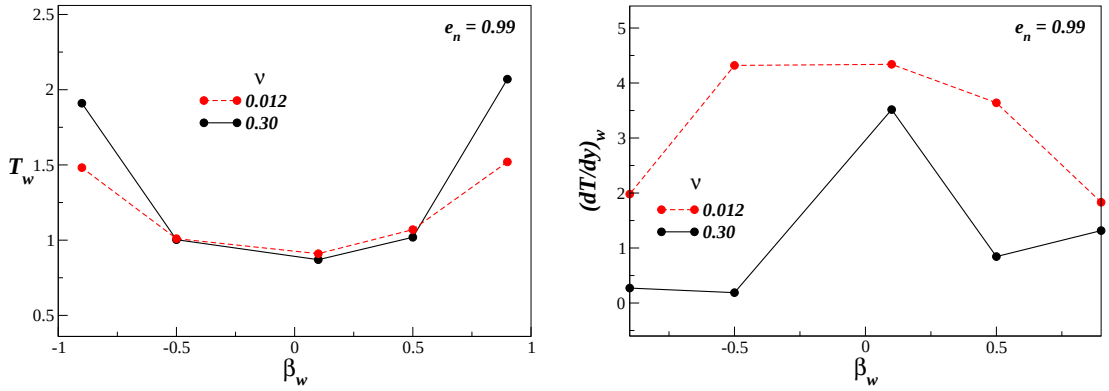

(a) (b)

Figure 4.29: Effect of wall-roughness on the (a) wall-temperature (T_w) and (b) temperature gradient at the wall, at different densities and $e_n = 0.99$.

The wall temperature (T_w) and temperature gradient ($(\frac{\partial T}{\partial y})_w$) display a non-monotonic variation with the wall-roughness. These results for the quasi-elastic limit ($e_n = 0.99$) are shown in Fig. 4.29. When the wall-roughness is close zero, the dissipation of energy at the walls due to wall-particle collisions is large, so the wall-temperature curve [Fig. 4.29(a)] has a minima near $\beta_w \sim 0$.

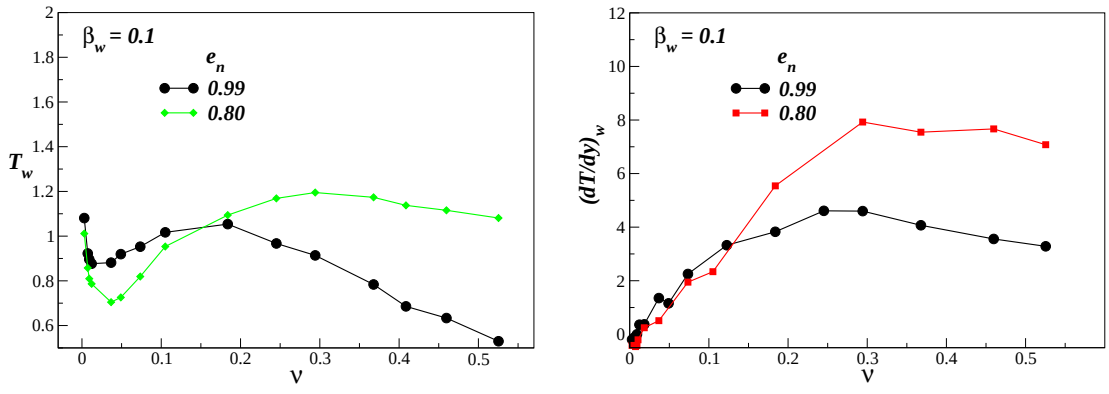

(a) (b)

Figure 4.30: Variation of (a) wall-temperature (T_w) and (b) temperature gradient with volume fraction at $e_n = 0.99, 0.80$ and for a wall-roughness of $\beta_w = 0.1$.

In Fig. 4.30, the wall-temperature and temperature gradient are plotted against

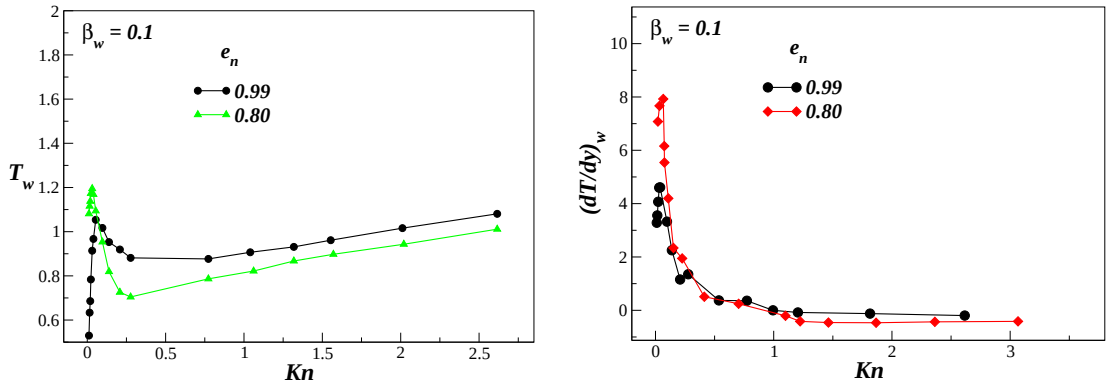

(a) (b)

Figure 4.31: Variation of (a) wall-temperature (T_w) and (b) temperature gradient with Knudsen number at $e_n = 0.99, 0.80$ and for a wall-roughness of $\beta_w = 0.1$.

volume fraction, whereas in Fig. 4.31 these quantities are plotted against the Knudsen number. Both T_w and $(\frac{\partial T}{\partial y})_w$ display a non-monotonic variation with volume fraction. On the other hand, the variation of wall-temperature is nearly linear at higher Kn, while the temperature gradient decreases rapdily at low and moderate Kn and approaches nearly a constant value at higher Kn .

CHAPTER 5

DENSITY WAVES

The formation of clusters due to inelastic collisions is one among the host of interesting phenomena exhibited by granular particles. This phenomenon has attracted the attention of many authors [33, 53, 60, 61, 62, 89, 92]. Clustering could be understood using simple and intuitive arguments [33]. Due to fluctuations the density in certain regions can increase, without a change in granular temperature, leading to an increased number of collisions compared to neighbouring areas. Since the collisions are inelastic, an increase in the collision rate would mean a greater rate of loss of energy in the denser region, causing a decrease in the pressure. The pressure difference created would lead to migration of particles from the surrounding region to denser region, leading to further increase in the density and decrease in temperature and pressure. The cluster thus formed would continue to grow until it is arrested by some other mechanism like diffusion.

In this chapter we are interested in studying the formation of density waves in gravity-driven granular Poiseuille flow. The density waves in bounded granular flows has been studied by various authors [48, 72, 76, 80, 98]. A lattice-gas automaton model was used to study the formation of density waves in a vertical pipe [72]. It was found that both dissipation and roughness of the walls of the pipe were essential for the emergence of density waves and were observed only when the average density of the system was in a certain range. In an experimental measurement of granular material flowing down a capillary tube [76], density waves formed only at intermediate flow rates between a low density free fall regime and a high compactness slower flow. A study of granular flow through a narrow vertical pipe described using the Langevin equation [80] showed that above a critical particle density the homogeneous flow becomes unstable with respect to short-wave length perturbations. A linear stability of the equations of motion for granular particles through a vertical channel showed that base state was unstable to perturbations in the form of density waves [98]. Three different types of unstable modes were identified from the linear stability analysis. Further, these density waves were connected to a wave-hierarchy equation through a nonlinear analysis [91].

A molecular-dynamic simulation was performed to study the flow of granular particles in a gravity-driven vertical channel [48]. Two distinct types of density waves were identified : a S-shaped wave and a slug; the dynamics of large systems were found to be qualitatively different from those of small systems. The present study on density waves is an extension of the earlier work by Liss *et al.,* [48]. The density waves have been explored in greater detail by examining their structure in different density regimes. We perform a Fourier analysis of the density field using

FFT subroutine available in MATLAB, to quantify the modes of instability and analyse the temporal structures in the flow. Besides, we investigate the effect of wall-roughness on the density waves. It is shown that the density waves are sensitive to various control parameters : volume fraction (ν), coefficient of restitution (e_n) and the aspect ratios L/W and W/d. Different types of density waves over a range of the control parameters are summarised in a phase diagram.

A brief description of Fourier analysis of density field is provided in this paragraph. The simulation box is divided into $N_1 \times N_2$ cells to obtain density field in the form of a matrix at $N_1 \times N_2$ points. Note the subscripts $1, 2$ refers to x and y coordinate directions, respectively. The two dimensional FFT subroutine in MATLAB is used to find complex Fourier expansion coefficients, $\mathbf{X}$, and also the power spectra, $\mathbf{P}$ which is given by the following expression :

$$\mathbf{P} = \frac{2.\mathbf{X}.conj(\mathbf{X})}{(N_1 N_2)^2}$$

The power spectra is normalised by the size of matrix to remove its dependence on the mesh size. It is represented as a surface plot and the peaks appearing in plot are amplitudes corresponding to coefficients $|a_{x,y}|$ in the Fourier series $a_{x,y}\ exp\big[2\pi\ i\ ((k_x x/L) + (k_y y/W))\big]$. More information about the steps involved in computing the power spectrum could be obtained elsewhere [48].

5.1 Moderately dense flows

We begin our study by looking at the density waves in moderately dense flows. A time trace of the average kinetic energy of the particles is shown in Fig. 5.1, for $\nu = 0.31, e_n = 0.85, L/W = 2$ and $W/d = 31$. To analyse the temporal structures, consider the flow at different times instances, $t = 4, 50$ and 150, indicated by filled circles in Fig. 5.1. The power spectrum of the density field and the particle positions at these times are displayed in Fig. 5.2. Clearly, as the time progresses the density waves undergoe a transition from a plug, at small times, to a one-humped wave, at steady state. The power spectrum of a plug flow has a peak at $(k_x, k_y) = (0, 1)$ in Fig. 5.2 (a), while a one-humped wavy flow gives rise to an additional peak at $(k_x, k_y) = (1, 1)$ in Fig. 5.2 [(b),(c)]. Note that in Fig. 5.2 both the walls were assigned a same roughness value ($\beta_w = 0.6$). To study the effect of wall-roughness on density waves different values of roughness are assigned to the left wall and right wall. The power spectrum and particle positions are displayed in Fig. 5.3, for the right wall at $\beta_w = 0.9$ and left wall at $\beta_w = 0.1$. It is observed that the structures are shifted towards left wall since it is at a lower temperature compared to the right wall, Fig. 5.3. Also, the transition to a wavy structure is absent and a plug flow persists till a steady state is reached. So, the power spectrum contains a single a peak at $(k_x, k_y) = (0, 1)$ at all times.

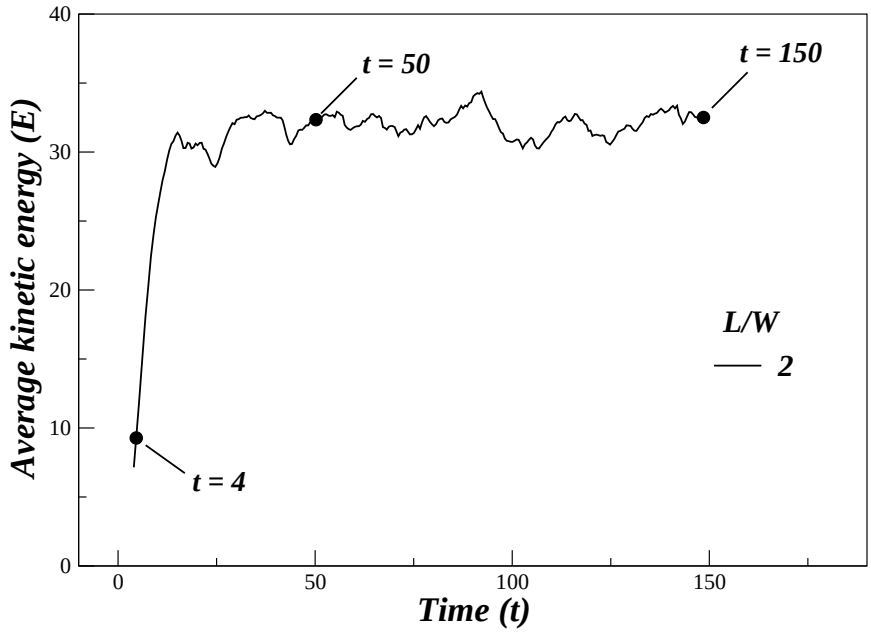

Figure 5.1: Time trace of average kinetic energy (E) of the particles for $N = 930$, $\nu = 0.31, e_n = 0.85, \beta_w = 0.6, L/W = 2$ and $W/d = 31$. The temporal structures of the flow at different times, $t = 4, 50$ and , indicated by circles, are shown in Fig. 5.2.

The power spectrum and particle configurations at a higher aspect ratio of $L/W = 8$ is shown in Figs. 5.4 and 5.5 for the walls at same roughness and at different roughness, respectively. Once again the structures are shifted towards the rougher (colder) wall, when the walls have different roughness, and in both the cases density waves make a transition from a plug flow, at small times, to a slug flow, at steady state. When t is small the power spectrum displays a peak at $(k_x, k_y) = (0, 1)$ indicating a plug flow and in the steady state an additional peak appears at $(k_x, k_y) = (1, 0)$ indicating a slug flow.

The results obtained for walls with same roughness are in good qualitative agreement with the results of Liss *et al* [48]. From the above observations it is apparent that the structure formation is affected due to the asymmetry in the wall-roughness. The steady state structures at different L/W and W/d aspect ratios and at $\nu = 0.31$ and $e_n = 0.85$ are summarised in a phase diagram in Fig. 5.6.

Further, to clearly demonstrate the effect of asymmetric wall-roughness, another set of plots for $W/d = 65$ and $L/W = 1, 2, 4$ are displayed in Fig. 5.7 [(a),(b),(c)]. With increasing L/W ratio, the steady state structure of the flow makes a transition from a $plug \rightarrow wave \rightarrow slug$. These results also confirm our earlier observations that the structures move towards rougher (colder) wall when the walls have different roughness.

To obtain a better picture of the effect of wall-roughness on density waves we fix the aspect ratio $W/d = 55$ and vary β_w symmetrically and asymmetrically over

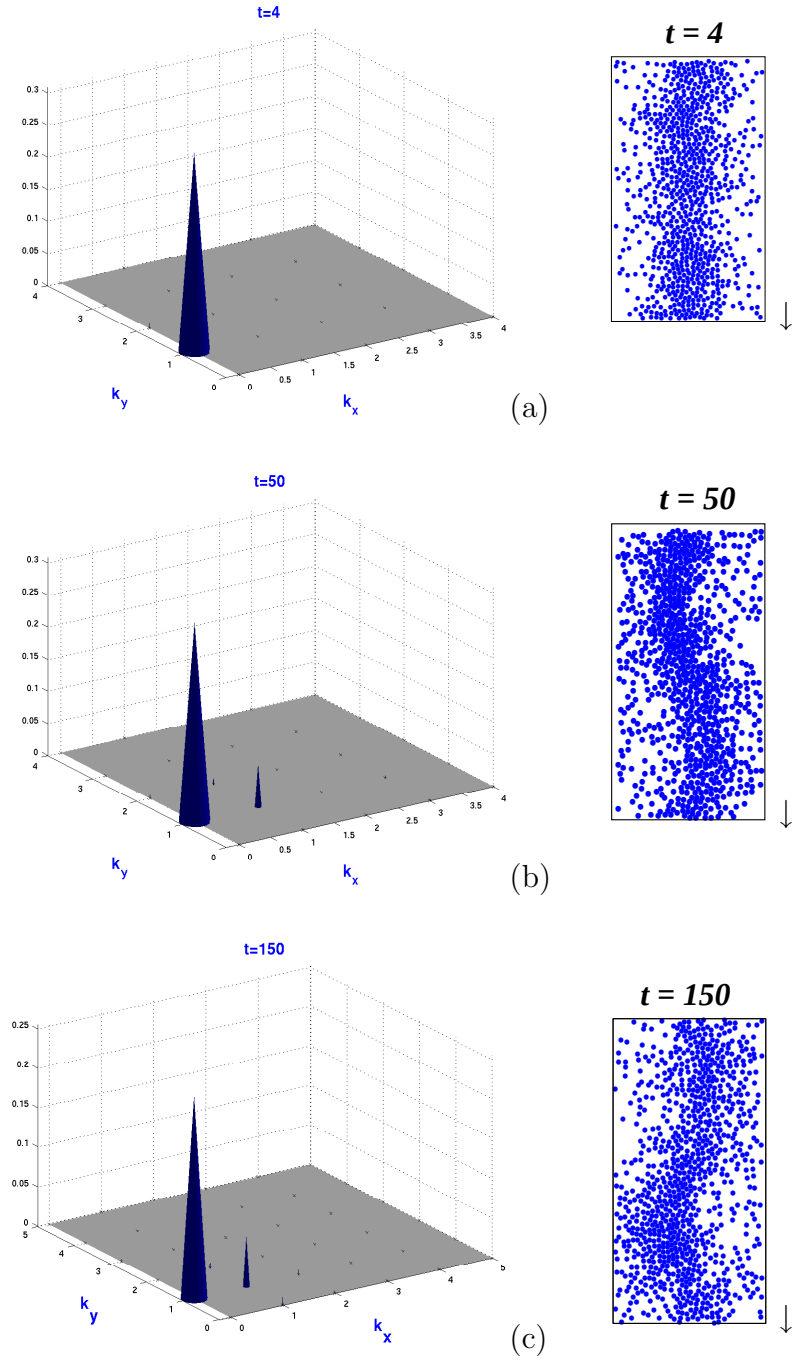

Figure 5.2: Power spectrum of density field (*left*) and particle positions (*right*) at different times. A transition from (a) a plug flow at $t = 4$ to a single humped wave in the steady at (b) $t = 50$ and (c) $t = 150$. The parameters are $N = 930$, $\nu = 0.31, e_n = 0.85, \beta_w = 0.6, L/W = 2$ and $W/d = 31$ for symmetric wall-roughness. The arrows at the bottom right corner of the plots on the right indicate the direction of the flow.

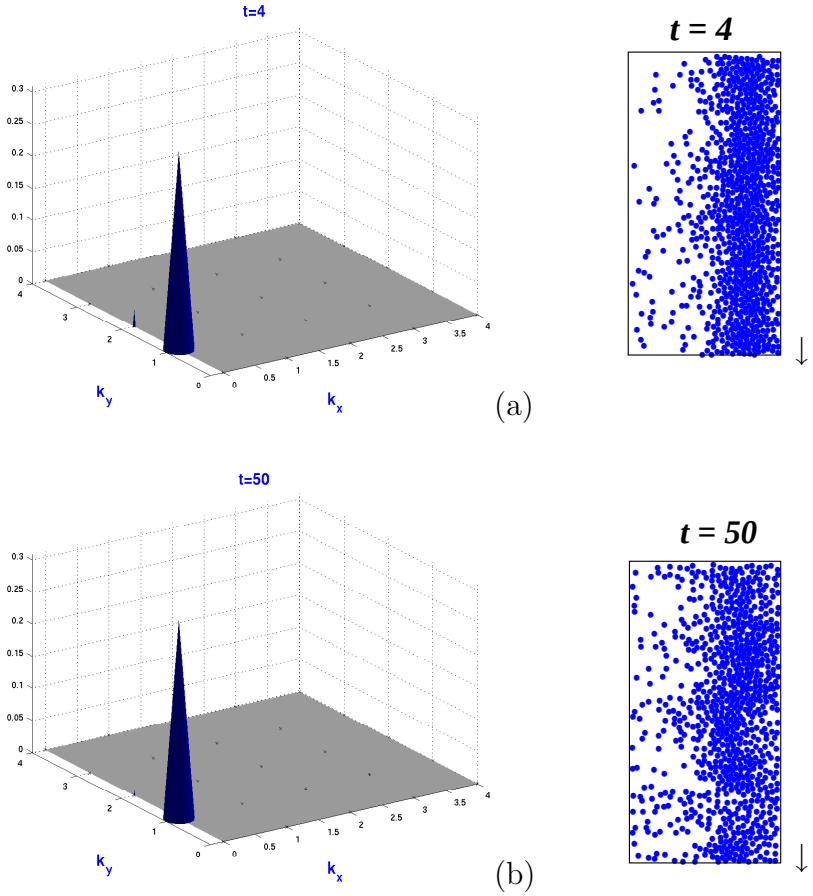

Figure 5.3: Power spectrum of density field ($left$) and particle positions ($right$) at different times. A transition from (a) a plug flow to (b) a slug is observed at $N = 930$, $\nu = 0.31, e_n = 0.85, \beta_w = 0.9, 0.1, L/W = 2$ and $W/d = 31$ for walls with asymmetric roughness. The arrows at the bottom right corner of the plots on the right indicate the direction of the flow.

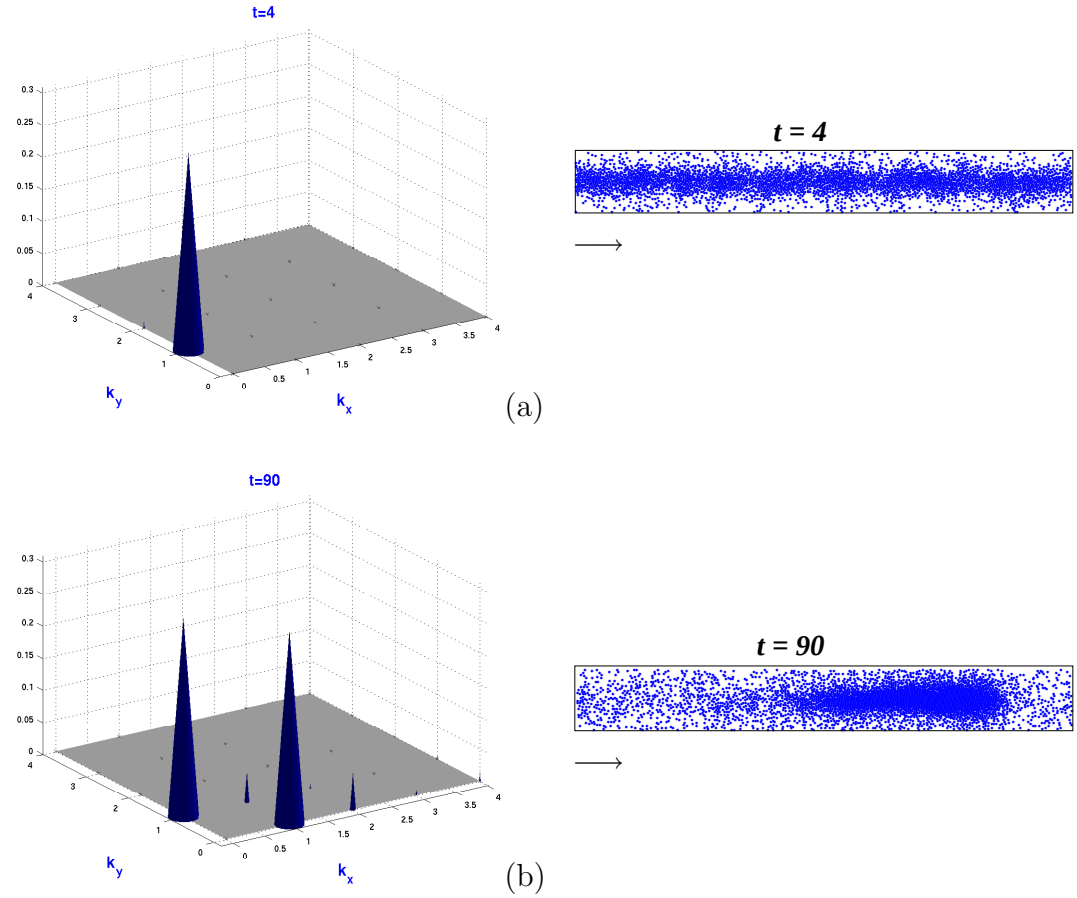

Figure 5.4: Power spectrum of density field ($left$) and particle positions ($right$) are shown at different times. A transition from (a) a plug flow at $t = 4$ to (b) a slug at $t = 90$ is observed when $N = 3450$, $\nu = 0.31, e_n = 0.85, \beta_w = 0.6, L/W = 8$ and $W/d = 31$ for symmetric wall-roughness. The arrows at the bottom left corner of the plots on the right indicate the direction of the flow.

a range of L/W ratio. The effect of varying β_w symmetrically is shown in the phase diagram Fig. 5.8, while the effect of asymmetric wall-roughness is shown in Fig. 5.9. The value of parameters used in these simulations are $\nu = 0.31$ and $e_n = 0.85$. These results clearly indicate that the steady state structure of the density waves are not greatly affected by wall-roughness.

5.2 Dense flows

We now look at the phase diagram for a relatively higher volume fraction of $\nu = 0.5$. The roughness of both walls are set $\beta_w = 0.9$. The phase diagrams corresponding to $e_n = 0.85$ and $e_n = 0.5$ are shown in Fig. 5.10 and Fig. 5.11, respectively. When the coefficient of restitution is $e_n = 0.85$, Fig. 5.10, a plug and an asymmetric

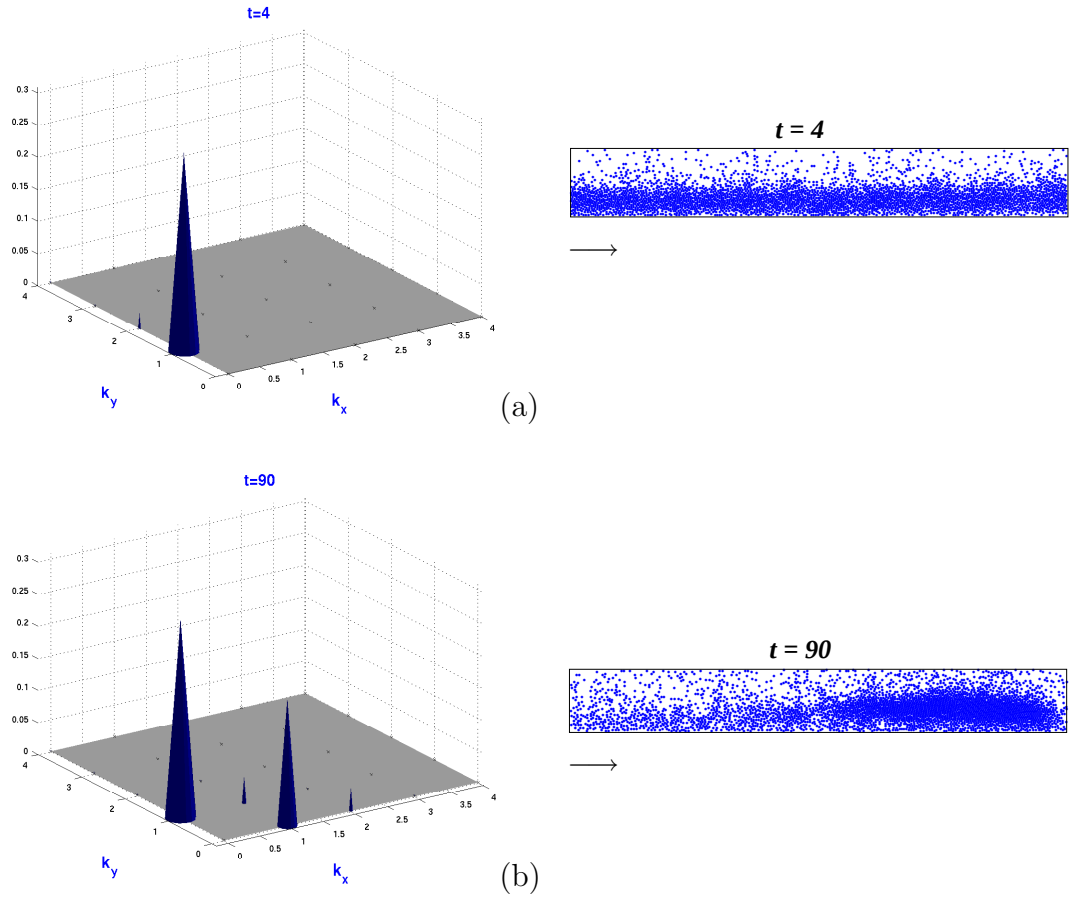

Figure 5.5: Power spectrum of density field (*left*) and particle positions (*right*) are shown at different times. A transition from (a) a plug flow to (b) a slug is observed at $N = 3450$, $\nu = 0.31, e_n = 0.85, \beta_w = 0.9, 0.1, L/W = 8$ and $W/d = 31$ for walls with asymmetric roughness. The arrows at the bottom left corner of the plots on the right indicate the direction of the flow.

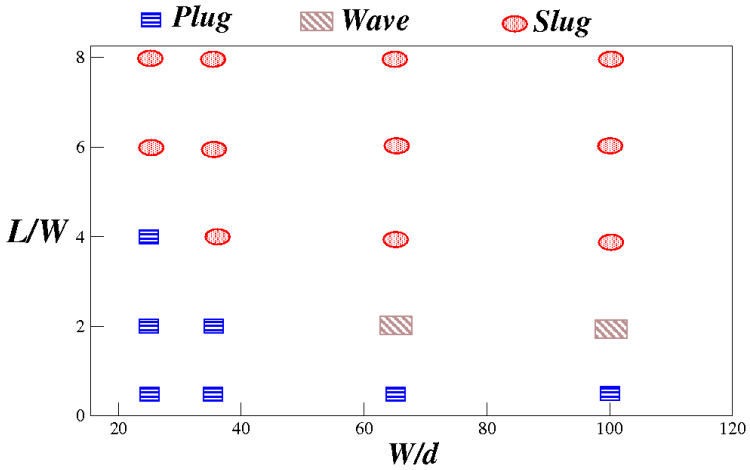

Figure 5.6: Phase diagram of steady state structures at $\nu = 0.31, e_n = 0.85$ and different L/W and W/d aspect ratios, for wall at different roughness is summarised. The right wall has roughness of $\beta_w = 0.9$ and left wall has a roughness of $\beta_w = 0.1$.

wave (sinuous mode) are observed over a wide range of L/W ratio. At large W/d or L/W ratio, a new symmetric wave (varicose mode) emerges, which is evident from the instantaneous positions of the particles in Fig. 5.13 and Fig. 5.14. In Fig. 5.13, $W/d = 70$ and $L/W = 2$, whereas in Fig. 5.14, $W/d = 70$ and $L/W = 3$. For the ease of understanding, particle positions at two different instances are presented. A time trace of the average kinetic energy of the particles is displayed in Fig. 5.12. The filled circles in Fig. 5.12 indicate the time instances at which the particle positions in Fig. 5.13 and Fig. 5.14 were captured. The region marked by the dark continuous lines in Fig. 5.13 and Fig. 5.14 indicate the dislocations in the struture, that arise due to the emergence of force chains. These force chains become prominent as the system size increases and at high densities. When the above set of simulations were carried out at a coefficient of restitution of $e_n = 0.50$, the varicose mode disappeared and the density waves display a transition from a plug to a wave and then a slug with increasing L/W ratio for $\nu = 0.5$, as shown in Fig. 5.11.

We include a set of plots showing the particle positions for $W/d = 55$ and $e_n = 0.85$ and $W/d = 50$ and $e_n = 0.50$ at various L/W ratios, to present a clear picture of the structure of the density waves. The plots on the left-side in Fig. 5.15 shows the instantaneous particle positions for $e_n = 0.85$ for $L/W = 1, 3, 6$, while the plots on the right-side shows the instantaneous particle positions for $e_n = 0.85$ for the same L/W ratios.

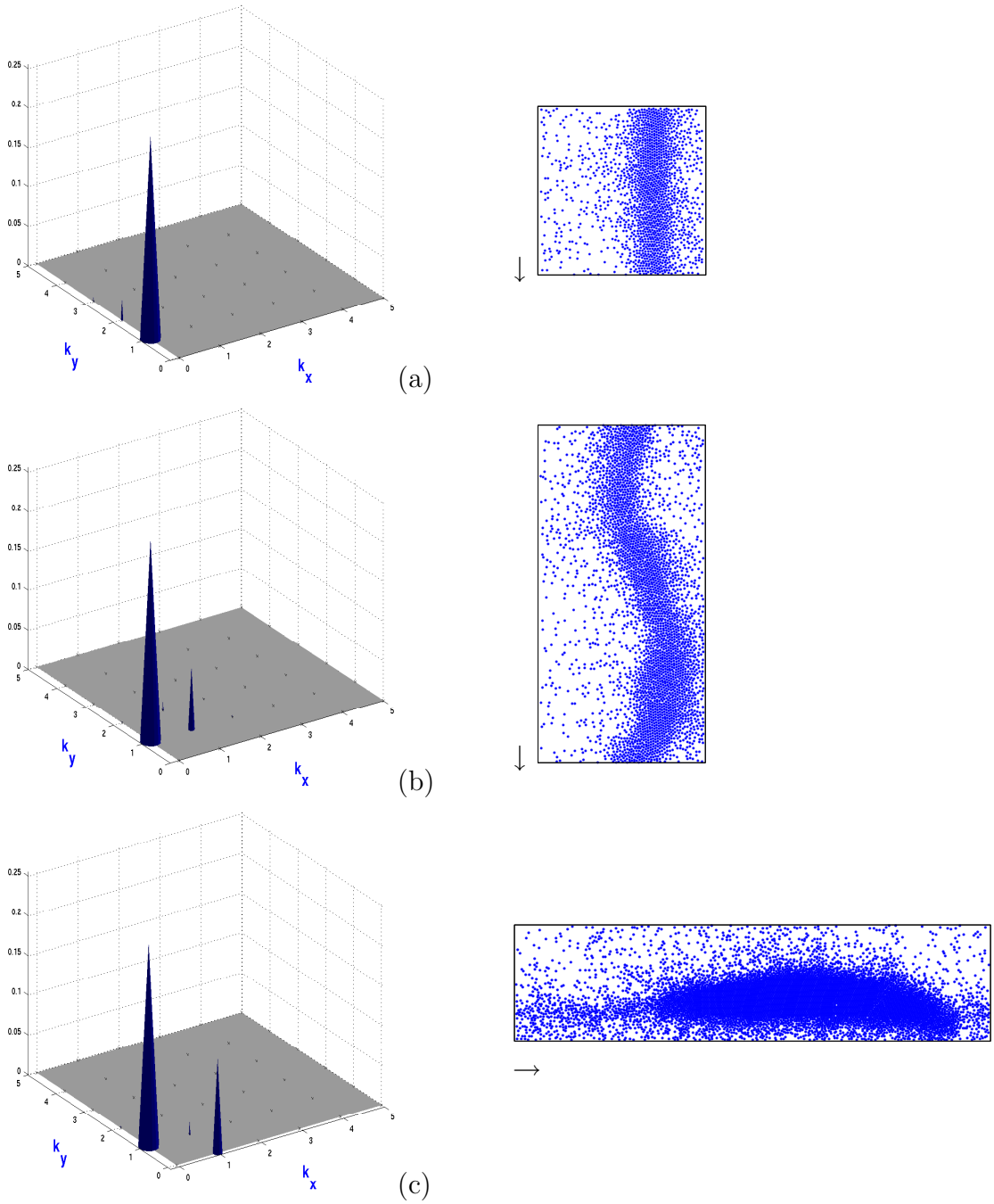

Figure 5.7: Power spectrum of density field (*left*) and particle positions (*right*) for $\nu = 0.31, e_n = 0.85, W/d = 65$ and (a) $N = 1620$ and $L/W = 1$ (b) $N = 3355$ and $L/W = 2$ and (c) $N = 6660$ and $L/W = 4$. The roughness of right wall is $\beta_w = 0.1$ and left wall is $\beta_w = 0.9$.

5.3 Dilute flows

We study the cluster formation in dilute flows by setting the volume fraction at $\nu = 0.05$ and coefficient of restitution at $e_n = 0.5$. Generally, the formation of clusters

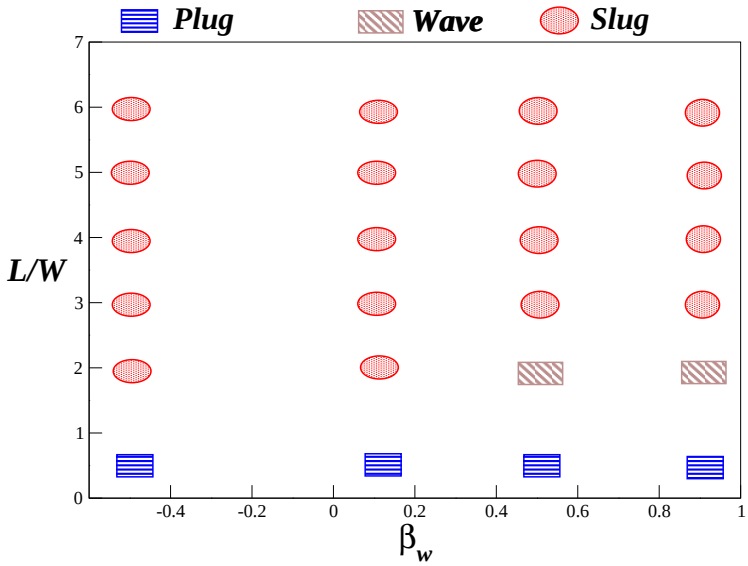

Figure 5.8: Phase diagram of steady state structures at $\nu = 0.31, e_n = 0.85$, $W/d = 55$ and different L/W ratios and wall-roughness. Both the walls are assigned same value of roughness.

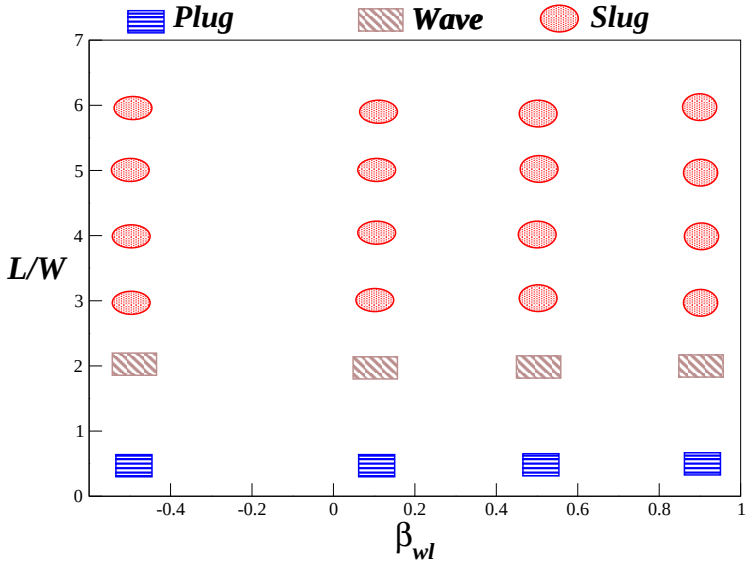

Figure 5.9: Phase diagram of steady state structures at $\nu = 0.31, e_n = 0.85$ $W/d = 55$ and different L/W ratios and wall-roughness is shown. The roughness of right wall is set at $\beta_{wr} = 0.9$ and roughness of the left wall β_{wl} is varied.

is weak in dilute flows, so in order to enhance their growth we increase the system size by taking large L/W aspect ratios. Even at large system sizes, $N \sim 25000$,

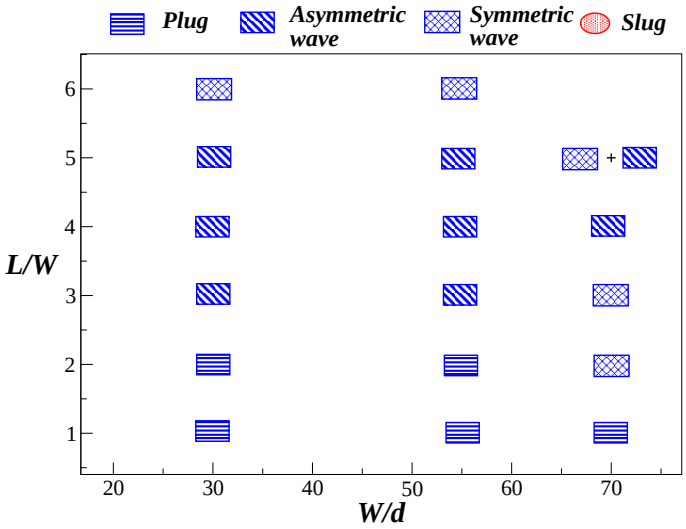

Figure 5.10: Phase diagram of steady state structures at $\nu = 0.50, e_n = 0.85$ $\beta_w = 0.9$ and different L/W and W/d ratios. Both the walls are assigned same value of roughness.

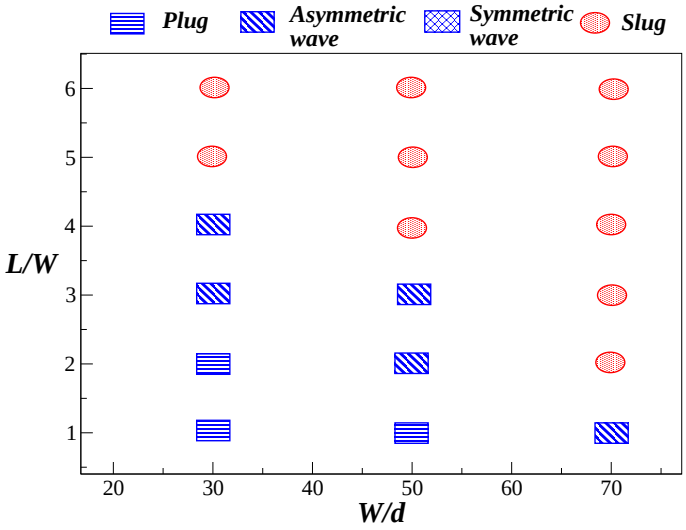

Figure 5.11: Phase diagram of steady state structures at $\nu = 0.50, e_n = 0.50$ $\beta_w = 0.9$ and different L/W and W/d ratios. Both the walls are assigned same value of roughness.

the dynamics of density waves is poor compared to that at moderately dense and dense flows. Some of these results are presented in the following paragraphs.

In the Figs. 5.16 (a) & (b) the power spectrum density (left), P, and instantaneous particle positions (right) for $W/d = 30$ at $L/W = 50$ and $L/W = 70$, respectively, are shown. Similar plots at $W/d = 50$ and $W/d = 70$ are shown in Fig. 5.17 and Fig. 5.18, respectively. In all the power spectrum plots the dominant peaks along k_x- axis indicate the presence of clumps of particles along the $x-$ direction, which is also evident from the plots of particle positions. The distin-

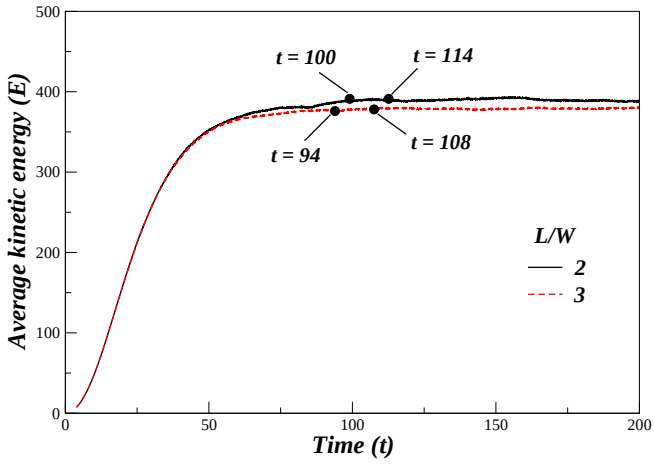

Figure 5.12: Time trace of average kinetic energy (E) of the particles for $\nu = 0.5, e_n = 0.85, \beta_w = 0.9, W/d = 70$ and $L/W = 2, 3$. The temporal structure of the flow at the time instances indicated by circles are shown in Fig. 5.13 and Fig. 5.14.

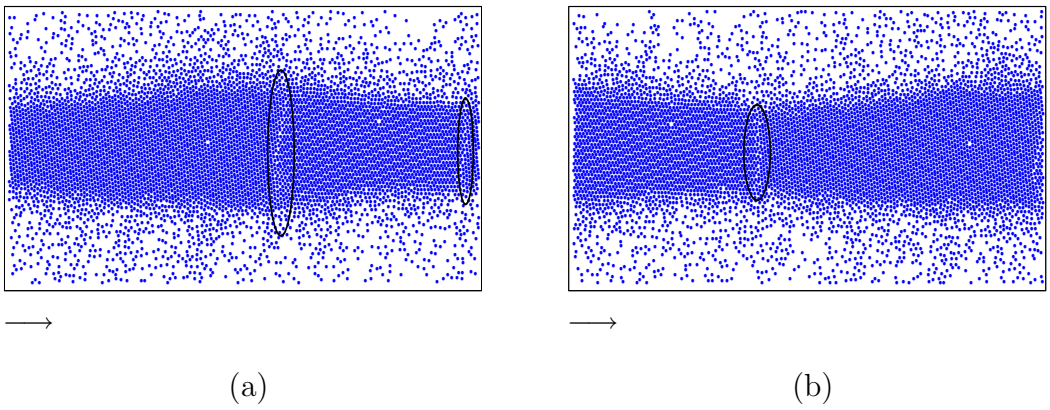

(a) (b)

Figure 5.13: Instantaneous positions of the particles at two different times, (a) t=100 and (b) t=114. The parameter values are $N = 6240$, $\nu = 0.5$, $e_n = 0.85$, $\beta_w = 0.9$, $W/d = 70$ and $L/W = 2$. The arrows at the bottom left corner indicate the direction of the flow.

guishing feature between a clump and a slug is that the size of a slug is comparable to the simulation box, whereas a clump is relatively much smaller.

From our previous observations, Fig. 5.8 and Fig. 5.10, it is apparent that a plug and a wave are obtained when $L/W \sim 1$. Motivated by these observations, we perform simulations at $\nu = 0.05$, $e_n = 0.5$, $W/d = 150$ and $L/W = 1$ and $\nu = 0.05$, $e_n = 0.9$, $W/d = 300$ and $L/W = 1$. These results are presented in Fig. 5.19 and Fig. 5.20. At $e_n = 0.5$, the plot of particle positions in Fig. 5.19 (a) shows a clump, while the power spectrum also has a peak corresponding to a clump along with another dominant peak along k_x- axis. When e_n is increased to $e_n = 0.99$, Fig. 5.19 (b), the plot of particle positions do not indicate any structure,

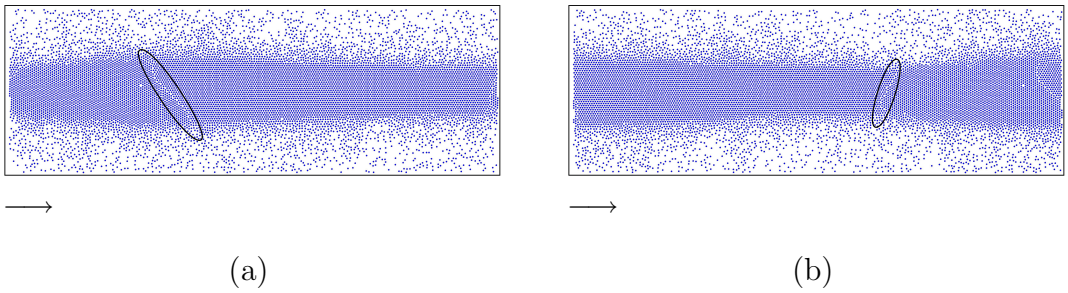

(a) (b)

Figure 5.14: Instantaneous positions of the particles at two different times, (a) t=94 and (b) t=108. The parameter values are $N = 9360$ $\nu = 0.5$, $e_n = 0.85$, $\beta_w = 0.9$, $W/d = 70$ and $L/W = 3$.

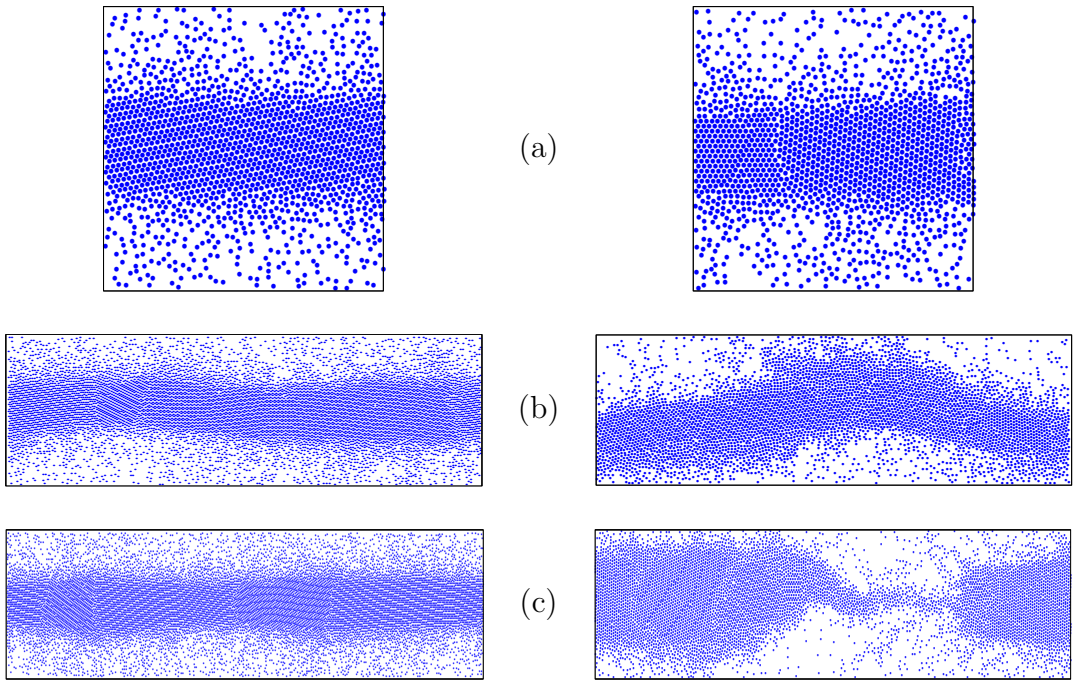

Figure 5.15: Instantaneous particle positions for $W/d = 55$ and $e_n = 0.85$ (left) and $W/d = 50$ and $e_n = 0.5$ (right) at different L/W ratios : (a) L/W=1, (b) L/W=3, (c) L/W=6. Note that the plots are not to scale.

while the power spectrum contains random peaks indicating the noise. Since the power spectrum displays relative magnitudes of the peaks, a noise in the system is displayed as random peaks in the spectrum. Increasing W/d to 300, the clumps reappear as in Fig. 5.20.

In an earlier chapter on velocity distribution, it was observed that wall roughness has a significant effect on the local velocity distribution at all points in a dilute flow. We would like to study the way wall-roughness affects the clustering of particles in dilute flows. In Fig. 5.21 the effect of asymmetric wall-roughness on the

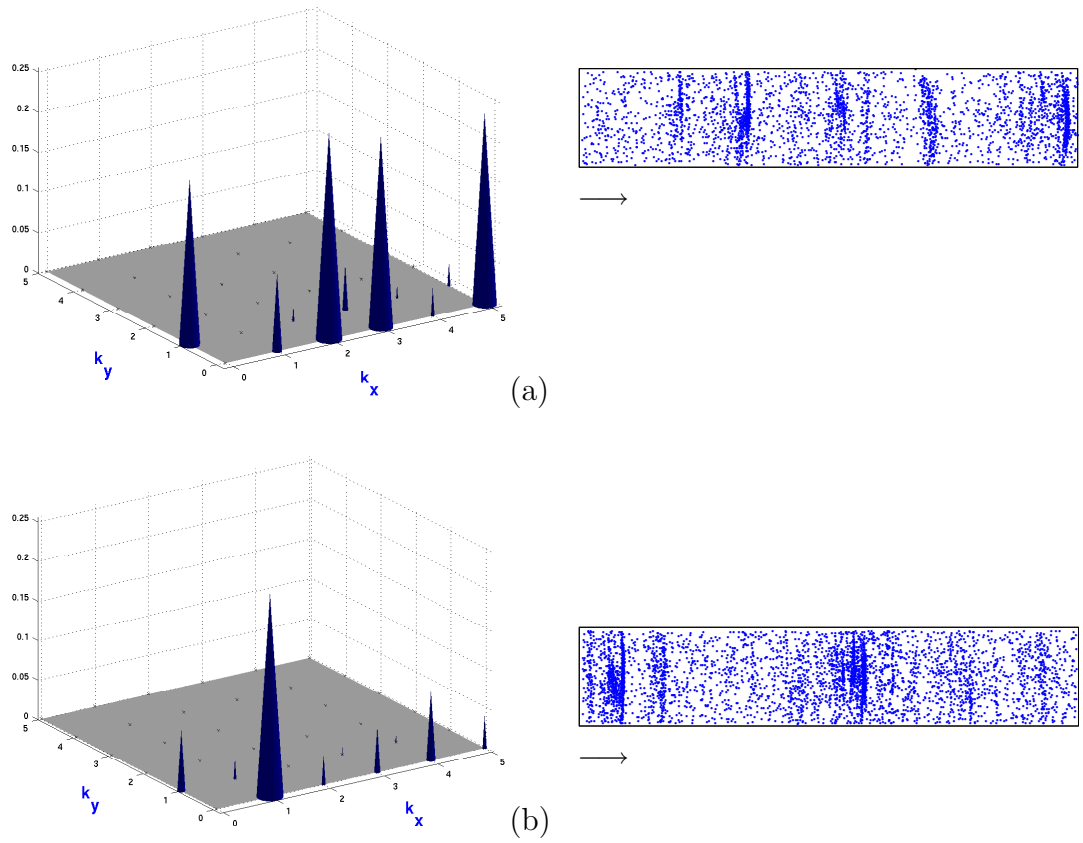

Figure 5.16: Power spectrum of density fluctuations (left) and particle positions (right) for $\nu = 0.05, e_n = 0.5, \beta_w = 0.9$ and $W/d = 30$ at (a) $N = 2900$, $L/W = 50$ and (b) $N = 4010$, $L/W = 70$. The dominant peaks along k_x- axis in the power spectrum indicates the presence of clumps along $x-$ direction. Note that the panel showing particle position is not to scale. The arrows at the bottom left corner of the plots on the right indicate the direction of the flow.

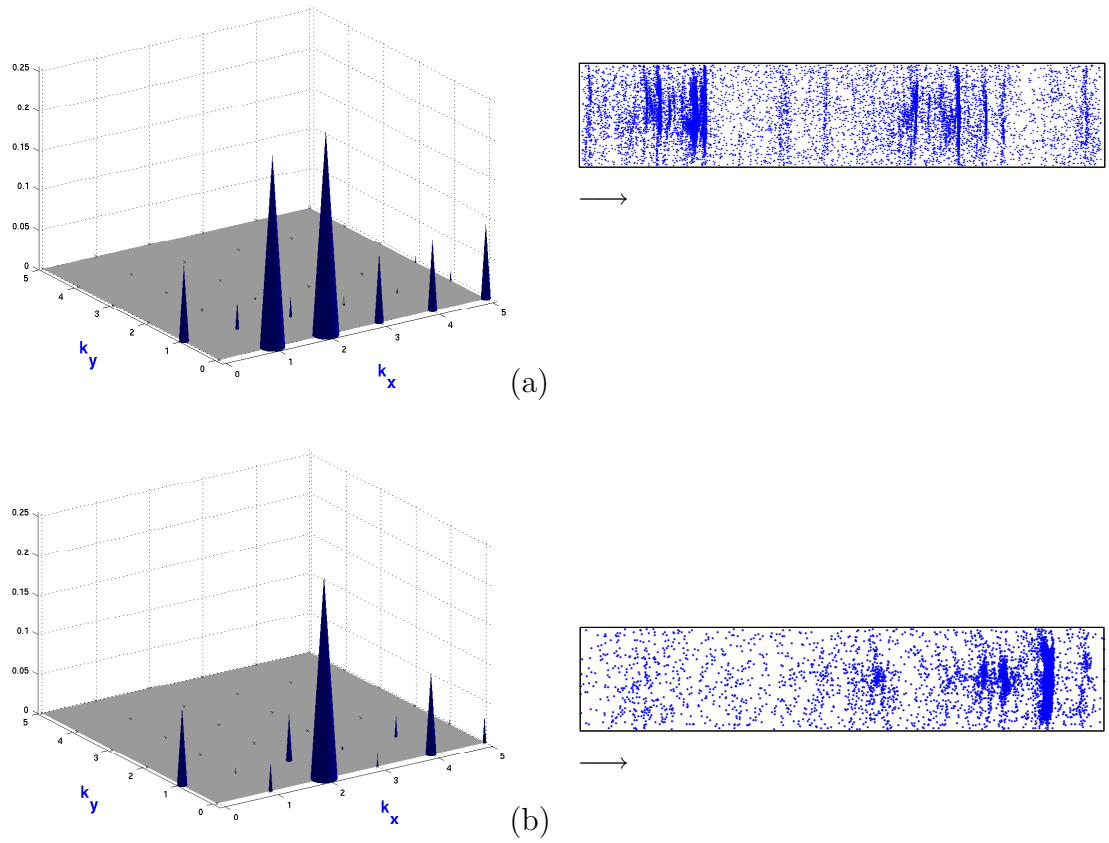

Figure 5.17: Power spectrum of density fluctuations (left) and particle positions (right) for $\nu = 0.05, e_n = 0.5, \beta_w = 0.9$ and $W/d = 50$ at (a) $N = 7960$, $L/W = 50$ and (b) $N = 11140$, $L/W = 70$. Note that the panel showing particle position is not to scale.

density fluctuations is shown. The right wall is assigned a roughness of $\beta_w = 0.9$ and left wall is assigned a roughness of $\beta_w = 0.1$. Though the clumps of particles are shifted towards the rougher (colder) wall (panels on the right in Fig. 5.21), the power spectrum remains qualitatively unchanged with dominant peaks along k_x- axis. A summary of the structure formation in the range $W/d = 30 - 70$ and $L/W = 25 - 125$, for the case of symmetric wall-roughness ($\beta_w = 0.9$), is shown in the phase diagram Fig. 5.22.

5.4 Summary

We saw that the dynamics of density waves in gravity-driven Poiseuille flow is rich in the moderately dense and dense regimes. At moderate densities density waves have three different structures : a plug, wave and slug. The range of L/W values over which a plug/ wave/ slug exists depends on the aspect ratio W/d, Fig. 5.8 and Fig. 5.10. Generally a transition from a plug to a wave at moderate L/W and then

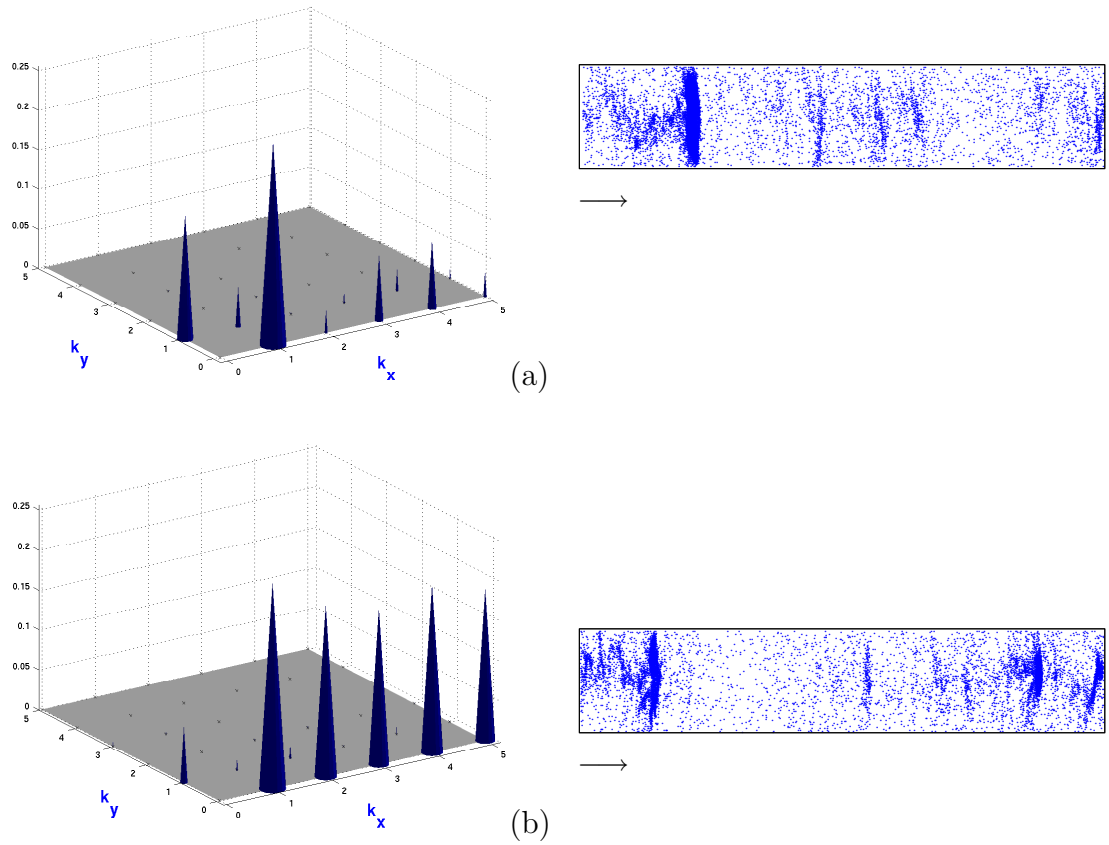

Figure 5.18: Power spectrum of density fluctuations (left) and particle positions (right) for $\nu = 0.05, e_n = 0.5, \beta_w = 0.9$ and $W/d = 70$ at (a) $N = 11140$, $L/W = 50$ and (b) $N = 22000$, $L/W = 70$. Note that the panel showing particle position is not to scale.

from a wave to slug at large L/W is observed. In dense flows, at moderate and high values of coefficient of restitution ($e_n \sim 0.8$), a new symmetric wave mode (varicose mode) emerges. Whereas at lower values of coefficient of restitution ($e_n = 0.5$) the density waves undergo a transition from plug-wave-slug with increasing L/W aspect ratio. Finally, in the dilute limit the particles form small clumps with no distinct features over a large range of L/W and W/d ratios. The effect of wall-roughness on structure formation was studied by varying the roughness of the walls symmetrically and asymmetrically. In the case of symmetric roughness the effect on density waves was negligible, whereas in the case of asymmetric roughness the density waves were pushed towards the smooth (cold) wall.

A qualitative picture of different steady state structures is presented as a three dimensional phase diagram in Fig. 5.23. The $(L/W - W/d)$ plane represents the limit $\nu \to 0$ *i.e.,* dilute limit, the $(L/W - \nu)$ plane represents the limit $W/d \to 0$ and the $(\nu - W/d)$ plane represents the limit $L/W \to 0$. We saw that in the dilute limit no distinct steady state structures were found except the clump formation, so $(L/W - W/d)$ plane is labelled as clump. At small values of $L/W \to 0$ or $W/d \to 0$

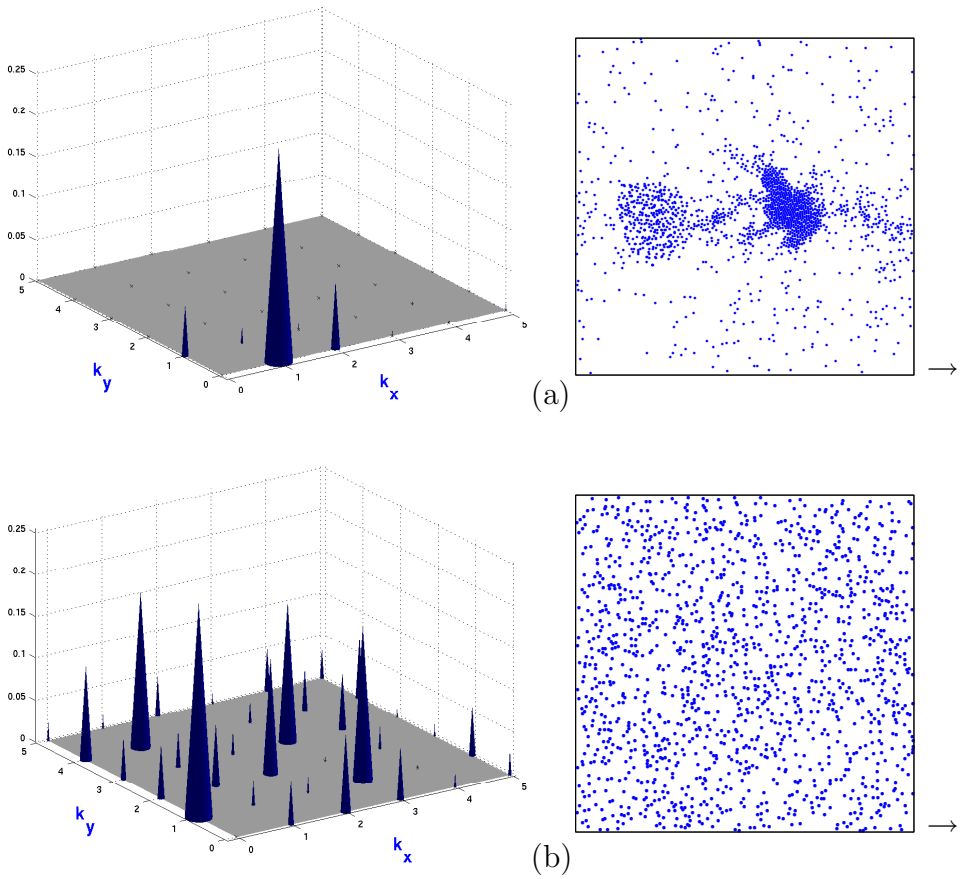

Figure 5.19: Power spectrum density of density fluctuations (left) and instantaneous particle positions (right) at (a) $e_n = 0.5$ and (b) $e_n = 0.99$ for $N = 1440$, $\nu = 0.05, \beta_w = 0.9$, $W/d = 150$ and $L/W = 1$.

a plug was observed, so the $(\nu - W/d)$ and $(L/W - W/d)$ planes are labelled as plug. The section considered in Fig. 5.23 shows the structures at intermediate densities that display a transition from $plug \rightarrow wave \rightarrow slug$ with increasing L/W or W/d ratio.

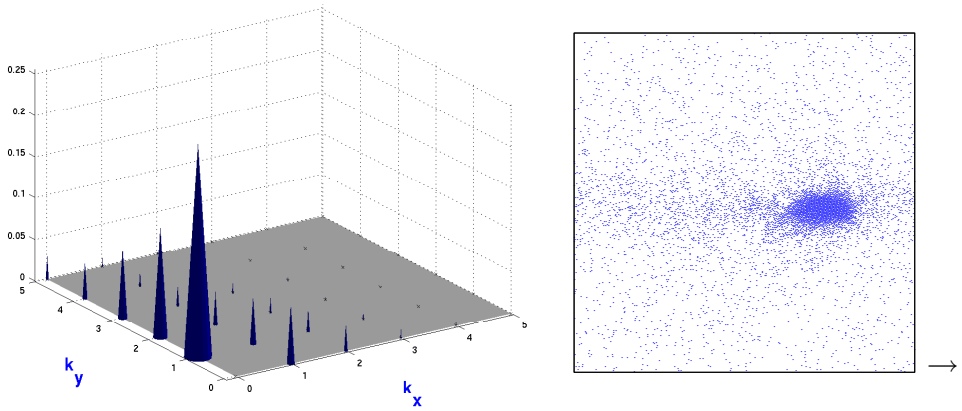

Figure 5.20: Power spectrum density of density fluctuations (left) and instantaneous particle positions (right) for $N = 5700$, $\nu = 0.05, e_n = 0.9, \beta_w = 0.9$, $W/d = 300$ and $L/W = 1$.

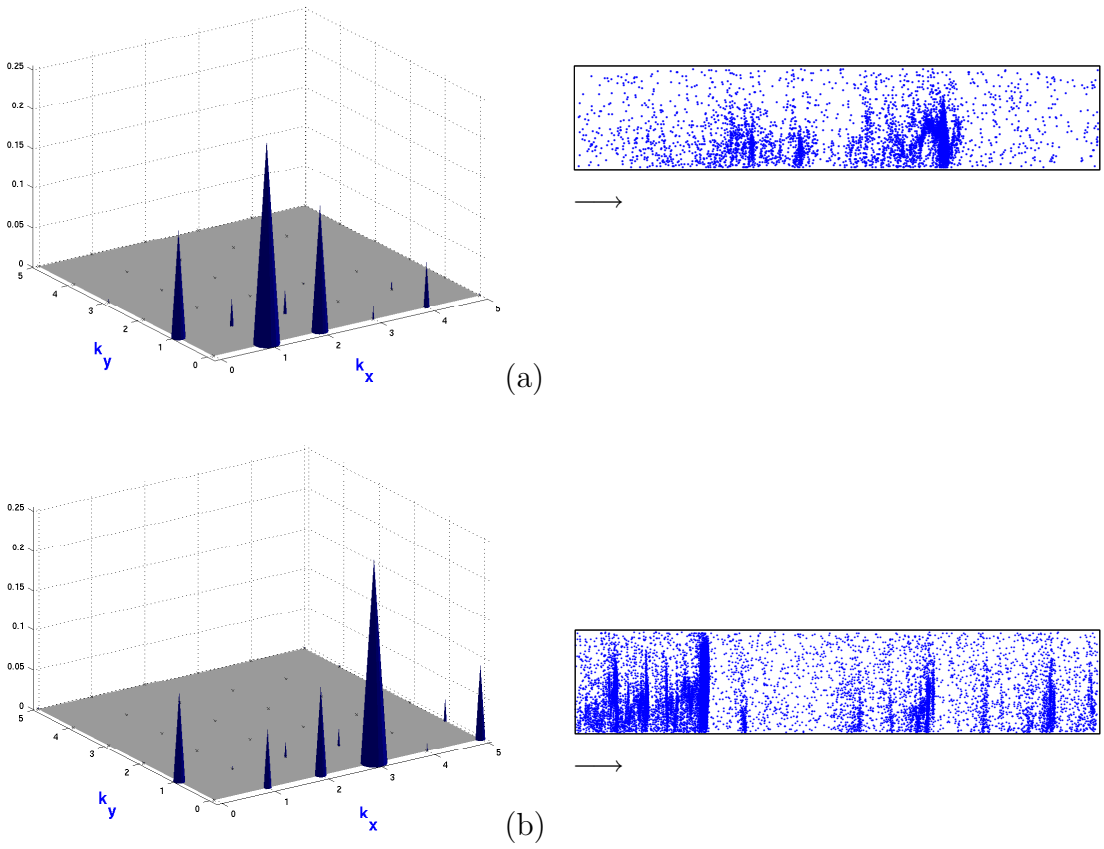

Figure 5.21: Power spectrum density of density fluctuations (left) and instantaneous particle positions (right) at $\nu = 0.05$ and $e_n = 0.5$ for $W/d = 50$ at (a) $N = 7960$, $L/W = 50$ and (b) $N = 11140$, $L/W = 70$. The roughness of right wall is set at $\beta_w = 0.9$ and left wall at $\beta_w = 0.1$.

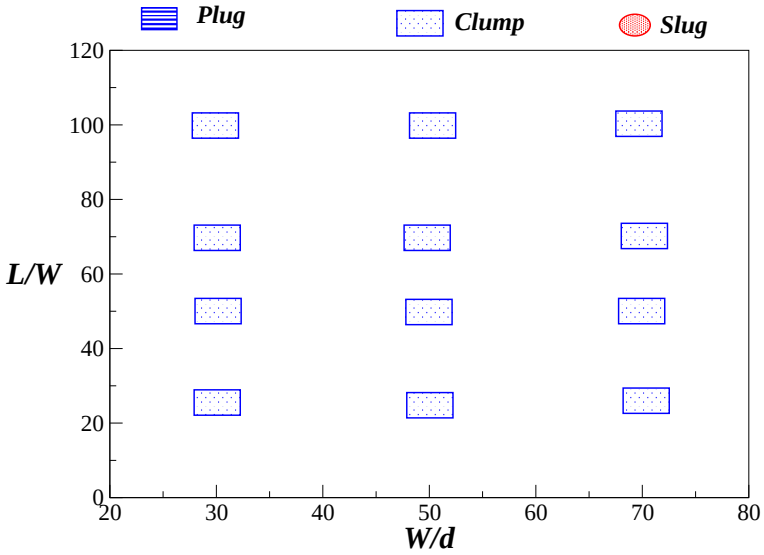

Figure 5.22: Phase diagram of steady state structures at $\nu = 0.05, e_n = 0.50$ $\beta_w = 0.9$ and different L/W and W/d ratios. Both the walls are assigned same value of roughness.

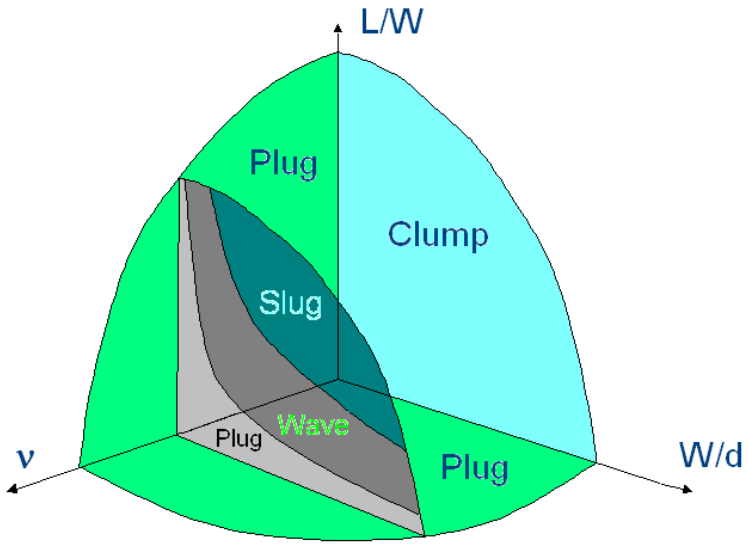

Figure 5.23: A qualitative phase diagram of steady state structures in granular Poiseuille flow.

CHAPTER 6

SUMMARY AND OUTLOOK

The granular Poiseuille flow (GPF) has been simulated using the molecular dynamics technique. Since the particles are modelled as smooth hard disks, the simulations are carried out in two dimensions. An even-driven algorithm proposed by Lubachevsky [51] is used for simlation. The losses due to particle-particle collisions and particle-wall collisions are characterised by normal restitution coefficient (e_n) and tangential restitution coefficient (β_w), respectively. Various aspects of the GPF : local velocity distributions, rheological quantities such as pressure, shear stress, viscosity and first normal stress difference, velocity and temperature boundary conditions and density waves are studied over a range of control paramaters.

The local distribution of the fluctuating velocities in the x-direction and y-directions, denoted as $P(u_x)$ and $P(u_y)$, respectively, remain Gaussian over a wide range of densities ($\nu \leq 0.85$) for *smooth* walls and nearly elastic collisions ($e_n \rightarrow 1$). The kurtosis of the distributions are computed to quantify their deviation from a Gaussian and its magnitude is found to be close to that of a Gaussian distribution. Increasing the wall roughness leads to interesting *asymmetric* distribution function for u_x, with a peak for negative velocities in the near wall region. In dilute flows the effect of wall roughness is felt at all points across the channel, whereas in dense flows the distribution (both $P(u_x)$ & $P(u_y)$) only in the near wall region is affected. On the other hand, the effects of dissipation due to particle-particle on the local velocity distributions have been studied in different density regimes. For moderately dense flows with smooth walls, the local velocity distributions are asymmetric except at the walls, where they remain Gaussian. Further, the inhomogenities due to the formation of density waves are found to enhance the asymmetry of the velocity distributions. At high densities ($\nu > 0.50$), an increase in dissipation is accompanied with the formation of a plug at the centre of the channel and the flow undergoes a transition from a liquid-like state to a crystal-like state. The tails of the velocity distributions (both $P(u_x)$ & $P(u_y)$) near the centerline of the channel display a transition from Gaussian distribution at $e_n \sim 1$ to a power-law distribution at higher dissipation. The distributions outside the plug region *i.e.,* in high shear region, are asymmetric owing to the presence of strong inhomogenities and close to a Gaussian in the near-wall region for smooth walls. A change in the wall-roughness affects the distributions only in the near-wall region and the dynamics inside the plug region are relatively unaffected. The tails of $P(u_x)$ and $P(u_y)$ distributions develop asymmetry with increasing dissipation and is characterised by skewness of the distribution. The magnitude of skewness of $P(u_x)$ and $P(u_y)$ is maximum in the region where the shear rate is high and minimum in

the plug region where the shear rate is negligible/small. The skewness of $P(u_x)$ distribution is negative in all the bins, whereas the skewness for $P(u_y)$ distribution in changes sign due to the underlying asymmetry of u_y-velocity. Various correlation functions : pair correlation function, spatial velocity correlation functions and autocorrelation functions, are studied to gain a better understanding of the effects of dissipation on the velocity distributions in the dense limit. Within the plug region, the density correlations and the spatial velocity correlations are enhanced due to dissipation, leading to deviation of tails of the velocity distribution (both $P(u_x)$ & $P(u_y)$) from a Gaussian to power-law. The flow outside the plug region is in a gaseous state with negligible density and velocity correlations. It is observed that the velocity autocorrelation function of the streamwise velocity decays to zero almost immediately in the both the plug and the shear regions, indicating that temporal correlations do not play any significant role in determining the behaviour of velocity distributions in the dense region.

The rheological quantities such as pressure, shear stress, viscosity and first normal stress difference of granular Poiseuille flow have been computed at various densities. In the quasi-elastic limit, the simulation results agree well with expressions derived from kinetic theory by Jenkins & Richman [41] for circular disks. As the degree of dissipation increases the simulation results deviate from the analytical results for quasi-elastic limit. The first normal stress difference ($\mathcal{N}_1$) is negligible in the quasi-elastic limit, but displays non-monotonicity behaviour with the volume fraction at higher dissipation. Near the center-line of the channel, $\mathcal{N}_1$ increases from zero in the dilute limit, reaches a maximum at some intermediate density and then decreases, attaining a negative value beyond a critical density. A closer look at kinetic ($\mathcal{N}_1^k$) and collisional ($\mathcal{N}_1^c$) components of $\mathcal{N}_1$ reveals that $\mathcal{N}_1$ at large densities is dictated by the behaviour of its collisional component ($\mathcal{N}_1^c$), which reverses sign beyond a certain volume fraction due to the structural re-organisaton of particles. The microstructural origin of the sign-reversal of $\mathcal{N}_1$ in GPF appears to be the same as in the sheared granular flow of Alam & Luding [1]. Further, a phase diagram depicting the zeros of first normal stress difference ($\mathcal{N}_1$) and its collisional components shows that the zero lines of $\mathcal{N}_1$ and $\mathcal{N}_1^c$ coincide with each other at lower e_n and deviate at higher e_n, with the $\mathcal{N}_1^c$ attaining a zero value at a lower volume fraction compared to $\mathcal{N}_1$.

The simulation results predict that the slip velocity varies as $\frac{U_w}{U_0} \sim Kn^{\alpha}$, over the range $Kn \sim (1.1 - 0.02)$ and $e_n \sim (0.99 - 0.8)$, with an exponent $\alpha \sim (0.55 - 0.78)$. A similar power-law dependence of Knudsen number and slip velocity on volume fraction is also observed for $\nu \sim (0.015 - 0.4)$ and $e_n > 0.7$. The exponent for the $(Kn - \nu)$ relation is $\alpha \sim (-0.98 - -0.82)$ and that for $(\frac{U_w}{U_0} - \nu)$ relation is $\alpha \sim (-0.63 - -0.50)$. In addition, the velocity gradient near the wall varies as a positive power of volume fraction over the range $e_n \sim (0.99 - 0.8)$ and $\nu \sim (0.005 - 0.5)$, with an exponent $\alpha = 0.273$ and it varies as a negative power of the Knudsen number over the range the $(Kn \sim 0.001 - 3)$ and $e_n \sim (1 - 0.8)$, with an

exponent $\alpha = -0.212$. Furthermore, the simulations predict the average velocity to be constant at very low Knudsen number ($Kn < 0.005$) and decreases rapidly with further increase in the Knudsen number. The wall-temperature (T_w) and the temperature gradient $\left[\left(\frac{\partial T}{\partial y}\right)_w\right]$ display a non-monotonic variation with volume fraction. On the other hand, the variation of wall-temperature is nearly linear at high Kn, while the temperature gradient decreases rapdily at low and moderate Kn and approaches nearly a constant value at higher Kn.

The temporal evolution and steady structure of density waves have been invesitgated using the FFT subroutine in MATLAB. At moderate densities, density waves have three different structures : a plug, wave and slug. The range of L/W values over which different structures exist depends on the aspect ratio W/d. Generally, the density waves undergo a transition from a plug to wave and to slug with increasing L/W ratio. In dense flows, at moderate and high value of coefficient of restitution ($e_n > 0.8$) a new symmetric wave mode (varicose mode) emerges. Otherwise, at lower values of e_n ($= 0.5$) the density waves display a transition from plug-wave-slug with increasing L/W ratio. In the dilute limit, the particles form small clumps with no distinct features over a large range of L/W and W/d ratios. Further, the effect of wall roughness is studied by varying the wall-roughness symmetrically and asymmetrically. In the case of symmetric wall-roughness, the effect on density waves is negligible, whereas in the case of asymmetric wall-roughness the density waves are pushed towards the smooth (cold) wall but the effect on the structure of density waves is small.

The code developed for simulating GPF in two dimensions can be extended to perform simulations in three dimensions. It is observed that certain characteristics of velocity distributions obtained from the present simulation are in variance with the experimental results of Ref. [63] that were carried out in the dense 'quasi-static' regime. A more realistic collision model that includes Coulomb friction, particle spin and a velocity dependent restitution coefficient may be helpful in making a direct comparison with the experimental results. The implementation of such a collision model should be an easy task and it is likely to yield more meaningful and interesting results.

Acknowledgments

I am grateful to my advisor Dr. Meheboob Alam for suggesting me a variety of problems for the thesis and for his guidance during the course of my work. I appreciate his enthusiasm in sharing ideas and his encouragement to explore different aspects of granular materials that greatly helped me in developing good perspectives about the subject in a short duration.

I would like to thank the Chairman of Engineering Mehchanics Unit (EMU) Prof. Roddam Narasimha and all the faculty members in EMU. Prof. Rama Govindarajan was extremely supportive of me during the intial phase of my stay at JNCASR and I would like to thank her for all the support.

I would like make a special mention of Prof. Fazle Hussain, whom I met during the IUTAM symposium in Bangalore. Though my meeting with him was for a brief period, it influenced me in a very fundamental way. He taught me how to choose a problem and what should be focus of a investigation. I want to thank him for that brief meeting.

I am indebted to Antina for her company. Her independent ideas and outlook towards science and life in general inspired me to refine my own opinions and attitude. I would like to thank Kaushik for his friendship. Be it science or any other subject, he was ever ready for discussions. My discussions with Antina and Kaushik on various topics often lead to a better understanding. Anubhab, Harish, Mukund, Pinaki, Ratul, Raja and Rajaram were all birds of the same feathers with whom I shared a common passion for science. Ashish, Bishakh and Priyanka were extremely helpful to me in various matters. I found a junior in them to whom I could pass on my knowledge about granular materials and MD-simulations. I would like to thank Ashish and Bishakh for their company and creating a enjoyable atmosphere in the lab. I would surely miss all our late-night movie sessions. I greatly appreciate the company of Debranjan, Gayathri and Vivek.

I would like to thank the Dr. Umesh Waghmare, whose was in-charge of the complab, and other staff members for allowing me to use the LUX machine and for other computer related help.

Finally, I want to thank my parents and brother to whom I owe everything. They gave me the independence to take few very risky decisions and supported me without any hesitation even in the toughest situations.

References

[1] M. Alam and S. Luding. First normal stress difference and crystallization in a dense sheared granular fluid. *Phys. Fluids*, 15(8):2298–2312, 2003.

[2] M. Alam and S. Luding. Rheology of bidisperse granular mixtures via event driven simulations. *J. Fluid Mech.*, 476:69–103, 2003.

[3] M. Alam and S. Luding. Energy nonequipartition, rheology, and microstructure in sheared bidisperse granular mixtures. *Physics of Fluids*, 17:063303, 2005.

[4] M. Alam and S. Luding. Non-newtonian granular fluid: Simulation and theory. In *Powders and Grains 2005 (Eds. R. Gracia Rojo, H. Herrmann and S. McNamara)*, pages 1141–1145. Balkema, 2005.

[5] M. P. Allen and D. J. Tildesley. *Computer Simulation of Liquids*. Oxford University Press, Oxford, 1987.

[6] R. A. Bagnold. Experiments on a gravity-free dispersion of large solid spheres in a Newtonian fluid under shear. *Proc. Royal Soc. London*, 225:49–63, 1954.

[7] A. Barrat and E. Trizac. Lack of energy equipartition in homogeneous heated binary granular mixtures. *Granular Matter*, 4(2):57–63, 2002.

[8] J. Baudry, E. Charlaix, A. Tonck, and D. Mazuyer. Experimental evidence for a large slip effect at a nonwetting fluid-solid interface. *Langmuir*, 17:5232–5236, 2001.

[9] G. W. Baxter and J. S. Olafsen. Kinetics - gaussian statistics in granular gases. *Nature*, 425(6959):680, 2003.

[10] C. Bizon, M. D. Shattuck, J. B. Swift, and H. L. Swinney. Velocity correlations in driven two-dimensional granular media. In J. Karkheck, editor, *Dynamics: Models and Kinetic Methods for Nonequilibrium Many-Body Systems*, pages 361–371, Dordrecht, 2000. Kluwer Academic Publishers.

[11] D. L. Blair and A. Kudrolli. Velocity correlations in dense granular gases. *Phys. Rev. E*, 64(5):050301, 2001.

[12] E. Bonaccurso, M. Kappl, and H. S. Butt. Hydrodynamics force measruements : Boundary slip of water on hydrophilic surfaces and electrokinetic effects. *Phys. Rev. Lett.*, 88:076103, 2002.

[13] J. J. Brey, J. W. Dufty, C. S. Kim, and A. Santos. Hydrodynamics for granular flow at low density. *Phys. Rev. E*, 58(4):4638, 1998.

[14] N. Brilliantov and T. Pöschel. Hydrodynamics and transport coefficients for dilute granular gases. *Physical Review E*, 67:061304, 2003.

[15] F. Brochard and P. G. de Gennes. Shear-dependent slippage at a polymer/solid interface. *Langmuir*, 8:3033–3037, 1992.

[16] R. Cafiero, S. Luding, and H. J. Herrmann. Two-dimensional granular gas of inelastic spheres with multiplicative driving. *Phys. Rev. Lett.*, 84:6014–6017, 2000.

[17] C. S. Campbell. The stress tensor for simple shear flows of a granular material. *J. Fluid Mech.*, 203:449–473, 1989.

[18] C. S. Campbell. Rapid granular flows. *Ann. Rev. Fluid Mech.*, 22:57, 1990.

[19] C. S. Campbell and C. E. Brennen. Computer simulation of granular shear flows. *J. Fluid. Mech.*, 151:167, 1985.

[20] W. F. Carnahan and K. E. Starling. Equation of state for nonattracting rigid spheres. *J. Chem. Phys.*, 51(2):635–636, 1969.

[21] C. Cercignani. Higher order slip according to the linearised boltzmann equation. *Institute of Engineering Research Report, University of California Berkley*, 1964.

[22] S. Chapman and T. G. Cowling. *The Mathematical Theory of Nonuniform Gases*. Cambridge University Press, London, 1970.

[23] J.C. Chen. Clusters. In D. King, editor, *Progress in fluidized and fluid particle systems*. American Institute of Chemical Engineers, New York, 1996.

[24] P. G. de Gennes. Viscometric flows of tangled polymers. *C. R. Acad. Sci. Paris B*, 288:219–220, 1979.

[25] M. M. Denn. Extrusion instabilities and wall slip. *Ann. Rev. Fluid Mech.*, 33:267–287, 2001.

[26] J. Eggers. Sand as Maxwell's demon. *Phys. Rev. Lett.*, 83:5322–5325, 1999.

[27] Mohamed Gad el Hak. *Flow Control : Passive, Active and Reactive Flow Management*. Cambridge University Press, Oxford, 2000.

[28] S. E. Esipov and T. Pöschel. The granular phase diagram. *J. Stat. Phys.*, 86:1385–1395, 1997.

[29] K. Feitosa and N. Menon. Breakdown of energy equipartition in a 2d binary vibrated granular gas. *Phys. Rev. Lett.*, 88(19):198301–1, 2002.

[30] I. Goldhirsch. Rapid granular flows. *Annu. Rev. Fluid Mech.*, 35:267–293, 2003.

[31] I. Goldhirsch and N. Sela. Origin of normal stress differences in rapid granular flows. *Phys. Rev. E*, 54(4):4458, 1996.

[32] I. Goldhirsch and M.-L. Tan. The single-particle distribution function for rapid granular shear flows of smooth inelastic disks. *Phys. Fluids*, 8(7):1752–1763, 1996.

[33] I. Goldhirsch and G. Zanetti. Clustering instability in dissipative gases. *Phys. Rev. Lett.*, 70(11):1619–1622, 1993.

[34] H. Grad. On the kinetic theory of rarefied gases. *Comm. Pure and Appl. Math.*, 2:331, 1949.

[35] N. G. Hadjiconstantinou. Comment on cercignani's second-order slip coefficient. *Phys. Fluids*, 15(8):2352, 2003.

[36] P. K. Haff. Grain flow as a fluid-mechanical phenomenon. *J. Fluid Mech.*, 134:401–430, 1983.

[37] O. Herbst, P. Müller, and A. Zippelius. Local heat flux and energy loss in a 2d vibrated granular gas. *Phys. Rev. E*, 72:041303, 2005.

[38] M. A. Hopkins and M. Y. Louge. Inelastic microstructure in rapid granulars flow of smooth disks. *Phys. Fluids A*, 3(1):47, 1991.

[39] H. M. Jaeger, S. R. Nagel, and R. P. Behringer. Granular solids, liquids, and gases. *Rev. Mod. Phys.*, 68(4):1259–1273, 1996.

[40] J. T. Jenkins. Boundary conditions for rapid granular flow: Flat, frictional walls. *Transactions of the ASME*, 59:120–127, 1992.

[41] J. T. Jenkins and M. W. Richman. Kinetic theory for plane shear flows of a dense gas of identical, rough, inelastic, circular disks. *Phys. of Fluids*, 28:3485–3494, 1985.

[42] J. T. Jenkins and R. W. Richman. Plane simple shear of smooth inelastic circular disks: the anisotropy of the second momnent in the dilute and dense limit. *J. Fluid Mech.*, 192:313, 1988.

[43] J. T. Jenkins and S. B. Savage. A theory for the rapid flow of identical, smooth, nearly elastic, spherical particles. *J. Fluid Mech.*, 130:187–202, 1983.

[44] P. C. Johnson and R. Jackson. Frictional-collisional constitutive relations for granular materials, with application to plane shearing. *J. Fluid. Mech.*, 176:67, 1987.

[45] L. P. Kadanoff. Built upon sand: Theoretical ideas inspired by granular flows. *Rev. Mod. Phys.*, 71(1):435–444, 1999.

[46] G. Karniadakis and A. Beskok. *Micro Flows : Fundamentals and Simulation.* Springer, Springer, 2001.

[47] E. Kennard. *kinetic Theory of Gases.* McGraw-Hill Book Co. Inc., New York, 1938.

[48] E. D. Liss, S. L. Conway, and B. J. Glasser. Density waves in gravity-driven granular flow through a channel. *Phys. Fluids*, 14(9):3309–3326, 2002.

[49] A. J. Liu and S. R. Nagel. Jamming and rheology: An introduction. In A. J. Liu and S. R. Nagel, editors, *Jamming and Rheology: Constrained Dynamics on Microscopic and Macroscopic Scales.* Taylor and Francis, 2001.

[50] W. Losert, D. G. W. Cooper, J. Delour, A. Kudrolli, and J. P. Gollub. Velocity statistics in vibrated granular media. *Chaos*, 9(3):682–690, 1999.

[51] B. D. Lubachevsky. How to simulate billards and similar systems. *J. Comp. Phys.*, 94(2):255, 1991.

[52] S. Luding. Global equation of state of two-dimensional hard sphere systems. *Phys. Rev. E*, 63:042201–1–4, 2001.

[53] S. Luding and H. J. Herrmann. Cluster growth in freely cooling granular media. *Chaos*, 9(3):673–681, 1999.

[54] S. Luding and S. McNamara. How to handle the inelastic collapse of a dissipative hard-sphere gas with the TC model. *Granular Matter*, 1(3):113–128, 1998.

[55] C. K. K. Lun, S. B. Savage, D. J. Jeffrey, and N. Chepurniy. Kinetic theories for granular flow: inelastic particles in couette flow and slightly inelastic particles in a general flowfield. *J. Fluid. Mech.*, 140:223–256, 1984.

[56] S. McNamara and W. R. Young. Inelastic collapse and clumping in a one-dimensional granular medium. *Phys. Fluids A*, 4(3):496–594, 1992.

[57] S. McNamara and W. R. Young. Inelastic collapse in two dimensions. *Phys. Rev. E*, 50(1):R28–R31, 1994.

[58] M. E. Möbius, B. E. Lauderdale, S. R. Nagel, and H. M. Jaeger. Brazil-nut effect: Size separation of granular particles. *Nature*, 414(270):15, 2001.

[59] G. Metcalfe, T. Shinbrot, J. J. McCarthy, and J. M. Ottino. Avalanche mixing of granular solids. *Nature*, 374:39–42, 1995.

[60] R. Mikkelsen, D. van der Meer, K. van der Weele, and D. Lohse. Competitive clustering in a bidisperse granular gas. *Phys. Rev. Lett*, 89:214301, 2002.

[61] R. Mikkelsen, K. van der Weele, D. van der Meer, M. Versluis, and D. Lohse. Competitive clustering in a granular gas. *Phys. Fluids*, 15(9), 2003.

[62] S. Miller and S. Luding. Event driven simulations in parallel. *J. Comp. Phys.*, 193(1):306–316, 2004.

[63] S. Moka and P. R. Nott. Statistics of particle velocities in dense granular flows. *Phys. Rev. Lett.*, 95:068003, 2005.

[64] S. J. Moon, M. D. Shattuck, and J. B. Swift. Velocity distributions and correlations in homogeneously heated granular media. *Phys. Rev. E*, 64:031303, 2001.

[65] E. P. Muntz. Rarefied-gas dynamics. *Ann. Rev. Fluid. Mech.*, 21:387–417, 1989.

[66] Y. Murayama and M. Sano. Transition from gaussian to non-gaussian velocity distribution functions in a vibrated granular bed. *J. Phys. Soc. Japan*, 67:1826–1829, 1998.

[67] S. R. Nagel. Instabilities in a sandpile. *Rev. of Mod. Phys.*, 64(1):321, 1992.

[68] V. V. R. Natarajan, M. L. Hunt, and E. D. Taylor. Local measurements of velocity fluctuations and diffusion coefficients for a granular material flow. *J. Fluid Mech.*, 304:1, 1995.

[69] S. Ogawa. Multitemperature theory of granular materials. In S. C. Cowin and M. Satake, editors, *Proc. of US-Japan Symp. on Continuum Mechanics and Statistical Approaches to the Mechanics of Granular Media*, page 208, Fukyu-kai, 1978. Gakujutsu Bunken.

[70] T. Ohwada, Y. Sone, and K. Aoki. Numerical analysis of the shear and thermal creep flows of a rarefied gas over a plane wall on the basis of the linearised boltzmann equation for hard-sphere molecules. *Phys. Fluids A*, 1:1588, 1989.

[71] J. M. Ottino and D. V. Khakhar. Mixing and segregation of granular materials. *Ann. Rev. Fluid Mech.*, 32:55, 2000.

[72] G. Peng and H. J. Herrmann. Density waves of granular flow in a pipe using lattice-gas automata. *Phys. Rev. E*, 49(3):1796, 1994.

[73] Olivier Pouliquen. Velocity correlations in dense granular flows. *Physical Review Letters*, 93:248001, 2004.

[74] A. Prevost, D. A. Egolf, and J. S. Urbach. Forcing and velocity correlations in a vibrated granular monolayer. *Phys. Rev. Lett.*, 89:084301, 2002.

[75] A. Puglisi, V. Loreto, U. M. B. Marconi, and A. Vulpiani. Clustering and non-gaussian behavior in granular matter. *Phys. Rev. Lett.*, 81:3848, 1998.

[76] T. Raafat, J. P. Hulin, and H. J. Herrmann. Density waves in dry granular media falling through a vertical pipe. *Phys. Rev. E*, 53:4345–4355, 1996.

[77] D. C. Rapaport. *The Art of Molecular Dynamics Simulation.* Cambridge University Press, Cambridge, 1995.

[78] M. W. Richman. Boundary conditions based upon a modified maxwellian velocity distribution for flows of identical, smooth, nearly elastic spheres. *Acta. Mech.*, 75:227, 1988.

[79] M. W. Richman. The source of second moment in dilute granular flows of highly inelastic spheres. *J. Rheol.*, 33(8):1293, 1989.

[80] T. Riethmueller, L. Schimansky-Geier, Dirk Rosenkranz, and T. Pöschel. Langevin equation approach to granular flows in narrow pipes. *J. Stat. Phys.*, 86:421, 1997.

[81] F. Rouyer and N. Menon. Velocity fluctuations in a homogeneous 2d granular gas in steady state. *Phys. Rev. Lett.*, 85(17):3676, 2000.

[82] S. B. Savage. Granular flows down rough inclines - review and extension. In J. T. Jenkins and M. Satake, editors, *Proc. US-Japan Seminar on New Models and Constitutive Relations in Mechanics of Granular Materials.* Elsevier, 1982.

[83] S. B. Savage and D. J. Jeffrey. The stress tensor in a granular flow at high shear rates. *J. Fluid. Mech.*, 110:255, 1981.

[84] H. J. Schlichtting and V. Nordmeier. Strukturen im sand. kollektives verhalten und selbstorganisation bei granulaten. *MNU*, 49(6):323–332, 1996.

[85] N. Sela and I. Goldhirsch. Hydrodynamic equations for rapid flows of smooth inelastic spheres to Burnett order. *J. Fluid Mech.*, 361:41–74, 1998.

[86] T. Shinbrot and F. J. Muzzio. Noise to order. *Nature*, 410:251–258, 2001.

[87] R. Soto, M. Mareschal, and D. Risso. Departure from Fourier's law for fluidized granular media. *Phys. Rev Lett.*, 83(24):5003–5006, 1999.

[88] Y.-h. Taguchi and H. Takayasu. Power law velocity fluctuations due to inelastic collisions in numerically simulated vibrated bed of powder. *Europhys. Lett.*, 30(8):499–504, 1995.

[89] M. L. Tan and I. Goldhirsch. Intercluster interactions in rapid granular shear flows. *Phys. Fluids*, 9(4):856, 1997.

[90] K. To, P.-Y. Lai, and H. K. Pak. Jamming of granular flow in two-dimensional hopper. *Phys. Rev. Lett.*, 86(1):71, 2001.

[91] A. Valence and T. Le Pennec. Non-linear dynamics of density waves in granular flows through narrow vertical channels. *Eur. Phys. J. B*, 5:223, 1998.

[92] D. van der Meer, K. van der Weele, and D. Lohse. Sudden collapse of a granular cluster. *Phys. Rev. Lett.*, 88:174302, 2002.

[93] T. P. C. van Noije and M. H. Ernst. Velocity distributions in homogeneous granular fluids: the free and the heated case. *Granular Matter*, 1(2):57–64, 1998.

[94] J. S. van Zon and F. C. MacKintosh. Velocity distributions in dissipative granular gases. *Phys. Rev. Lett.*, 93(3):038001–1–4, 2004.

[95] L. Verlet and D. Levesque. Integral equations for classical fluids. III. the hard disks system. *Mol. Phys.*, 46(5):969–980, 1982.

[96] K. C. Vijayakumar and M. Alam. Velocity distribution and the effect of wall roughness in granular poiseuille flow. *Phys. Rev. E*, 75:051306, 2007.

[97] O. R. Walton and R. L. Braun. Viscosity, granular-temperature, and stress calculations for shearing assemblies of inelastic, frictional disks. *J. Rheol.*, 30(5):949–980, 1986.

[98] C.-H. Wang, R. Jackson, and S. Sundaresan. Instabilities of fully developed rapid flow of a granular material in a channel. *J. Fluid Mech.*, 342:179, 1997.

[99] T. Zhou and L. P. Kadanoff. Inelastic collapse of three particles. *Phys. Rev. E*, 54:623, 1996.

[100] Iker Zuriguel, Angel Garcimart´in, Diego Maza, Luis A. Pugnaloni, and J. M. Pastor. Jamming during the discharge of granular matter from a silo. *Physical Review E*, 71:051303, 2005.